Modeling electro-magnetic and thermal Stability of Cable-in-Conduit Superconductors for Fusion Magnets

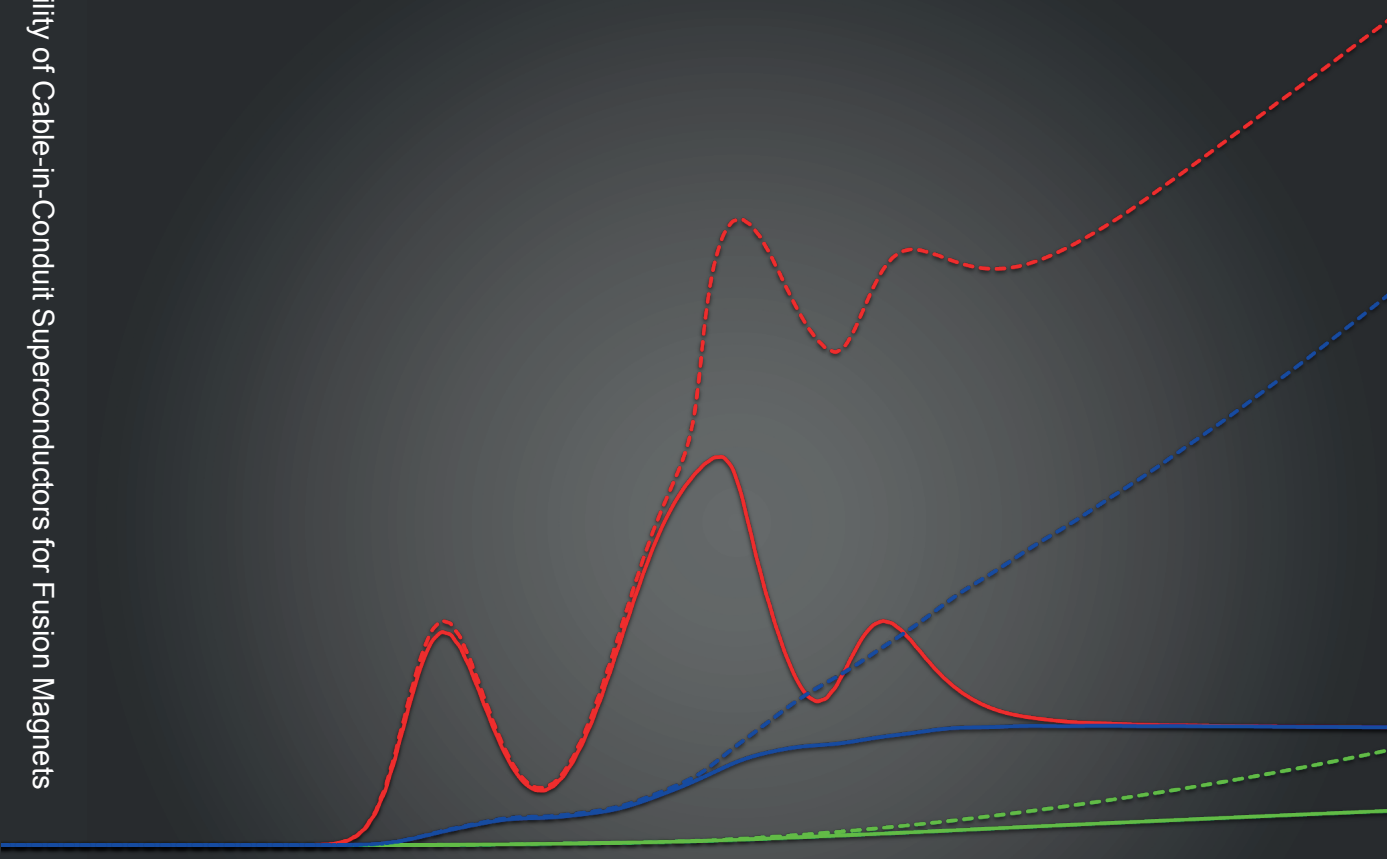

Tommaso Bagni

UNIVERSITY OF TWENTE.

GHENT UNIVERSITY

Modeling electro-magnetic and thermal Stability of Cable-in-Conduit Superconductors for Fusion Magnets

T. Bagni

2018

MODELING ELECTRO-MAGNETIC AND THERMAL STABILITY OF CABLE-IN-CONDUIT SUPERCONDUCTORS FOR FUSION MAGNETS

Tommaso Bagni

MODELING ELECTRO-MAGNETIC AND THERMAL STABILITY OF CABLE-IN-CONDUIT SUPERCONDUCTORS FOR FUSION MAGNETS

DISSERTATION

to obtain
the degree of doctor at the University of Twente
on the authority of the rector magnificus
prof. dr. T.T.M. Palstra
on account of the decision of the Doctorate Board,
to be publicly defended
on Wednesday the 12th of December 2018 at 12.45 hours

by
Tommaso Bagni

born on the 3rd of November 1985
in Torino, Italy

This thesis was approved by the supervisors:

Prof. dr. ir. H.H.J. ten Kate (University of Twente)

Prof. dr. dr.h.c. ir. J.M. Noterdaeme (Ghent University)

This thesis was prepared for a Joint Doctorate at the University of Twente and Ghent University.

Modeling electro-magnetic and thermal Stability of Cable-in-Conduit Superconductors for Fusion Magnets
T. Bagni
Ph.D. thesis, University of Twente, The Netherlands and Ghent University, Belgium
ISBN: 978-90-365-4674-4
Printed by Ipskamp Printing, Enschede, The Netherlands
Cover by T. Bagni
© T. Bagni, Enschede, The Netherlands – 2018.

All rights reserved. No parts of this thesis may be reproduced, stored in a retrieval system or transmitted in any form or by any means without permission of the author.

JackPot-ACDC © Arend Nijhuis, University of Twente, Enschede. All rights reserved.

PhD Graduation Committee:

Chairman	: Prof. dr. ir. J.W.M. Hilgenkamp	University of Twente
Supervisor 1	: Prof. dr. ir. H.H.J. ten Kate	University of Twente
Supervisor 2	: Prof. dr. dr.h.c. ir. J.M. Noterdaeme	Ghent University
Co-supervisor	: Dr. ing. A. Nijhuis	University of Twente
Members	: Prof. dr. ir W. Biel	Ghent University
	Prof. dr. ir. F. De Turck	Ghent University
	Dr. A. Devred	CERN, Switzerland
	Prof. dr. J.L. Herek	University of Twente
	Dr.-Ing. A. Kario	GSI, Germany
	Prof. dr. ir. H.J.M ter Brake	University of Twente

The research described in this thesis was carried out at the University of Twente, Enschede, The Netherlands in cooperation with the ITER Organization, Cadarache, France and Ghent University, Ghent, Belgium. It was financially supported by the ITER Organization, Cadarache, France as well as the Fusion Doctorate College, Ghent, Belgium.

UNIVERSITY OF TWENTE.

GHENT UNIVERSITY

Disclaimer: The views and the opinions expressed herein do not necessarily reflect those of the ITER Organization as well as EUROFusion.

per mio padre

to my father

SUMMARY

ITER is going to be the first experimental pulsed fusion reactor designed to produce a net output power and it will be the largest fusion facility in the world. The tokamak magnet system is based on NbTi and Nb_3Sn Cable-In-Conduit superconductors. All ITER conductors have to follow a strict qualification program, which includes test of current sharing temperature, coupling loss and electromagnetic and thermal stability. Most of the tests are performed at the SULTAN facility of the Swiss Plasma Center complementary test are performed at the University of Twente. Due to the high cost of tests, limited length of the conductor samples and, for Nb_3Sn Cable-In-Conduit Conductors, magnetic field and magnetic field rates lower than the peak values during ITER operating conditions, dedicated simulations are necessary to extend the comprehension of CIC Conductor behavior. The aim of this thesis is to investigate and predict the stability operational behavior for the ITER plasma-operating scenario.

Different models are applied for the analysis of the NbTi and Nb_3Sn CIC Conductors. The analytical Model with PArtial Shielding zone (MPAS), developed at the CEA, France, is used to fit and express the CIC Conductors coupling loss. The numerical model JackPot ACDC, developed at the University of Twente, is used to analyze electromagnetic behavior of the conductors at strand, cable and coil levels. Both models are used in combination with the THEA software (Thermal, Hydraulic and Electric Analysis of Superconducting Cables) to model the thermal and hydraulic behavior of the conductors and their coolant.

The MPAS-THEA models combination prove to be effective for analyzing the stability tests performed on ITER Poloidal Field coil conductors. The studied sample is designed for the ITER Poloidal Field coils 1 and 6. The SULTAN measurement results are used to calibrate and validate the codes. MPAS-THEA can simulate the thermal behavior of the conductor sample during Minimum Energy Quench (MQE) tests. The conductor MQE tests are performed using a single sine wave magnetic field pulse. The fast magnetic field variations generate current loops and heat dissipation, which cause a quench when exceeding a certain critical level of energy. After the validation of the model the results are compared to the JackPot simulation results of the same sample conductor.

The analysis of the Nb_3Sn CIC Conductors is more critical; these conductor are exposed to extreme current and magnetic field levels during the Plasma Operating scenario representative for the worst operating conditions. In

particular, the Central Solenoid is exposed to fast changes of current and magnetic field, reaching over 13 T with a maximum rate of 1.5 T/s after the Start of the Discharge. In the experimental data available, the conductor layout, the time and the magnetic field settings are significantly different from the real ITER operating conditions and also the MQE tests conditions do not cover satisfactorily the Plasma Operating conditions. Nevertheless, in a best-effort approach, the test results are applied to calibrate the simulation codes.

One of the Japanese Central Solenoid conductor samples, so-called CSJA8 and tested in SULTAN is used to calibrate the models. The MPAS-THEA combination showed the limitations of the analytical model for Nb_3Sn conductors, failing to reproduce the experimental stability tests. On the other hand, JackPot-ACDC is able to study the behavior of the sample and to achieve accurate transient stability predictions. JackPot is suitable for the calculation of local ohmic loss since it is able to generate the full geometry of a real CIC Conductor at strand level and to simulate the electromagnetic behavior of a conductor undergoing varies stability tests and a Plasma Scenario. THEA is combined with JackPot to model the normal zone and its propagation along the conductor. The resulting combination of codes, in this study called JackPot-THEA, is able to predict the stability limit of a conductor, starting only from testing conditions of current, temperature and magnetic field. The model is validated with the results based on SULTAN short sample stability tests with very short pulse duration. The current distribution calculated at strand level, and the corresponding power dissipation generated during the stability tests, allow the evaluation of the local peak and average electric fields and the definition of an electric field threshold as a criteriafor the ITER Nb_3Sn CIC Conductor stability.

The definition of an electric field threshold, supported by the JackPot-THEA model, facilitates to compare quantitatively short sample stability tests and conductor performance under actual ITER plasma operating conditions.

During the ITER plasma scenario the most severe condition is during the Start of the Discharge, which is not directly comparable to the SULTAN stability results. The stability results obtained from the analysis of the SULTAN tests are used to extrapolate and investigate using JackPot-THEA the MQE for more relevant magnetic field disturbances. Subsequently, the performance of the ITER Central Solenoid is analyzed with the JackPot-THEA model, in order to predict the stability of the Central Solenoid conductor under realistic load conditions. The temperature evolution in the CIC Conductor during the plasma scenario is

analyzed and used to investigate the temperature evolution of one full layer of the Central Solenoid module exposed to the most severe magnetic field conditions. The peak and average electric fields generated during the 15 MA Plasma Scenario are compared to the electric field threshold of the short sample stability simulations in order to analyze the stability of the entire coil. Considering the defined electric field criteria, the ITER Central Solenoid conductor does not show stability issues. On the contrary, the JackPot-THEA confirms the ability of the Central Solenoid for continuous operation of the 15 MA Plasma Scenario burn cycles.

While ITER is under construction, the research and development for the next step demonstration reactor, called DEMO (DEMOnstration Power Station) in Europe, is underway. Two different cable designs for DEMO's Toroidal Field coil were developed by the Swiss Plasma Centre and the Italian National Agency for New Technologies, (ENEA), respectively. DEMO conductors differ from the ITER ones in shape, diameter of strands, cable pattern and twist pitch. The two sample conductors were tested in the EDIPO facility at Swiss Plasma Center and in the Cryogenic Cable Press facility at the University of Twente. The test results are used to calibrate and validate the JackPot model for the new geometries. After the validation, a first stability analysis is performed to compare the peak electric field reached during the fast transient to the ITER CS conductor electric field.

The work presented in the thesis demonstrates the advancing tools and next steps in Stability Simulations of Cable in Conduit Conductors. The electromagnetic analysis at strand level, combined with the thermal behavior of the conductor, provides a new and very powerful method for designing conductors for next generation magnets for fusion.

SAMENVATTING (Summary in Dutch)

ITER, de International Tokamak Engineering Reactor, op dit moment in aanbouw in Cadarache, Zuid Frankrijk, wordt de eerste experimentele gepulste tokamak fusiereactor met een positief rendement en is daarmee de grootste fusiereactor in de wereld. Het zogenaamde tokamak magneetsysteem is gebaseerd op het gebruik van NbTi- en Nb_3Sn supergeleiders, uitgevoerd als een kabel met vele draden in een stalen behuizing, de zogenoemde Cable-In-Conduit (CIC) geleiders. Alle geleiders voor ITER moeten een streng kwalificatie-onderzoek ondergaan, waarbij onder meer de magnetische en thermische stabiliteit, het koppelingsverlies en de zogenaamde stroom ver de lings temperatuur (current sharing) worden gemeten. De meeste van deze kwalificatietesten worden uitgevoerd in de SULTAN-faciliteit bij het Swiss Plasma Center, met aanvullende tests bij de Universiteit Twente. Vanwege de hoge kosten van deze kwalificatietests, de beperkte lengte van de te testen geleiders, en de voor Nb_3Sn CIC-geleiders benodigde extreme magneetvelden en magneetveldveranderingen voor het representatief testen onder de piekbelastingen van ITER, is besloten dat numerieke simulaties noodzakelijk zijn om het gedrag van de CIC-geleiders verder in kaart te brengen. Het doel van dit proefschrift is om de stabiliteit van de stroomgeleiders in ITER-magneten tijdens de extreme operationele omstandigheden te onderzoeken en te kunnen voorspellen.

Een aantal verschillende modellen worden gebruikt voor de analyse van de NbTi en Nb_3Sn CIC-geleiders. Het analytische MPAS (Model met Gedeeltelijk Afgeschermd Gebied), ontwikkeld bij CEA in Frankrijk, wordt gebruikt om de koppelingsverliezen in de CIC-geleider te beschrijven. Het numerieke model JackPot AC/DC ontwikkeld aan de Universiteit Twente, wordt gebruikt om het elektromagnetisch gedrag op draad-, kabel- en spoelniveau te modelleren. Beide modellen worden gebruikt in combinatie met THEA (Thermische, Hydraulische en Elektrische Analyse van Supergeleidende kabels), het softwarepakket om de thermische en hydraulische gedragingen van de geleider en het koelmedium te voorspellen.

De combinatie MPAS-THEA is effectief gebleken voor het analyseren van de stabiliteitsproeven van de poloïdale veldspoelen van ITER. De geteste geleider was ontworpen voor de spoelen 1 en 6. De resultaten van stabiliteitsmetingen in SULTAN worden gebruikt om de numerieke code voor het model te kalibreren en te valideren. MPAS-THEA kan het thermische gedrag van de geleider gedurende minimum quench energie (MQE) experimenten modelleren. De MQE

experimenten zijn uitgevoerd met een enkele sinusoïdale magneetveldpuls. De variaties in het magneetveld genereren kleine stroomkringen en warmte die een quench kunnen veroorzaken wanneer een bepaalde kritieke hoeveelheid energie wordt overschreden. Na validatie van het model zijn de resultaten vergeleken met de JackPot simulaties van dezelfde geleider.

De analyse van de Nb_3Sn CIC-geleiders is van groot belang. Deze geleiders worden blootgesteld aan extreem hoge stromen en magneetveld veranderingen gedurende plasma controle fase in ITER. Dit is het zwaarste belastingscenario voor deze geleiders. De Centrale Solenoïde moet bij een magneetveld van 13 T extreme magneetveldveranderingen van maximaal 1.5 T/s gedurende de ontladingsfase kunnen weerstaan. De beschikbare testresultaten betreffen een geleiderontwerp, meettijd en magneetveld instellingen die significant afwijken van de daadwerkelijke omstandigheden in ITER. Dit is ook het geval voor de MQE experimenten die niet alle omstandigheden gedurende de plasma controle fase afdekken. Desalniettemin worden de beschikbare testresultaten zo goed als mogelijk gebruikt om de simulatiecode te kalibreren.

Een van de Japanse geleiders voor de ITER centrale solenoïde, CSJA8, is getest in de SULTAN-faciliteit voor het kalibreren van de modellen. De MPAS-THEA combinatie liet de beperkingen van het analytische model voor de Nb_3Sn geleiders zien en kon de stabiliteitstests niet goed reproduceren. JackPot AC/DC echter, is tegelijkertijd in staat om het gedrag van de geleider te laten zien en om nauwkeurige voorspellingen te doen. JackPot is geschikt voor de berekening van het lokale ohmse verlies omdat het in staat is om de gehele geometrie van de CIC-geleider op draadniveau te genereren. Daarnaast is het mogelijk om het elektromagnetische gedrag van een geleider te voorspellen voor verschillende stabiliteitstests en voor elk mogelijke plasmascenario. De code THEA wordt gecombineerd met JackPot om het normaal-geleidende gebied en de propagatie van dit gebied in de geleider te modelleren. De resulterende combinatie van modellen, in deze thesis JackPot-THEA genoemd, is in staat om de stabiliteitslimieten van een CIC-geleider te voorspellen, enkel en alleen op basis van de initiële stroom, temperatuur en magneetveldomstandigheden. Dit model is gevalideerd met behulp van de resultaten gemeten in de SULTAN-experimenten aan korte geleiders en met korte pulsen. De stroomverdeling, berekend op draadniveau gedurende de stabiliteitstests en de bijbehorende warmteontwikkeling, maken het mogelijk om de lokale piek-en gemiddelde elektrische velden te bepalen, hetgeen een criterium geeft voor de stabiliteit van de ITER Nb_3Sn CIC-geleider.

De definitie van een criterium voor het elektrisch veld, met ondersteuning van het JackPot-THEA model, stelt ons in staat om kwantitatief resultaten van stabiliteitstests te vergelijken van korte stukken geleider en dan te extrapoleren naar de extreme ITER plasma condities.

De zwaarste belasting in het plasmascenario van ITER vindt plaats tijdens de start van de ontlading. Dit deel is niet direct vergelijkbaar met de SULTAN stabiliteitsresultaten. De resultaten, verkregen door analyse van de SULTAN experimenten, worden geëxtrapoleerd en onderzocht met behulp van het JackPot-THEA model voor het berekenen van de MQE voor meer relevante magneetveld veranderingen. Tevens wordt het gedrag van de centrale ITER-solenoïde geanalyseerd met behulp van het JackPot-THEA model om de stabiliteit van de centrale solenoïde geleider in een realistisch plasmascenario te onderzoeken. Het temperatuurverloop in de CIC-geleider gedurende het plasmascenario wordt berekend om het temperatuurverloop in de gehele binnenste laag wikkelingen van de centrale solenoïde te bestuderen die aan de zwaarste belasting onderhevig zijn. De piek-en gemiddelde waardes van het elektrisch veld dat gegenereerd wordt tijdens het 15 MA-plasmascenario, worden vergeleken met de simulatieresultaten van de stabiliteit van de korte geleiders om de stabiliteit van de gehele solenoïde te voorspellen. Wanneer het elektrisch veld criterium in acht wordt genomen, dan laat de ITER centrale solenoïde geen tekenen van stabiliteitsproblemen zien. Tevens bevestigt het JackPot-THEA model de geschiktheid van de centrale solenoïde voor een continue belasting met het 15 MA plasmascenario.

Terwijl ITER wordt gebouwd concentreert het onderzoek zich op de volgende fusiereactor DEMO (DEMOnstratie elektriciteitscentrale) in Europa. Twee verschillende ontwerpen voor de geleider van de toroïdale veldspoel van DEMO zijn ontwikkeld door het Swiss Plasma Center (SPC) en het Italiaanse ENEA. De verschillen tussen de geleiders van DEMO en ITER zitten in de vorm van de geleiderdoorsnede, afmetingen van de kabel en het kabelpatroon. Twee demonstratie geleiders zijn getest in de EDIPO-faciliteit bij het SPC en de cryogene kabelpers bij de Universiteit Twente. Opnieuw worden de testresultaten gebruikt om de JackPot code te valideren voor de nieuwe geleiderstructuur. Na validatie is een stabiliteitsanalyse gedaan om het maximale elektrische veld te vergelijken met het elektrische veld in de ITER Centrale Solenoïde geleider.

Het werk, gepresenteerd in dit proefschrift, laat de verdere ontwikkeling en volgende stappen zien in simulaties van stabiliteit in zogenaamde Cable in Conduit geleiders. De elektromagnetische analyse op draadniveau, gecombineerd met het thermische gedrag van de geleider, biedt een nieuwe en zeer sterke basis voor het ontwikkelen van geleiders voor de volgende generatie magneten voor kernfusie.

TABLE OF CONTENTS

Summary ***ix***

Samenvatting (Summary in Dutch) ***xiii***

1. Introduction ***1***

1.1. Nuclear Fusion **1**

1.2. ITER magnet system **4**

1.3. DEMO reactor **9**

1.4. Technical superconductors **10**

1.4.1. Strands and CICCs 15

1.4.2. AC loss 18

1.4.3. Stability 24

1.5. Scope of the thesis **25**

2. Experiments and Modeling ***27***

2.1. Introduction **27**

2.2. SULTAN facility **27**

2.2.1. SULTAN Setup 28

2.2.2. SULTAN test procedure 29

2.2.3. Sultan AC magnetic field amplitude during MQE tests 31

2.3. JackPot AC/DC **33**

2.3.1. Introduction 33

2.3.2. Cable model 34

2.3.3. Inter-strand contact resistances 36

2.3.4. Self- and mutual inductances 37

2.3.5. Magnetic field coupling 38

2.3.6. System of Equations 39

2.4. Model with Partial Shielding zone (MPAS) **40**

2.4.1. Coupling loss calculation 41

2.4.2. Stability calculation 42

2.5. THEA **43**

2.5.1. Cable model and SULTAN sample 43

2.6. Structure of the modeling **44**

3. Modeling stability of Poloidal Field Coil conductor ____ *47*

3.1. Introduction ____ **47**

3.2. PFEU2: conductor layout and parameters ____ **47**

3.3. Stability tests ____ **49**

3.4. Simulation using MPAS-THEA code ____ **52**

3.4.1. MPAS calibration ____ 52

3.4.2. MPAS-THEA stability simulations ____ 53

3.4.3. Effect of the jacket on calorimetric measurements ____ 59

3.4.4. Effect of the central channel on short pulse MQE ____ 60

3.5. Simulation using JackPot AC/DC ____ **62**

3.5.1. JackPot calibration ____ 62

3.5.2. JackPot simulations ____ 63

3.6. Conclusion ____ **65**

4. Modeling transient stability of the Central Solenoid conductor _ *67*

4.1. Introduction ____ **67**

4.2. Minimum Quench Energy of the CSJA8 conductor ____ **68**

4.3. MPAS-THEA ____ **72**

4.3.1. MPAS calibration ____ 72

4.3.2. MPAS-THEA stability simulation ____ 73

4.4. JackPot-THEA ____ **77**

4.4.1. JackPot calibration by AC loss ____ 77

4.4.2. JackPot-THEA simulations ____ 78

4.4.3. Stability for 1 s pulse period ____ 81

4.4.4. Stability for 5 s pulse period ____ 84

4.4.5. Discussion ____ 89

4.5. Conclusion ____ **90**

5. Stability of ITER Central Solenoid conductor during the 15MA Plasma Scenario ____ *93*

5.1. Introduction ____ **93**

5.2. ITER Central Solenoid design and plasma scenario ____ **93**

5.3. JackPot-THEA electric field threshold definition ____ **96**

5.4. JackPot Plasma Scenario short sample simulation _____ 98
5.4.1. Magneto-resistance and Lorentz' force effect _____ 99
5.4.2. Simulation results _____ 100

5.5. Temperature evolution in a layer of CSU2 module _____ 104
5.5.1. JaskPot-THEA results _____ 105

5.6. Conclusion _____ 107

6. Toroidal Field conductors for DEMO _____ 109

6.1. Introduction _____ 109

6.2. Rectangular TF WP1 Conductor _____ 109
6.2.1. AC loss analysis _____ 112
6.2.2. WP1 stability analysis _____ 116

6.3. Rectangular TF WP2 Conductor _____ 119
6.3.1. AC loss analysis _____ 122
6.3.2. WP2 stability analysis _____ 130

6.4. Strand diameter effect study _____ 133
6.4.1. Coupling loss _____ 135
6.4.2. Stability analysis _____ 136

6.5. Conclusion _____ 138

7. Conclusion _____ 141

A. Energy calculation of SULTAN stability tests _____ 147

A.1. Introduction _____ 147

A.2. Minimization of the temperature fluctuation _____ 147

A.3. Energy Calculation _____ 153

References _____ 157

Acknowledgement _____ 169

1. INTRODUCTION

1.1. Nuclear Fusion

Nuclear fusion is a reaction in which two or more atomic nuclei form one or more different atomic nuclei. During the fusion, the difference in mass between the products and reactants is released in the form of energy. Fusion is the process that powers active stars as our sun. The energy release is due to the effect of two opposite forces: the Nuclear force, responsible for combining protons and neutrons, and the Coulomb force, which causes the repulsion between particles with the same electric charge [1].

Nuclei smaller than iron are sufficiently poor of protons to allow the nuclear force to overcome the Coulomb force. These light nuclei build new nuclei by fusion, releasing the extra energy. The stars are powered by fusion reactions producing virtually all elements in a process called nucleosynthesis.

For example in the sun's core, where temperature reaches 15 million Kelvin, hydrogen atoms are in a constant state of agitation. As they collide at very high speed, the natural electrostatic repulsion that exists between the positive charges of their nuclei is overcome and the atoms fuse. The fusion of light hydrogen atoms produces the heavier element helium. A 0.7% fraction of the mass is transformed into electromagnetic radiation or into kinetic energy of an alpha particle or other forms of energy [2]. This is a direct consequence of Einstein's formula: $E = mc^2$. The small lost mass (m), multiplied by the square of the speed of light (c^2), results in a very large amount of energy (E), which is the energy created by the fusion reaction. Every second, the sun turns about 600 million tons of hydrogen into helium, thereby releasing an enormous amount of energy. Without the huge gravitational forces involved in the sun's fusion process, achieving fusion in a machine on earth needs a different approach.

Thermonuclear fusion potentially is an attractive source of energy, because the fuel is abundant and a limited amount is necessary for the reaction, 250 kg for 1 GW/year. The process is considered intrinsically safe, because any variation in the required conditions will cause a plasma disruption, leading to a cool down ending the reaction. Moreover, there is no emission of pollution or greenhouse gases from the fusion process itself. The main drawbacks are the radioactivity accumulated in the inner wall of the reactor and the radiation damage mainly due to neutron

bombardment, introduced in the plasma facing components, forcing a periodic and time-consuming replacement of these parts.

Twentieth-century fusion science identified the most efficient fusion reaction in the laboratory setting to be the reaction between two hydrogen (H) isotopes deuterium (D) and tritium (T) [3]. The DT fusion reaction produces the highest energy gain at the "lowest" temperature. It requires nonetheless temperatures of 150 MK, ten times higher than the hydrogen reaction occurring in the sun.

Since the second half of the twentieth century, research on fusion energy has largely progressed. Several fusion machines, primarily tokamaks, have been constructed, which can generate and maintain plasmas for several minutes. At present, the largest operating fusion experiment in the world is the Joint European Torus (JET) in Culham (UK) [4]. This machine also holds the record for the generation of fusion energy with 16 MW during 1 second, and a continuous fusion capacity of 4 MW during 4 seconds. The next step towards exploration and demonstration of fusion energy is represented by ITER [5], presently under construction. It is going to be the first pulsed device designed to produce a net output power. The volume of the plasma seems to be crucial for the ratio between input and output power. The cross section of ITER compared to existing tokamaks is shown in Figure 1.1.

In spite of the substantial progress, several technological challenges remain on the path eventually leading to commercial fusion power plants [6]:

- To achieve the conditions enabling a net energy production, plasmas must be maintained at high density and temperature for a few hours or even in steady-state. This requires the minimization of energy loss due to small-scale turbulences and plasma instabilities. At the same time, a large fraction of the heating power must be radiated by the confined plasma to avoid excessive heat load on localized components of the machine. Operating plasma regimes simultaneously ensuring high plasma confinement and radiation have yet to be qualified.
- The power necessary to maintain plasmas at high temperatures is ultimately exhausted in a narrow region of the reaction chamber called the divertor. Although exhaust systems able to withstand heat fluxes up to 20 MW/m^2 (which is of the same order of the heat load on the sun's surface) have been produced for ITER, solutions for the larger power load on the divertor expected in future fusion machines still needs to be developed.

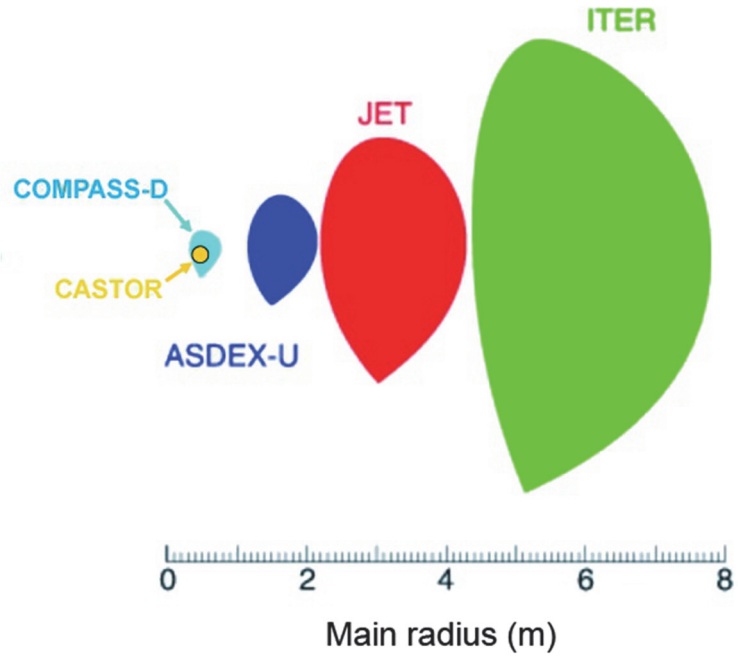

Figure 1.1 – Cross section of plasmas and radii of some European tokamak fusion reactors, showing the difference between ITER and its predecessors.

- Neutron resistant materials able to withstand 14 MeV neutron flux and to maintain their structural and thermal conduction properties for long operation times need to be developed. Although some candidates materials already exist (EUROFER for the breeding blanket, tungsten for plasma facing component armor and copper alloys for the divertor coolant interface) much more R&D is needed to find new solutions in order to significantly enhance the operational lifetime of the reactor components. In addition, the completion of their characterization under relevant conditions requires the creation of dedicated irradiation facilities.
- Tritium self-sufficiency is mandatory for future fusion power plants. It requires the research of efficient breeding and extraction systems as well as tritium loss minimization. The sufficiently effective Tritium breading yet has to be demonstrated in real fusion processes.

In order to address the above issues, the DEMO project [6] is currently envisaged as the next step after ITER towards a prototype fusion power plant. On a longer

time scale, alternative magnetic confinement fusion devices may also reach sufficient technological maturity. In this respect, the stellarator is the most promising configuration offering certain advantages over tokamaks, such as capability for steady-state operation and lower occurrence rate of plasma instabilities [6]. In addition, the stellarator has less magneto-hydrodynamic (MHD) instabilities and it is nearly disruption-free [7]. Currently, the stellarator machine W7X using a superconducting magnet system as well is in its early stage of operation [8].

To be economically successful fusion will need to demonstrate its potential for competitive cost of electricity. Extended operation times, high efficiency of the power conversion cycle and reliable operation for several decades have to be ensured for enabling commercial fusion power plants. To reduce construction costs, materials, especially for the divertor and the first wall, allowing extended operational time and simple fabrication routes has to be identified. Plasma regimes of operation with improved confinement will also contribute to reduce plant size and cost. In the future, high temperature superconductors, when they can be manufactured at sufficiently lower cost, may eventually replace present NbTi and Nb_3Sn superconductors in the magnets, avoiding the use of liquid helium and increasing the reliability of the machine by a larger stability margin.

1.2. ITER magnet system

To achieve a fusion reaction, a high plasma density is necessary. The temperature of the plasma increases with the density to such extreme values that no material withstands direct contact with such plasma. A solution is to confine the plasma using a magnetic field in order to avoid contact with the first wall. The plasma consists of moving charged particles and can therefore be shaped and confined by magnetic field of the tokamak.

The simplest magnetic configuration is a long solenoid, where the magnetic field lines run parallel to the axis of the cylinder. Such a magnetic field prevents charged particles being lost radially, but does not confine them at the ends of the solenoid. To solve the problem the easiest approach is to trap the plasma particles by bending the magnetic field lines around so that they close on themselves in a toroidal shape.

To achieve this, the tokamak reactor was developed in Russia during the 1950s. The tokamak is today's most used design in magnetic confinement fusion experiments.

Tokamak is a Russian acronym for “toroidal chamber with magnetic coils“ [9]. However, a toroidal magnetic field alone would provide poor confinement because its strength decreases radially, so that the particles tend to drift outwards. For complete confinement, an additional poloidal field is required, causing the plasma particles to spin in a helix pattern and thus keeping them constantly moving towards the center of the torus and away from the walls. Most of the poloidal magnetic field in tokamaks is provided by the toroidal current, which flows inside the plasma. Acting as the primary coil of a transformer, the central solenoid induces a current through the plasma, which effectively acts as the secondary coil, that also contributes to heating the plasma through ohmic dissipation. Depending on the specific design of the reactor, additional sets of coils to control the plasma like the Poloidal Field coils, in Figure 1.2, and the Correction Coils in the ITER design are added to the tokamak magnet system which contribute to the plasma confinement.

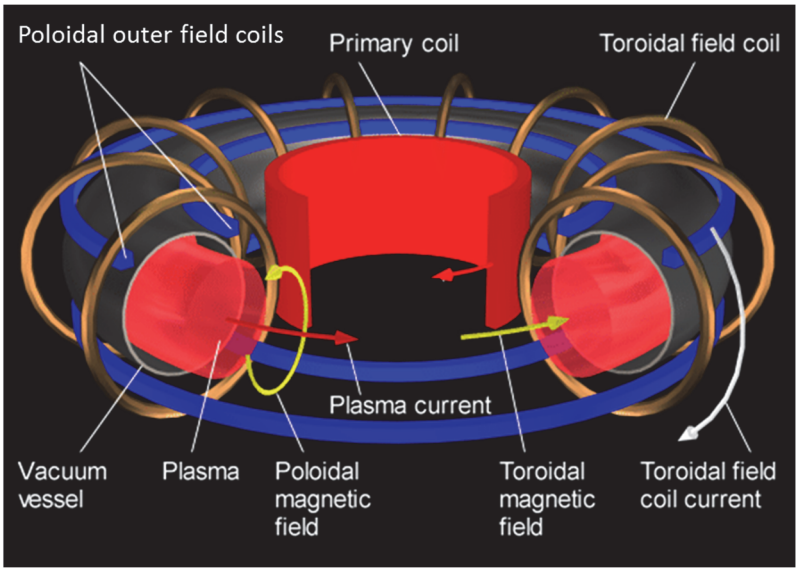

Figure 1.2 – Schematic of a Tokamak fusion reactor: magnetic field confinement scheme, correction coils not shown here).

The ITER project comprises building the world’s largest (830 m^3 of plasma volume) and most advanced experimental tokamak fusion reactor at the Cadarache site in southern France [10]. The ITER magnet system is the largest and most integrated superconducting magnet system with 51 GJ stored energy in the magnets. For comparison, the Large Hadron Collider at CERN, has a stored energy of 11 GJ distributed over 27 km of tunnel [11] and the world’s largest toroidal detector

magnet system, ATLAS, has a stored energy of 1.6 GJ [12]. The ITER machine is expected to demonstrate the feasibility of producing more power from fusion than is used to sustain it, a challenge not yet been achieved by previous fusion reactors. The project goal is an energy gain factor Q of 10, corresponding to an output of 500 MW for 50 MW of input power.

To generate the high magnetic field required to confine the plasma efficiently, the use of superconducting magnets is essential. The ITER magnet system comprises 48 superconducting coils [13], see Figure 1.3:

- 18 Toroidal Field (TF) coils,
- 1 Central Solenoid (CS), composed of 6 modules,
- 6 Poloidal Field (PF) coils,
- 9 pairs of Correction Coils (CC).

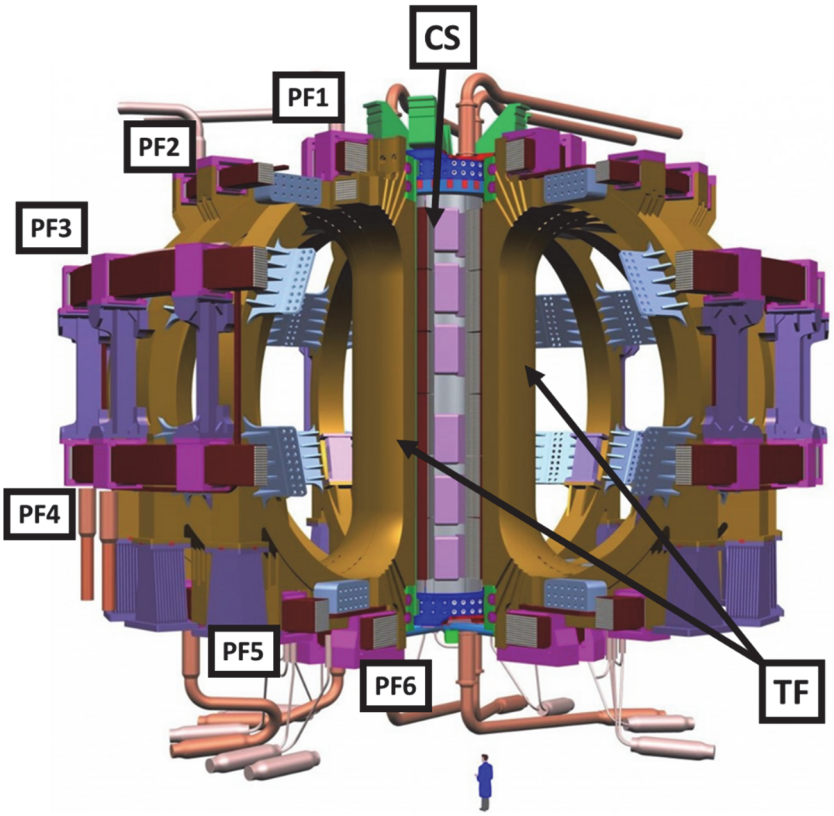

Figure 1.3 – Schematic cross section of ITER magnets [13].

The 18 Torodial Field (TF) coils are designed to carry a steady-state current, generating an average 5.3 T magnetic field around the ITER tokamak torus to confine the plasma particles [14]. The TF coils have a total magnetic stored energy of 41 GJ and a peak magnetic field of 11.8 T. The total toroid weight exceeds 6000 ton and their dimensions make them one of the biggest components of the ITER machine, as each coil is 14 m high and 9 m wide.

The Central Solenoid (CS) is the core of the magnet system, featuring a total height of more than 12 m, an inner radius of 1.3 m and outer radius of 2.08 m. The Central Solenoid is divided in six independent coil modules, in which current can be independently driven to enable the test of various operating scenarios. The Central Solenoid has a peak magnetic field of about 13 T and sustain a magnetic field ramp rate of 1.3 T/s in the inner turns [15].

The Poloidal Field (PF) system consists of six solenoids oriented horizontally and placed outside the toroidal magnet structure, with diameters in the range 8 to 24 m [16], [17].

The Correction Coils are distributed around the tokamak between the TF and PF coils for correcting the error field modes. The type of superconductor, peak operating currents and peak magnetic fields of the ITER magnets are listed in Table 1.1.

Table 1.1 – Type of superconductor, peak operating current and peak magnetic field of the ITER magnets [16], [17].

Coil	*Sc. material*	*Peak current [kA]*	B_{peak} *[T]*
TF	Nb_3Sn	68	11.8
CS	Nb_3Sn	40-45	13
PF	NbTi	48-55	6
CC	NbTi	10	5

Details of the operating scenarios envisaged for ITER operation can be found in [17]. Figure 1.4 shows the currents in the Poloidal Field coils, see Figure 1.3, and in the six modules of the Central Solenoid, see Figure 5.1, during a 15 MA plasma pulse, which represents the reference operating scenario adopted throughout this thesis.

Four main phases can be distinguished from the coil currents point of view:

- Coil charging: in the interval -310 < t < 0 s the currents in the coils are ramped up to their nominal values. The current charge process lasts for 300 s and it is followed by a plateau of 10 s;
- Start of Discharge (SOD): at t = 0 s the SOD occurs, when the currents in the coils are rapidly varied to induce and shape the plasma. Very fast magnetic field variations take place especially in the first 1.5 s but a significant ramp rate is taking place up to 80 s. This phase is most demanding since highest magnetic field, highest forces and highest ramp rates are present requiring particular specification of superconductors and coil structures;
- In the successive phase, between 80 < t < 700 s, the burning plasma is first achieved and then slowly cooled down. This phase is characterized by lower currents and hence lower magnetic field variations;
- In the final phase, between 700 < t < 950 s, all coil currents are ramped down to zero. A long 0 kA current plateau is then maintained for 550 s, after which the successive plasma pulse is initiated by ramping up the currents again.

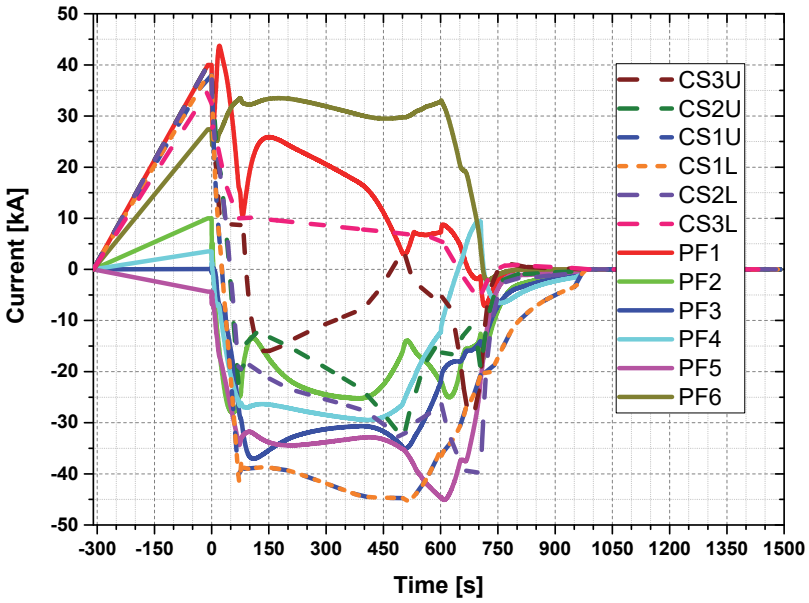

Figure 1.4 – Nominal operating currents in the 6 modules of the ITER Central Solenoid (dashed lines) and the 6 Poloidal Field coils (solid lines) [17]. For t < 0 s currents are ramped up.

1.3. DEMO reactor

The DEMOnstration fusion reactor is intended as the first fusion power plant after the ITER tokamak experimental operation able to produce electricity. The EUROfusion Consortium is leading the conceptual design of the new tokamak system in Europe. The present activities are mainly focused on the Toroidal Field magnet system design. Similar DEMO-like design activities are undertaken by other ITER parties [18], [19].

A large fraction of the work in progress was dedicated to the dimensioning of the Toroidal Field (TF) coil; using Low Temperature Superconductor (LTS) materials, see Figure 1.5. In parallel to the conceptual design and dimensioning of the LTS TF coils, High Temperature Superconductor (HTS) R&D activities were pursued, in continuity with the former program [20].

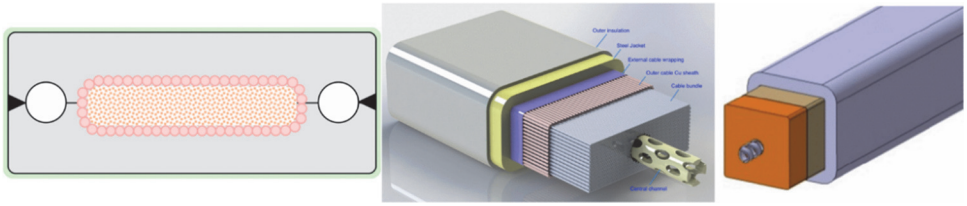

Figure 1.5 – Schematic views of the three initial conductor concepts proposed for the EU DEMO TF coil winding packs. (Left) WP1 is a flat cable composed of twisted sextuplets separated by a steel foil, confined in steel profiles with segregated cooling channels. (Middle) WP2 is a low aspect ratio classically transposed cable, with two perforated tube channels to reduce the helium flow resistance. (Right) WP3 is a square transposed cable with a spiral central channel [20].

WP1, proposed by Swiss Plasma Center, follows the design basis of [21], i.e., high aspect ratio rectangular section, react & wind manufacturing route and a graded layer to layer winding approach. The WP2 design, proposed by ENEA, Italy, is also described in [21] but relies on wind & react manufacturing. WP3, proposed by “Commissariat à l'énergie atomique et aux énergies alternatives”, CEA, France [22], has a square cross section, a wind & react manufacturing route and is based on pancake winding technology. From WP1 to WP3 the degree of technological similarity with respect to the ITER TF design gradually increases although the so-called radial plate concept [23] [24] is not adopted in the DEMO TF design, retaining a relatively broad spectrum of approaches in DEMO. The radial plates are D-shaped stainless steel plates for the ITER toroidal field coils, profiled to contain on each side of the spiral grooves the insulated conductor. In the TF WP designs proposed for DEMO, the rectangular Cable-in-Conduit Conductors (CICCs) are wound in eight

double layers (DL). The layer winding allows the use of a graded superconductor (Nb_3Sn or NbTi, for the different layers) cross section depending on the peak field in the DL, saving about half of the superconductor cost [21]. The different designs are studied to investigate advantages and disadvantages regarding integration in the DEMO machine, e.g., savings on material amount (superconductor, steel) and thus on machine cost, or affect certain manufacturing steps (electrical junctions, winding tolerances) and thus risks in either fabrication or exploitation phases.

1.4. Technical superconductors

Superconductivity is a phenomenon whereby certain materials, when cooled to low temperature, can conduct steady-state currents without electrical resistance. The transition from the normal-conducting to the super-conducting state, occurs at a critical temperature, T_c, characteristic for the material.

The superconducting state is also bounded to a magnetic field lower than the upper critical magnetic field Bc_2, and to current densities below a critical value J_c. The critical temperature, upper critical field and characteristic engineering current density, i.e. the critical current density normalized to the wire/tape cross-section, of the most common practical superconducting materials are summarized in Table 1.2.

Table 1.2 – Critical temperature, upper critical field and characteristic engineering critical current density of practical superconductors [25].

Material	***T_c (0 T) [K]***	***B_{c2} (0 K) [T]***	***J_e (B, 4.2 K) [A/mm^2]***
NbTi	9.3	15	1000 (6 T)
Nb_3Sn	18.3	24-28	700 (15 T)
ReBaCuO	92	160	400 (20 T)
Bi-2223	110	>100	600 (20 T)

In crystal-like superconductors, as Nb_3Sn, the critical behavior is significantly affected by strain as well. In these materials, lattice deformation alters B_{c2} and T_c, while micro-structural cracks limit the transport current. Given the above limits, the performance of a superconductor is generally described by means of a critical surface in the *J-B-T* space. For combinations of the three parameters corresponding to points below the critical surface, the material is in the superconducting state.

The material is instead normal conducting for points above the critical surface. In practical applications of superconductivity, the operating temperature is set around 4.5 K (liquid helium temperature at about 1.3 bar). Therefore, the relevant parameter to characterize the performance of the different superconducting materials is their critical current density variation with the applied magnetic field.

Figure 1.6 illustrates the engineering critical current density dependence on the applied magnetic field at 4.2 K for a number of practical superconductors.

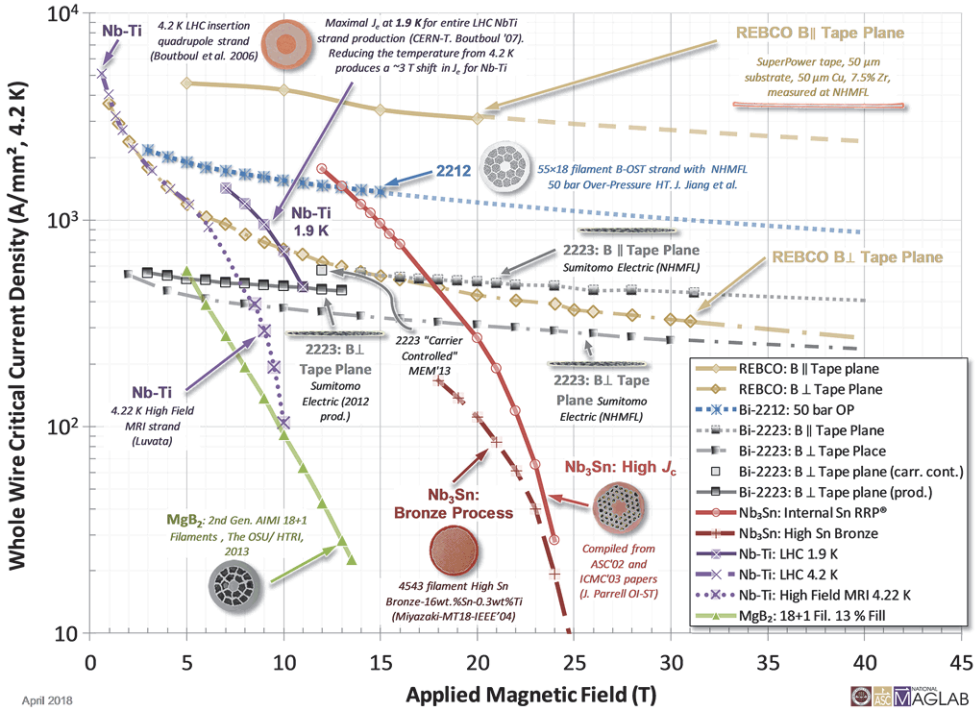

Figure 1.6 – Engineering critical current density versus applied magnetic field for several practical superconductor [25].

For the most used materials, NbTi and Nb_3Sn, the critical current density is accurately modeled as function of temperature, magnetic field and, eventually, strain [26], [27].

The materials used in ITER magnets, described in this thesis are NbTi and Nb_3Sn. The equation used to describe the critical current density $J_c(B,T)$ behavior of the NbTi is [28]:

$$J_c = \frac{1}{B}\left[C_1 \cdot (1 - t^{1.7})^{\gamma_1} \cdot b^{\alpha_1} \cdot (1 - b)^{\beta_1} + C_2 \cdot (1 - t^{1.7})^{\gamma_2} \cdot b^{\alpha_2} \cdot (1 - b)^{ß_2}\right], \quad \textbf{(1.1)}$$

where t is the reduced temperature, b reduced magnetic field and B applied magnetic field. C_1, α_1, β_1, γ_1, C_2, α_2, $ß_2$ and γ_2 are fitting parameters for a specific wire. The normalized temperature is defined as:

$$t = \frac{T}{T_{c0}}, \quad \textbf{(1.2)}$$

where T is the operating temperature and T_{c0} is the critical temperature at 0 T. The normalized magnetic field is expressed by:

$$b = \frac{B}{B_{c2}(T)}, \quad \textbf{(1.3)}$$

where B_{c2} is the upper critical magnetic field at the operating temperature T as given in:

$$B_{c2}(T) = B_{c20}(1 - t^{1.7}), \quad \textbf{(1.4)}$$

and B_{c20} is the upper critical magnetic field at 0 K.

The critical current scaling law equation for Nb_3Sn [27], [29] is :

$$I_c = \frac{C}{B} \cdot S \cdot (1 - t^{1.52}) \cdot (1 - t)^2 \cdot b^p \cdot (1 - b)^q, \quad \textbf{(1.5)}$$

where t is the normalized temperature, b normalized magnetic field, S strain dependent term and B the applied magnetic field. C_1, p and q are fitting parameters for the specific wire. The normalized temperature is defined as:

$$t = \frac{T}{T^*_{c0}(\varepsilon)}, \quad \textbf{(1.6)}$$

with

$$T^*_{c0}(\varepsilon) = T^*_{cm} \cdot S^{\frac{1}{3}}, \quad \textbf{(1.7)}$$

and T^*_{cm} is the inhomogeneity averaged critical temperature. The normalized magnetic field is:

$$b = \frac{B}{B^*_{c2}(\varepsilon, T)}, \tag{1.8}$$

where

$$B^*_{c2}(\varepsilon, T) = B^*_{c2m}(0) \cdot S \cdot (1 - t^{1.52}). \tag{1.9}$$

$B^*_{c2m}(0)$ is the inhomogeneity averaged upper critical magnetic field at 0 K. The strain dependent term S is expressed as:

$$S = \frac{C_{a,1} \cdot \left[\sqrt{\varepsilon^2_{shift} + \varepsilon^2_{0,a}} - \sqrt{\left(\varepsilon_{axial} - \varepsilon_{shift}\right)^2 + \varepsilon^2_{0,a}}\right] - C_{a,2} \cdot \varepsilon_{axial}}{1 - C_{a,1} \cdot \varepsilon_{0,a}} + 1, \tag{1.10}$$

where $C_{a,1}$ and $C_{a,2}$ are the second and third invariant of the axial sensitivity, ε_{axial} is the axial strain [30], $\varepsilon_{0,a}$ is the residual strain component and ε_{shift} is the measurement related strain given by:

$$\varepsilon_{shift} = \frac{C_{a,2} \cdot \varepsilon_{0,a}}{\sqrt{C^2_{a,1} - C^2_{a,2}}}. \tag{1.11}$$

In the ITER magnet system, NbTi is used for the PF and CC coils, where magnetic fields are lower than 6 T. Nb_3Sn is adopted for the CS and TF coils, where higher magnetic fields are required.

Nb_3Sn and NbTi are low temperature superconductors that need to be cooled with liquid helium. As visible in Figure 1.7, the specific heat of Nb_3Sn material at cryogenic temperature is dramatically lower than at room temperature; about 3000 times lower [31].

Consequently, even a small energy release in the conductor causes a significant temperature rise. This may lead to a quench in the superconductor. A quench is an unwanted and irreversible avalanche-like transition from superconducting to normal state, where after coils have to be switched off. They are heating up and need to be re-cooled for restoring operational conditions.

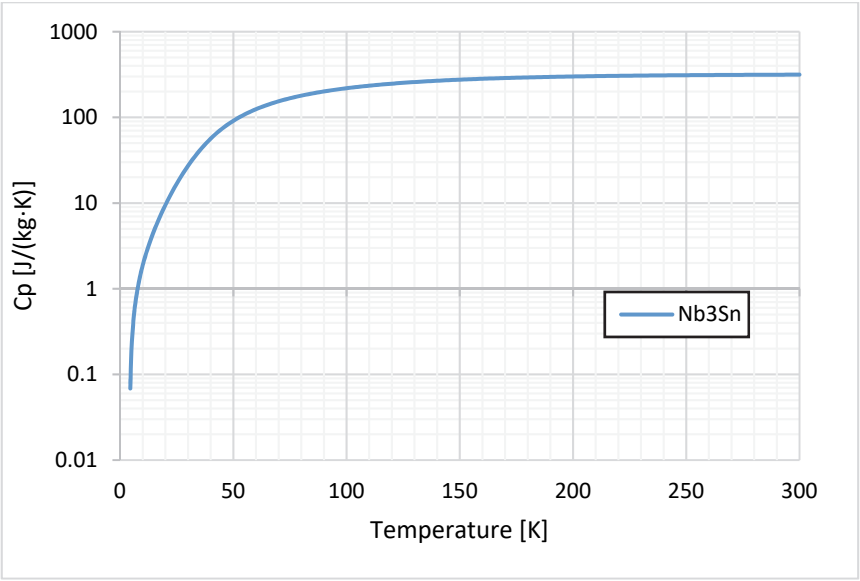

Figure 1.7 – Specific heat at constant pressure versus temperature for Nb_3Sn strand [31].

To avoid quenches, the magnets are designed to have a certain temperature margin, ΔT, large enough to ensure reliable operation even with the most critical operating scenarios. The temperature margin is defined as [32]:

$$\Delta T = T_{cs} - T_{op}, \tag{1.12}$$

where T_{cs} is the current sharing temperature and T_{op} is the operating temperature.

The temperature at which the critical current equals the operating current is called current sharing temperature T_{cs}, defined as:

$$\mathrm{T_{cs}}(B,I) = T_{op} + \left[T_c(B) - T_{op}\right]\left[1 - \frac{I_{op}}{I_c}\right]. \tag{1.13}$$

Above T_{cs}, the superconductor develops a resistance and the current flow is associated with Joule heating. The superconductor develops a longitudinal resistive voltage when the operating temperature is between T_{cs} and T_c, and part of the current is shared between superconductor and stabilizer. The transition from superconducting to normal state is not sharp, but smooth over a temperature range. Therefore, the transition from superconductive to normal-state, in quasi-stationary conditions, is defined as the value at which the longitudinal electric field of E_c = 10 μV/m is reached along the sample. As a consequence the E_c = 10 μV/m is

used as criterion to establish the boundaries between superconductive and normal-state conditions.

1.4.1. Strands and CICCs

For stability and AC loss reasons [33], practical superconductors are shaped into wires (diameters often in the range 0.7-1.5 mm) also called strands when used in a cable. Every strand is made of a large number of thin superconducting filaments (diameter in the range 1-50 μm) twisted and embedded in a low-resistivity matrix of normal metal, usually copper. In the case of Nb_3Sn strands also bronze is present around the filaments and low-resistivity copper is added separated by a Ta and Nb barrier. The main specification of ITER NbTi and Nb_3Sn strands is detailed in Table 1.3, while few characteristic strand cross-sections are shown in Figure 1.8.

Since the resistivity of the superconducting material above their critical temperature T_c is relatively high, a low-resistive parallel path for the current is necessary in the case of a transition to the normal state. This, because an excessive ohmic heating can even cause melting of the conductor in the worst-case scenario. The matrix materials (Cu for NbTi, CuSn/Cu for Nb_3Sn, Ag for BSCCO-2212 and steel/Cu for ReBCO), exhibits an electrical resistivity that is several orders of magnitude lower than the one of the filaments in the normal state.

Filament diameters below 8 μm are required for the ITER strands to minimize the AC hysteresis loss, as detailed in Table 1.3. The subdivision into small filaments is also required to obtain sufficient stability of the strands against local thermal disturbances, allowing fast heat and current transfer to the surrounding matrix. Filament twisting is introduced to reduce inter-filament coupling currents induced by time-varying magnetic fields. In twisted wires, the magnetic flux linked to the current loops changes sign every half-twist pitch. For sufficiently short twist pitches, not enough space is available for large transverse currents to build up. Relatively hard and highly-resistive coatings are applied to the strands, usually Ni for NbTi and Cr for Nb_3Sn, to reduce their coupling in the final cable.

The same strategy is used for cabled conductors, composed of several hundreds of strands. The resistance of the inter-strand contacts influences the conductors coupling loss. Therefore, it has to be carefully controlled to keep the heat below an acceptable level. At the same time, the inter-strand contact resistance affects the electro-magnetic and thermal stability also influencing the current sharing among the strands. The inter-strand resistance should not be too high to allow sufficient

current redistribution. These two phenomena define a safe and reliable operation range of magnets made with cabled conductors.

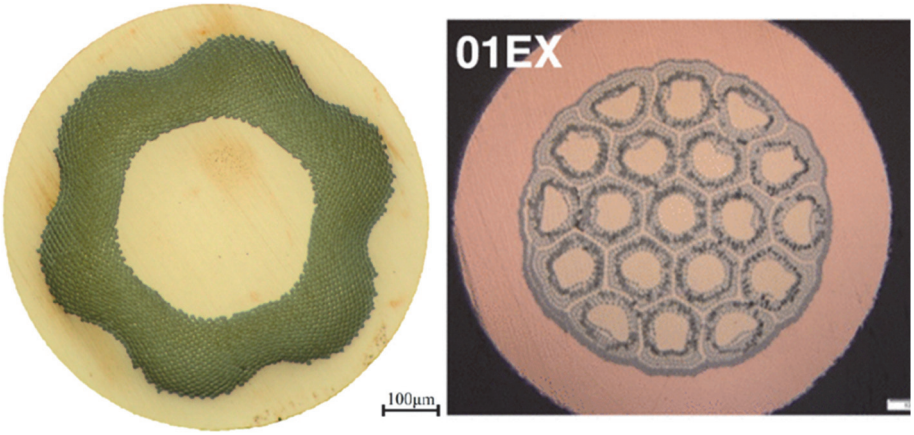

Figure 1.8 – Transverse cross-section of a NbTi strand for the ITER Poloidal Field conductors produced by Western Superconducting Technologies (WST), China [34] (left). Transverse cross-section of a Nb_3Sn strand for the ITER Central Solenoid conductors produced by Kiswire Advanced Technology (KAT), Korea [35] (right).

Table 1.3 – Specification of the ITER PF NbTi and CS Nb_3Sn strands [36], [37].

	NbTi	***Nb_3Sn***
Strand diameter [mm]	0.730 ± 0.005	0.830 ± 0.005
Twist pitch [mm]	15 ± 2	15 ± 2
Twist direction	Right hand	Right hand
Ni/Cr Plating thickness [μm]	2.0 + 0 – 1	2.0 + 0 – 1
Cu:nonCu ratio	2.3 – 0.05/+ 0.15	1.0 ± 0.1
Filament diameter [μm]	≤ 8	≤ 5
Residual-resistance ratio (RRR)	> 100	> 100
Critical current [A] at 4.22 K and B_{ref}	339 (B_{ref} = 5 T)	≥ 228 (B_{ref} = 12 T)
Resistive transition index in the 10-to-100 μV/m range at 4.22 K and B_{ref}	> 20 (B_{ref} = 5 T)	> 20 (B_{ref} = 12 T)
Max. hysteresis loss [mJ/cm^3] per strand unit volume at 4.22 K at B_{cycle}	55 (B_{cycle} = ± 1.5 T)	500 (B_{cycle} = ± 3 T)

To achieve the high current necessary for generating the ITER magnetic fields and to minimize the self-inductance of the coils to allow fast current variation, many strands are cabled as illustrated in Figure 1.9.

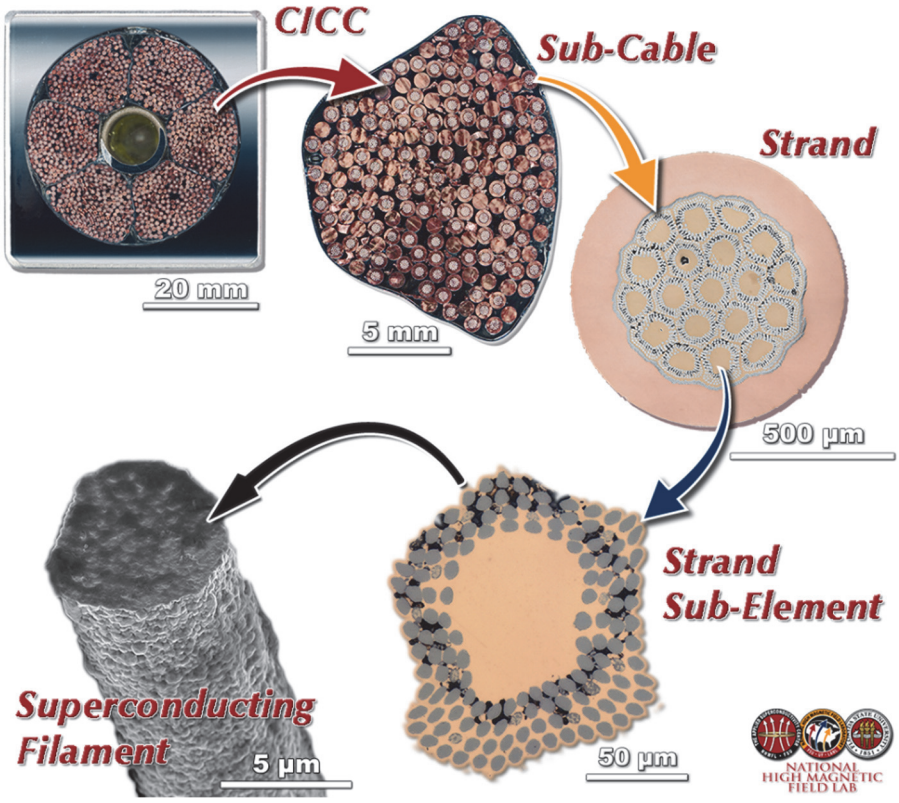

Figure 1.9 – Components of one of the superconducting Cable-In-Conduit Conductor for ITER Central Solenoid [38].

The design of ITER coils is based on the Cable-In-Conduit Conductor (CICC) concept, where hundreds of strands are twisted in multiple cabling stages around a central spiral, and then inserted in a metal jacket [36], [39]. The jacket surrounding the cable provides mechanical reinforcement by taking up most of the Lorentz force in the coil windings during operation.

For cooling forced flow, supercritical helium is in the interstices between the strands and the central channel. The forced helium flow combined with the strand-coolant contact results in a high cooling capacity, which is fundamental for the stability against significant power dissipation. A central channel delimited by a

metal spiral is usually added to reduce the helium pressure drop, while facilitating helium circulation between the strand bundles.

Copper strands can be included in the cable for creating sufficient cross-section for a low-resistivity current path in the case of a quench, improving the stability and reducing the hot-spot temperature during a local quench. Metal barriers (wraps) are added around the last stage sub-cables (petals) to reduce inter-petal coupling currents in pulsed operation. The main specifications of the ITER CIC Conductors are detailed in Table 1.4.

Table 1.4 – Specification of the ITER Poloidal Field and Central Solenoid coils CICCs [36].

	PF1-6	***CS***
Cable pattern	3Sc x 4 x 4 x 6 x 6	(2Sc+1Cu) x 3 x4 x 4 x 6
Central spiral [mm]	10 x 12	7 x 9
SS petal wrap	0.05 mm thick 50% coverage	0.05 mm thick 70% coverage
SS cable wrap	0.1 mm thick 40% coverage	0.08 mm thick 40% coverage
Nr. of Sc. strands	1440	576
Nr. of Cu strands	0	288
Void fraction [%]	34.3	33.5
Cable diameter [mm]	37.7	32.6
Jacket size [mm]	Circle in square 53.8 x 53.8	Circle in square 49 x 49
Jacket material	316L	JK2LB
Petal Wrap coverage [%]	40	70

1.4.2. AC loss

Two main mechanisms can be identified in superconducting cables that contribute to the overall loss under time-dependent current and magnetic field conditions, so called AC loss.

Hysteresis loss is caused by the movement of flux lines within the superconducting material due to changes in magnetic field or transport current. When flux lines move, a resistive loss occurs [33], [40]. Under time-dependent conditions, inter-filament coupling currents are induced across the resistive matrix material between different filaments, causing a resistive inter-filament coupling current loss [33], [41].

Inter-strand coupling currents are the equivalent of inter-filament coupling currents but among strands. When the inter-strand contact resistances are low enough, significant induced currents are passing across the strand interfaces causing noticeable dissipation [42], [43].

Hysteresis loss

In a superconducting filament exposed to a varying magnetic field, shielding currents of density ± J_c are generated in the outer layer. They screen the interior of the filament from the change of magnetic field. The case of a round filament without transport current in transverse magnetic field is illustrated in Figure 1.10. While the magnetic field rises, the screening current boundary shifts towards the center of the filament, because J_c is limited. The so-called full-penetration magnetic field, B_p, is reached when the screening current arrives to it's maximum at the center of the filament.

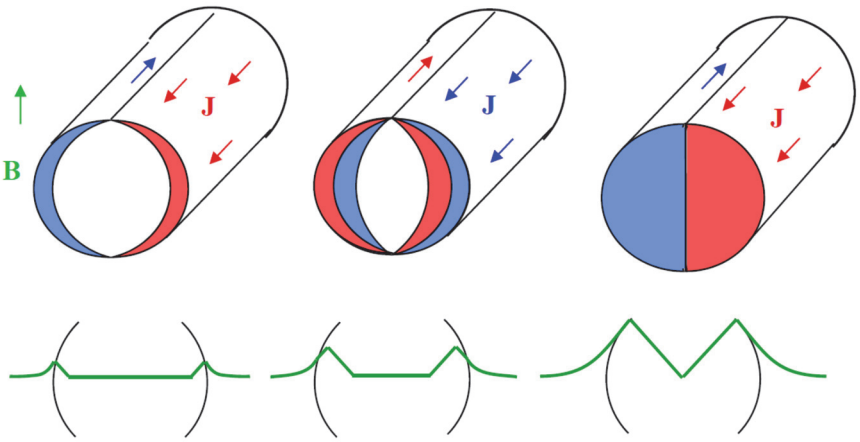

Figure 1.10 – Screening current density and magnetic field profiles in a superconducting filament subjected to a transverse time-varying magnetic field *B*.

For transvers of magnetic field the penetration field can be expressed as:

$$B_p = \frac{\mu_0 J_c d_f}{\pi}, \tag{1.14}$$

where d_f is the filament diameter.

The magnetic momentum per unit of volume, called magnetization *M*, produced by the screening current generated by parallel and transverse magnetic field is given as:

$$M_{par} = \frac{J_c d_f}{6}, \tag{1.15}$$

$$M_{tra} = \frac{2J_c d_f}{3\pi}. \tag{1.16}$$

The energy dissipated per magnetization cycle in a unit volume is the circulation integral of the hysteresis loop and can be expressed as: (see Figure 1.11):

$$Q_{hyst} = \oint M dB. \tag{1.17}$$

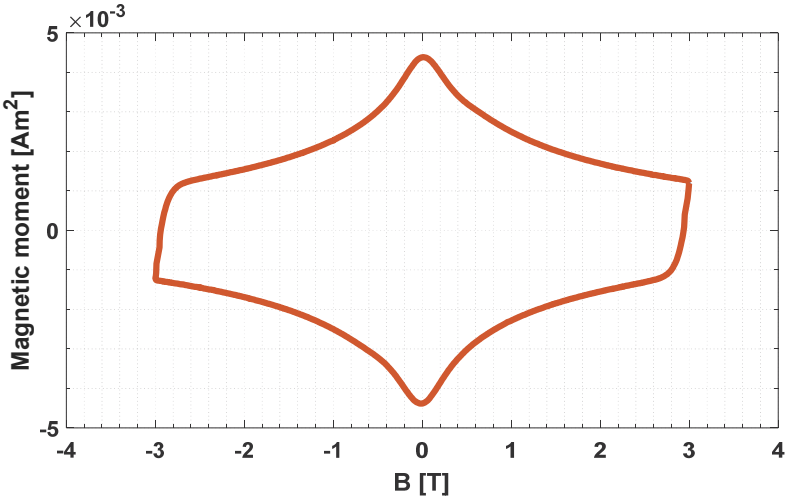

Figure 1.11 – Magnetization versus applied magnetic field in a Nb_3Sn strand at T = 4.2 K, B_a = 3 T and f = 10 mHz [44].

Eq. (1.17) can be also expressed in terms of power loss per unit of superconductor volume:

$$P_{hyst} = \frac{2}{3\pi} J_c d_f \left|\frac{dB}{dt}\right|. \tag{1.18}$$

In presence of a stationary transport current I_t, the magnetization is reduced. However, the loss is increased roughly by a factor $1 + \left(\frac{I_t}{I_c}\right)^2$:

$$P_{hyst} = \frac{2}{3\pi} J_c d_f \cdot \left(1 + \left(\frac{I_t}{I_c}\right)^2\right) \cdot \left|\frac{dB}{dt}\right|. \quad \textbf{(1.19)}$$

For closely packed filaments, practically in contact, as for some of the ITER strands, proximity effects between filaments can influence the hysteresis loss. Cooper pairs [45] can cross the normal material of the strand matrix by tunneling. In this case, the effective strand diameter d_{eff}, corresponding to the size of the bundle of filaments, rather than the single filament, has to be used in Eq. (1.18) and Eq. (1.19) [35].

Coupling loss

Figure 1.12 shows a multi-filamentary wire subjected to a uniform external magnetic field B_a, varying with rate *dB/dt*. The arrows show the inter-filament coupling currents. Coupling current flows along the filament and crosses the matrix every half twist pitch. The current crossing the matrix follows mainly a path parallel to the changing magnetic field.

The coupling currents generate an almost perfect dipole field in the strand interior. Therefore, a uniform internal magnetic field B_i is generated by the coupling currents:

$$B_i = B_a - \dot{B}_i \tau, \quad \textbf{(1.20)}$$

where:

$$\tau = \frac{\mu_0}{2\rho_t}\left(\frac{L}{2\pi}\right)^2, \quad \textbf{(1.21)}$$

where L is the twist pitch and ρ_t the transverse inter-filamentary resistivity. The time constant of the system is called τ and it represents the time needed by the coupling currents to decay after the external magnetic field has stopped changing.

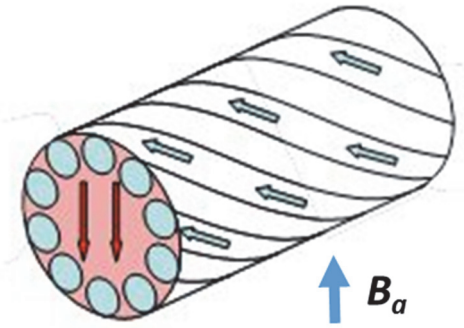

Figure 1.12 – Twisted multi-filamentary strand in a variable transverse magnetic field showing the path used to calculate the flux linkages.

The power per unit volume dissipated by the induced currents is obtained integrating $J^2\rho_t$ along the current path, which results in:

$$P_{cpl} = \frac{\dot{B_l}^2}{\rho_t} \cdot \left(\frac{L}{2\pi}\right)^2 = \frac{2\dot{B_l}^2}{\mu_0} \cdot \tau. \qquad \textbf{(1.22)}$$

The loss per cycle due to a sinusoidal magnetic field of amplitude B_a is given by:

$$Q_{cpl} = \frac{B_a^2}{\mu_0} \cdot \frac{2\pi\omega\tau}{1+\omega^2\tau^2}. \qquad \textbf{(1.23)}$$

Both, eq. (1.22) and eq. (1.23) were derived for a wire with circular cross-section. In order to generalize the formulas, the coefficient *2* has to be replaced by the effective shape factor *n* of the wire. Detailed treatments of the inter-filament coupling loss for different cross-sectional shapes, types of magnetic field variation and frequencies can be found in references [33], [40], [41], [46], [47].

Apart from a factor related to the geometry, the inter-filament coupling loss depends on a single parameter τ determined by the twist pitch and the effective transverse resistivity, which is a function of the filament-to-matrix contact resistance, effective matrix resistivity and cross-sectional layout of the filaments. The behavior can be compared to the characteristics of an LR circuit, by which the resistance is the transverse resistivity per unit length; the twist pitch determines the self-inductance; the driving voltage is caused by the changing magnetic field.

Inter-strand coupling loss is generally treated analogously to inter-filament coupling loss. Assuming the condition of full penetration of the magnetic field, the hysteresis loss is almost independent of the frequency. The magnetic field applied in eq. (1.23) has a sinusoidal profile, $B_a(f) = B_a sin(2\pi f t)$, and n is the shape factor of the wire. The initial linear section of the loss versus frequency curve with slope α, represents the coupling loss, $Q_{cpl}(f)$ and provides the effective coupling current time constant $n\tau$ as following:

$$n\tau = \frac{\alpha \mu_0}{2\pi^2 B_a^2}. \quad \textbf{(1.24)}$$

The $n\tau$ can be used for calculation of the AC loss at low magnetic field ramp rate. At higher ramp rates, the coupling loss saturates and decreases with frequency because of the shielding of the interior of the conductor. Depending on the cable geometry, it is possible to have a large number of different coupling current paths, due to multiple strand contacts and various contact resistances and current loops. The contact resistance depends strongly on the strand and cable production and on the operation history [42], [48]. As a consequence, in multi stage cables there can be multiple time constants without even a dominant one. In fact, the loss, represented by a particular time constant, is created in a particular region of the cable. The different current loops can be saturated or shield others [30].

Therefore, eq. (1.22) and eq. (1.23) are also used for a cable but now using an effective time constant τ_{eff} defining the initial slope of the AC loss versus frequency curve:

$$n\tau_{eff} = \sum_{i=1}^{N} n_i \tau_i. \quad \textbf{(1.25)}$$

This concept offers an easy treatment of any number of cabling stages analytically although the individual parameters are obtained by fitting and are only valid for the experimental conditions. Consequently, this model is used for the analytical calculation of inter-strand coupling loss in CICCs, in section 2.3.

In practice, the analytical models show relatively high uncertainty for scaling to conditions other than the experimental condition like e.g. higher magnetic field amplitudes. The best solution is using a detailed numerical model with all the strand paths incorporated in the geometry and with the correct inter-strand resistance matrix. Such model, called JackPot AC/DC, has been created at the University of

Twente featuring detailed analysis of coupling loss, current distribution and stability of CICCs [49], [50], [51], [52], [53], [54].

1.4.3. Stability

To achieve the specified repetition rates of plasma cycles in ITER and proper operation of the tokamak, it is essential to build magnets with a well-proven stability margin. Reduced stability implies significant loss in terms of operation time, efficiency and money. If a quench occurs, it is necessary to re-cool the magnets to their operating temperature, which causes interruption of the operation. In the worst case, a quench can cause damage of the conductor if the temperature of the hot spot and stress in the system are not properly controlled. Various phenomena can occur in superconducting cables that limit their performance [55].

Current unbalance among the strands originates by the natural spread in the contact resistances between strands. When, because of the current non-uniformity, the current in a given strand exceeds the critical current determined by the local magnetic field and temperature, a transition to the normal state occurs. The successive evolution of one initial normal zone into a quench or into recovery of the conductor depends on the possibility for the saturated strand to expel excess current into the surrounding strands.

The exposure to time-varying magnetic field induces currents in multi-strand cables, both within the individual strands and between them. The flow of coupling currents through the resistive parts of strands and cable produces ohmic heating, and thus temperature increase. Such loss can therefore potentially lead to a quench. Moreover, the addition of induced coupling currents can cause the strand total current to become higher than the critical current, leading to local normal zones in strands and eventually quench of the entire conductor.

Low-resistive contacts allow a reduction of ohmic heating and possibly improved current uniformity by facilitating current sharing among strands. On the other hand, highly resistive barriers around strands and petals are required to limit eddy, inter-strand and inter-cable coupling currents introduced by pulsed operation. As in most superconductivity applications, these two opposing requirements necessitate a carefully balanced design of strands, cables and joints.

1.5. Scope of the thesis

The scope of the thesis is to enhance understanding CICCs performances by studying and modeling the stability behavior of CICCs of the ITER magnet system, with particular attention to the conductors of the Central Solenoid coil. The ultimate goal is to explore a thermal and electromagnetic stability threshold to be applied for optimized design of the next generation conductors for DEMO.

The results of the experiments performed on short conductor samples are essential for the ITER magnet research, but practical test conditions differ significantly from the real operating plasma scenario. Simulation based on properly developed models is the only way to test the conductors under realistic plasma scenario operating conditions. The codes JackPot AC/DC and THEA, described both in Chapter 2, are used in this thesis to analyze the performance of CICCs for ITER and DEMO magnets.

The structure of the thesis is shown in Figure 1.13.

- Chapter 2 presents the SULTAN test facility, its experiment design and characteristics. The measured conductor sample results are used to validate the stability models of the CICCs. An overview of the models, JackPot AC/DC, THEA and MPAS, is also given in this chapter, highlighting the main properties of the three models.

- In Chapter 3 the MPAS-THEA stability model is validated for NbTi type Poloidal Field CIC Conductor; the results are compared to JackPot results for the same PF conductor.

- In Chapter 4 MPAS-THEA and Jackpot-THEA models are validated for Nb_3Sn CS conductor. The stability tests performed in the SULTAN facility are analyzed using the two models. Stability predictions for slow magnetic field pulse are simulated for the CS conductor using JackPot-THEA.

- Chapter 5 connects the stability simulations, performed with the JackPot-THEA model, to the ITER 15MA plasma scenario of the Central Solenoid. The electromagnetic and thermal performances of the coil are compared to the short sample simulations.

- In Chapter 6, JackPot is validated for the DEMO TF Nb_3Sn model conductors. Coupling and eddy current losses are modeled and compared with measured performance. The stability behavior of the DEMO CIC Conductors is finally compared to the CS ITER conductor results.

- Chapter 7 presents the conclusion of the PhD work.

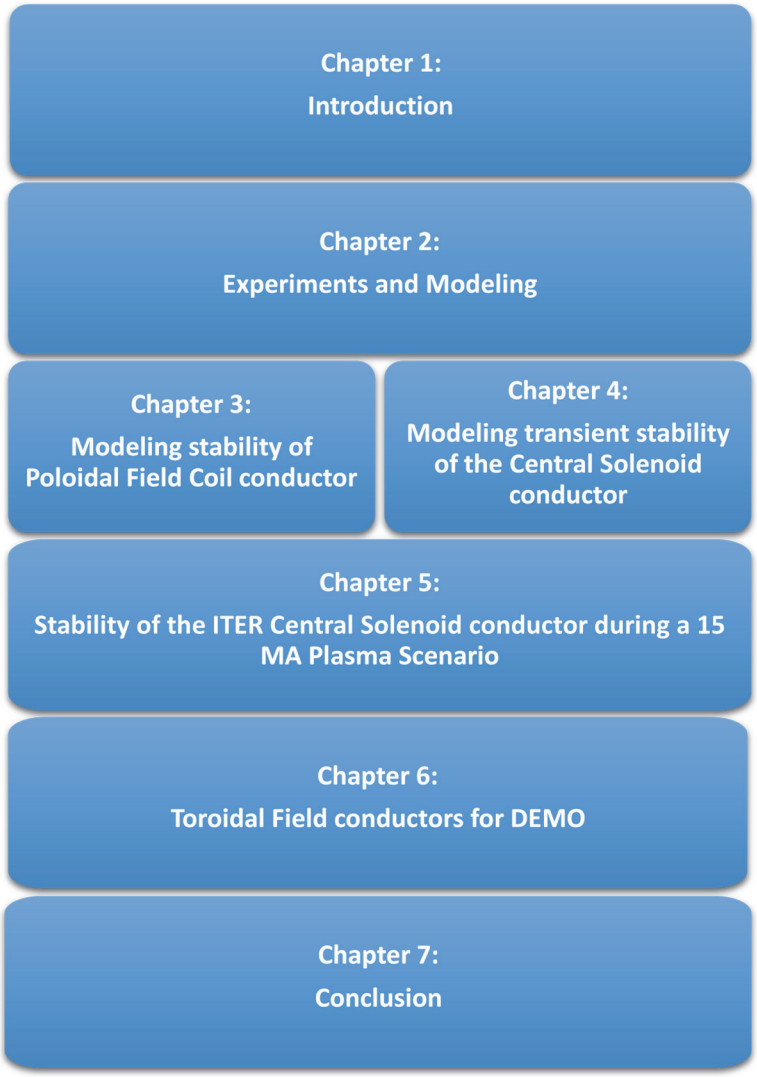

Figure 1.13 – Outline of the thesis showing the relation between chapters.

2. EXPERIMENTS AND MODELING

2.1. Introduction

ITER will be the largest fusion facility in the world with a tokamak superconducting magnet system including NbTi and Nb_3Sn Cable-In-Conduit Conductors (CICC). All ITER conductors have to follow a strict qualification program mostly performed at the SULTAN facility of the Swiss Plasma Center (SPC) and includes current sharing temperature, AC coupling loss and stability tests on short full size conductor samples [56]. Due to the high cost of tests, limited length of the samples and, for some conductors, magnetic field and magnetic field rates lower than the peak values in ITER, especially for Nb_3Sn, dedicated simulation are necessary to extend the comprehension of the CICCs behavior.

The simulations presented here are based on samples tested in SULTAN. A short introduction on the SULTAN experimental facility and the tests performed on the ITER samples are also shown.

Different models are applied for the analysis of the NbTi and Nb_3Sn conductors. The JackPot AC/DC numerical model developed at the University of Twente, is used to analyze electromagnetic and thermal behavior of CICCs at strand, cable and coil levels. The Model with PArtial Shielding zone (MPAS) is an analytical model and is used to fit and express the CIC Conductors' coupling loss. Both are also used in combination with THEA (Thermal, Hydraulic and Electric Analysis of Superconducting Cables) [57], a 1-D model to analyze the superconducting thermal and hydraulic behavior of CIC Conductor. The main properties of the models are presented.

2.2. SULTAN facility

The SUpraLeiter Test ANlage (SULTAN) facility of the Swiss Plasma Center (SPC) is at the moment the most appropriate magnet facility to test short sections of full-size sample superconductors in forced flow helium condition in a background magnetic field up tp 10.85 T [58]. A second facility now for coil windings is present at the ITER Central Solenoid Model Coil facility in Naka (Japan) [59].

2.2.1. SULTAN Setup

The NbTi conductor samples for test in SULTAN are generally made from one conductor unit length bent in a hair pin U-shape [60], while the Nb_3Sn conductors samples are made of two conductor sections of the same length joined at one end in a praying hand configuration obtaining a hair pin shaped joint [61]. The central channel of the conductor is blocked; thus, the helium is forced to flow only in the voids between the strands with a mass flow rate of 1 to 10 g/s. The instrumentation was optimized for the qualification of the ITER samples [62], [63]. The sample voltage taps and temperature sensors are located upstream and downstream the High Field Zone (HFZ), see Figure 2.1. The sensors are usually four and they are attached to the jacket, one for each side of the conductor cross section. The longitudinal distance between the voltage taps is 450 mm, which is about to the length of the HFZ while the distance between the temperature sensors is 800 mm.

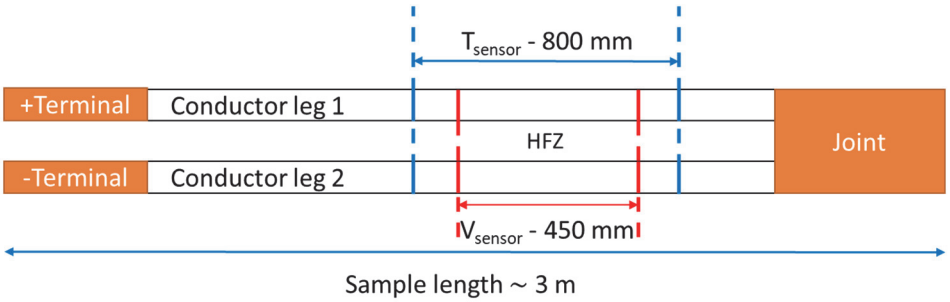

Figure 2.1 – Schematic of SULTAN sample instrumentation, voltage taps and temperature sensors. Voltage taps and temperature sensors are located upstream and downstream the HFZ at 225 mm and 400 mm distance from the center, respectively.

In the SULTAN facility, the sample is vertically inserted in the magnet bore and the upper terminations are electrically connected to the current leads of the superconducting transformer [58]. The SULTAN magnet system comprises a stationary split coil system and an AC and pulsed coil. The stationary magnet system is able to generate up to 10.85 T with a HFZ of about 500 mm. The spit coil gap is about 100 mm, and allows a straight short conductor sample to be positioned in the HFZ. The AC magnet consists of two saddle shaped coils, placed in the HFZ bore of the DC coils. The saddle coil is orientated to generate an AC or a pulsed magnetic field perpendicular to the DC field, see Figure 2.2. The effective magnetic field length of the AC coil is 390 mm. The coil can generate a sinusoidal varying magnetic

field on the conductor to induce AC loss and if required a quench when used for Minimum Quench Energy (MQE) tests.

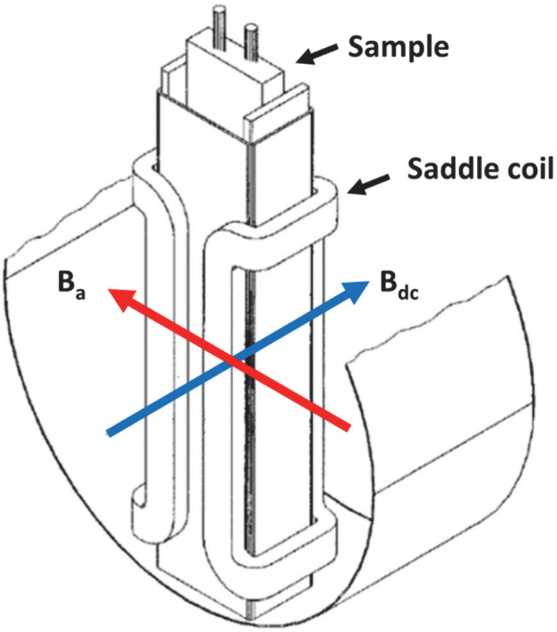

Figure 2.2 – Orientation of the AC/pulsed saddle coil magnetic field with respect to the stationary field and sample [58].

2.2.2. SULTAN test procedure

The tests performed on the CICCs comprise so-called DC and AC tests [56]. The aim of the DC test is to measure the current sharing temperature T_{cs}, and critical current I_c, of the conductor, and check compliance with the ITER requirements. The current sharing temperature is measured by injecting the operation current in the conductor and raising the temperature stepwise until a thermal run-away, or quench, occurs. The average voltage from the voltage taps is used to determine the electric field evolution in the conductor. The electric field criterion that defines the T_{cs} of the ITER conductor is E_c = 10 μV/m. The critical current and transition steepness are measured in a separate test by holding the conductor temperature at the previously measured T_{cs} and increasing the operation current up to the transition from superconducting to normal state.

The AC tests consist of AC loss and stability measurements. The AC loss measurements comprise a series of runs where a continuous sinusoidal magnetic field generated by the AC coil is varied in the frequency range of 0.1 to 5 Hz while the amplitude generally is fixed at 0.2 T. The power loss generated is measured with a calorimetric method [64]. The error declared by SULTAN in AC loss measurements is within 5% for a frequency below 5 Hz.

The stability tests are performed to define the Minimum Quench Energy (MQE) of the conductor. Generally, it is possible to deposit a large amount of energy in a magnet without causing a quench. In this case, the conductor is able to recover to the initial condition after the energy deposition. If the conductor is not able to recover, it will quench. The Minimum Energy necessary to initiate the Quench is called MQE [65]. Different from the AC loss measurements, during the stability tests the energy is deposited using a single sinusoidal magnetic field wave, see Figure 2.3.

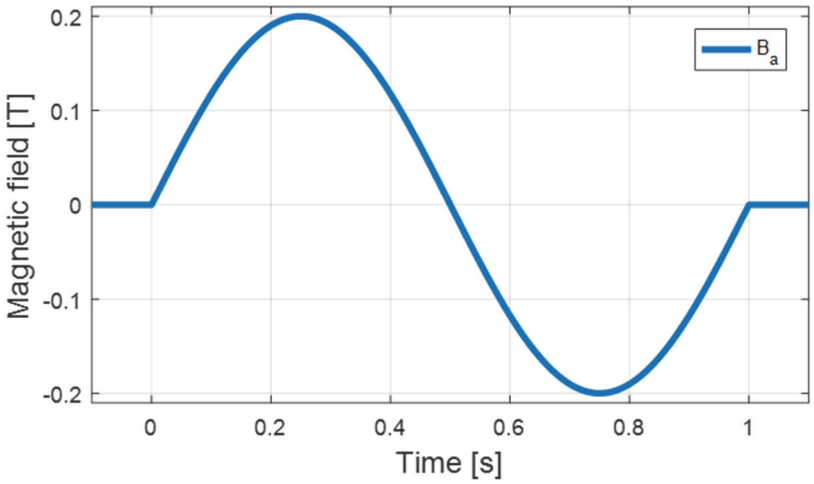

Figure 2.3 – Ideal single sinusoidal magnetic field wave applied during an MQE test in SULTAN.

Due to the complexity of the conductor and the length of the region where the coupling- and eddy current losses are generated, it is impossible to define the exact location where the quench starts, defining a local MQE. Therefore, the MQE, measured during the stability tests, is a global MQE. To achieve a single sinusoidal-like wave, a capacitor bench with 10 capacitors of 4 mF each, is connected to the coils in order to build an RLC circuit with 7.8 Hz resonating frequency (128 ms of time period). The capacitor discharge generates an almost perfect sinusoidal

magnetic field wave that can be cut either after one or half period. To reach the MQE, the amplitude of the pulse is stepwise increased until the quench occurs. Due to the facility limitation, the maximum magnetic field pulse amplitude available is about 0.5 T which is insufficient to initiate a quench from the operating conditions. Therefore, it is necessary to increase the temperature, in order to initiate a quench. The temperature of the sample is modified by varying the temperature of the helium at the sample inlet. The temperature of the helium is set by controlling a heater in the cooling channel. Therefore, the higher the temperature needed in the test the higher is the amount of heat necessary to inject in the helium. The helium temperature is controlled using as reference the temperature sensors placed on the conductor jacket in the high-field zone. This control system generates fluctuations in the coolant temperature at elevated temperature, above 8 K. The temperature fluctuation propagates in the conductor generating unpredictable errors. The temperature instability combined with the high frequency of the test (>5 Hz) generates an error in the energy measurements higher than 5%. The error related to the stability measurements is considered 10%. See appendix A for the assessment of the energy calculation during the stability tests with temperature fluctuations.

It is important to note that the testing condition refers to the peak magnetic field, while the SULTAN test program refers to the background magnetic field applied to the conductor in the HFZ. The peak magnetic field applied to the conductor can be approximated as background magnetic field plus the self-field generated by the test current in the two conductor legs, using eq. (2.1):

$$B_{peak} = B_{dc} + \frac{\mu_0 I_{op}}{2\pi} \cdot \left(\frac{1}{R} + \frac{1}{a - R}\right), \quad \textbf{(2.1)}$$

where B_{dc} is the background magnetic field, I_{op} is the operation current, μ_0 the magnetic permeability in vacuum, R is the conductor bundle radius and a is the distance between the centers of both legs [66].

2.2.3. Sultan AC magnetic field amplitude during MQE tests

To be able to simulate with a model the conductor when exposed to the SULTAN stability tests, it is mandatory to know the magnetic field amplitude applied by the AC coil. The applied magnetic field is not measured directly but is deduced knowing the coil design, the field-to-current ratio B/I of $8.69 \cdot 10^{-4}\ T/A$, the ratio between the full wave field excursion and the set voltage $\Delta B/V = 2.86\ T/kV$ [58].

Most of the work presented here is based on measurements on the ITER conductor qualification samples referred to as PFEU2 [67] and CSJA8 [68], see Figure 2.4. Both samples will be thoroughly analyzed in the subsequent chapters. Next an example of the applied magnetic field pulse calculation is shown.

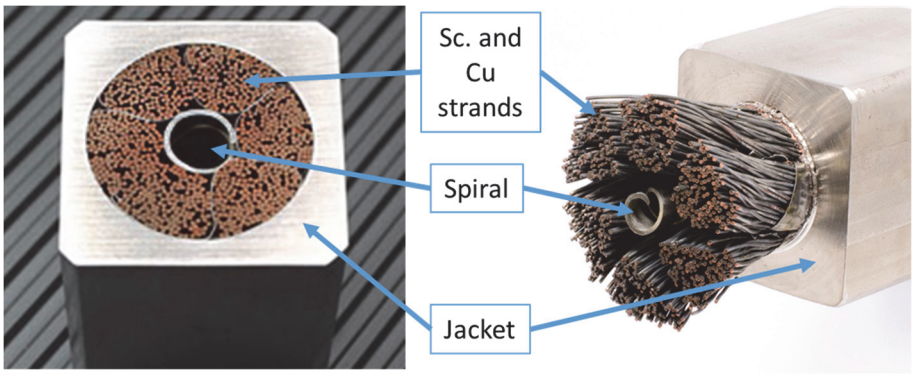

Figure 2.4 – Cross section of a NbTi poloidal field coil conductor (left) and a Nb_3Sn Central Solenoid conductor (right) [69].

CSJA8 sample

The Central Solenoid JApanese sample #8 (CSJA8) is a Nb_3Sn CICC. The stability tests were performed at B_{dc} = 9 T, and I_{op} = 40 kA. In the following calculation the data used are from the test with number Q011205, where the nominal AC voltage applied to the AC coil is 320 V. In Figure 2.5 the discharge of the capacitor is shown in terms of measured voltage of the AC coil.

Table 2.1 – Average magnetic field pulse amplitude indirectly obtained from the voltage generated by the capacitors bench discharge for the CSJA8 test #Q011205.

	Magnetic field amplitude calculated from the CSJA8 voltage (Figure 2.5)
U_{avg} $[V]$	273
ΔB_a $[T]$	0.78
B_a $[T]$	0.39

The voltage is used to determine the magnetic field amplitude. In Table 2.1, the voltage half amplitude, between the average U_1-U_2 and U_2-U_3, is multiplied for the field-to-voltage ratio. The resulting 0.39 T is the magnetic field amplitude used during the stability simulation.

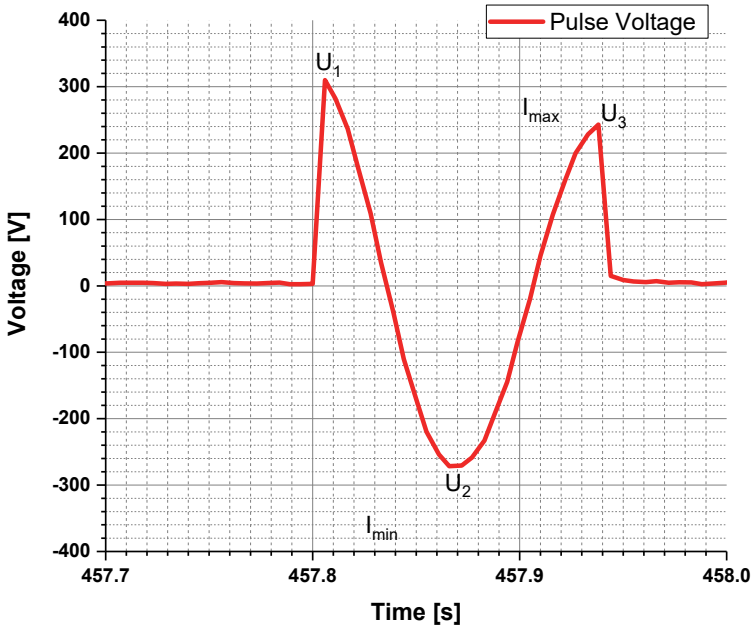

Figure 2.5 – CSJA8 test #Q011205. Measured voltage generated by the discharge of the capacitor connected to the AC coil.

2.3. JackPot AC/DC

2.3.1. Introduction

JackPot AC/DC is a numerical model created and developed in the last decade at the University of Twente [51]. It is an electrical and thermal model that can simulate AC and DC performances of CIC Conductors deriving all the cable properties from the conductor geometry model except the inter-strand contact resistance. The code was initially developed to study the JACKet POTential distribution in ITER SULTAN samples, to explain the effect of non-uniform current distribution introduced by the joints. It was extended during the following years to include the coupling with a variable applied magnetic field and strand self- and mutual inductances [52], [50], and the possibility to model a lap-type joint connecting two

conductors [49]. In the following sections the main features of JackPot relevant for the present research are briefly described.

2.3.2. Cable model

The backbone of JackPot is the accurate modeling of internal geometry of the cable down to strand level. The first step in every simulation is to determine the strand trajectories from which the electromagnetic parameter values are defined. Cable twisting and compaction make it particularly complex to model the conductor. To arrive at an ITER cable like geometry, the cabling routine uses a mapping function that changes the coordinates of strands in sub-cable geometries from circular to a final sub-cable segment shape, also called petal. The steps followed to reach the ITER TF full cable geometry are presented in Figure 2.6.

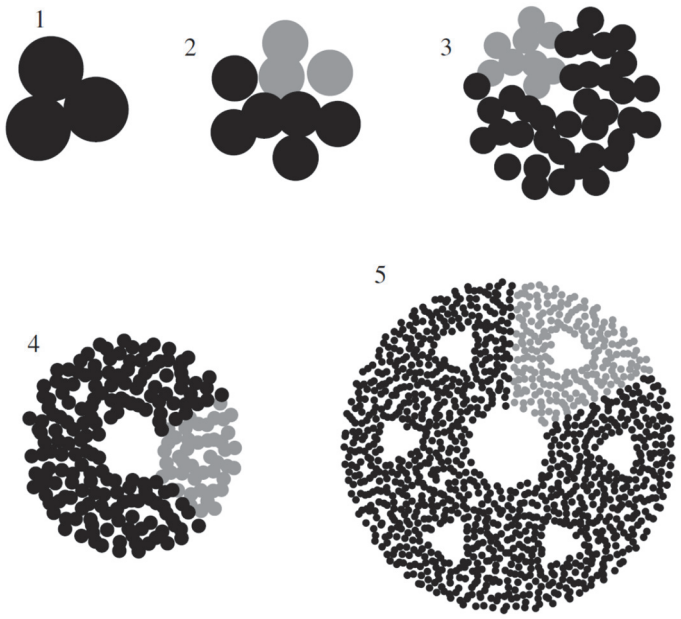

Figure 2.6 – Example of subsequent cabling stages in an ITER TF conductor. In every stage, grey strands represent a sub-cable obtained in the previous step [51].

The three reshaping steps are shown in Figure 2.7. The first step involves the definition of the reshaped cable dimensions: α, r_{in}, r_{out}. The r_{in}, inner radius, is used to account for the inner radius (e.g. central spiral), if present, α is the angle

determined from the number of sub-cables used in the next cabling stage and r_{out} is solved from the requirement that the cable outer diameter has to remain the same during the reshaping. The second step keeps the distance even between surrounding strands and perimeter to reach a close to homogeneous distribution. The last step distributes the strand coordinates around the cable barycenter.

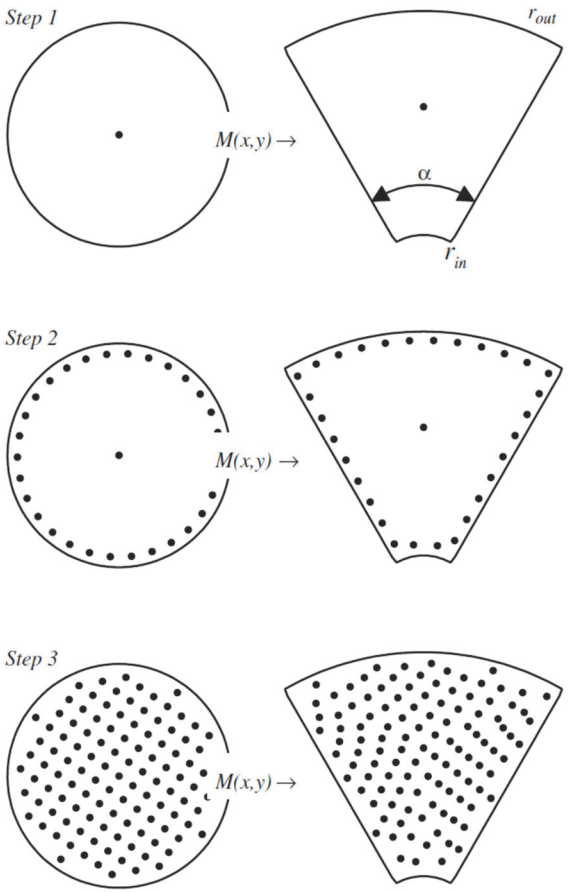

Figure 2.7 – Three steps in the reshaping process of the cabling JackPot modeling, from circular to the final sub-cable shape [51].

The model reproduces the conductor cabling stages, from the triplet (step 1) to the final CICC (step 5). All steps are reshaped following the mapping function explained in Figure 2.7. An occasionally overlap between strands is visible in the geometry. The overlap is used to calculate the inter-strand resistances based on the estimated strand-to-strand contact areas.

2.3.3. Inter-strand contact resistances

JackPot defines the inter-strand contact resistance based on the overlap between strands. The resistance value depends on the inter-strand contact area A_{is}, defined by multiplying the distance d_z between successive strand intersections, and the contact width w_{is}. The length d_z is usually chosen to be 5-10 times smaller than the shortest twist pitch in order to minimize the probability of missing inter-strand contacts. While w_{is} is calculated as:

$$\mathrm{w_{is}} = d_{str}\sqrt{1 - \min\left[1, \left(\frac{d_{is}}{d_{str}}\right)^2\right]}, \tag{2.2}$$

where d_{is} is the distance between the center of the two strands and d_{str} is the strand diameter, see Figure 2.8.

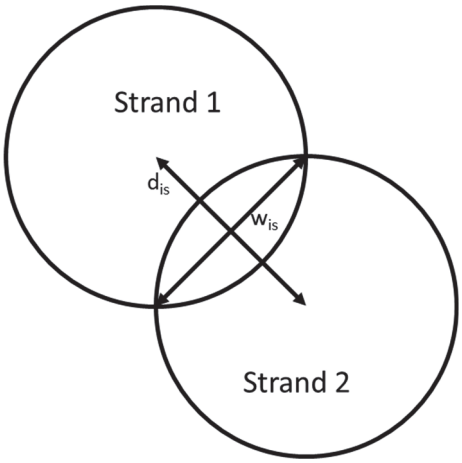

Figure 2.8 – Schematic of the contact resistance calculation, w_{is} is the inter-strand contact width and d_{is} is inter-strand distance between the strand centers [51].

Finally the inter-strand resistance, R_{is}, is calculated as following:

$$R_{is} = \frac{\rho_{is}}{A_{is}}. \tag{2.3}$$

The ρ_{is} is the inter-strand resistivity expressed in [$\mu\Omega \cdot m^2$]. The resistivity per unit of surface is the only free parameter used in the JackPot model and it can be obtained from inter-strand contact resistance measurements, e.g. as performed in the Twente Press experiment [70], [71] or indirectly by fitting the ρ_{is} to the results of a

coupling loss experiment. If petal wraps are present, the inter-petal resistivity can be introduced as a second parameter to take into account the differences in contact resistances. All contact resistances are stored in the conductance matrix of the system.

2.3.4. Self- and mutual inductances

After the calculation of the resistances, the strand trajectories are used for the calculation of the self- and mutual inductances. The self-inductance of a single strand is equal to the sum of mutual inductances between the sections of the strand plus the self-inductances of each section [72]. JackPot considers strands as piecewise linear line elements [52] and therefore the mutual inductance can be expressed as a linear double integral:

$$\mathrm{M_{ij}} = \frac{\mu_0}{4\pi}\left(\vec{u}_i \cdot \vec{u}_j\right) \int_{L_i} \int_{L_j} \frac{1}{\left|\vec{r}_j - \vec{r}_i\right|} dL_j dL_i, \qquad \textbf{(2.4)}$$

with L_i and L_j being the lengths of the strand sections where the current is flowing, $\vec{u}_i$ and $\vec{u}_j$ are unit vectors expressing the direction of sections, $\left|\vec{r}_j - \vec{r}_i\right|$ is the distance between two strands, see Figure 2.9.

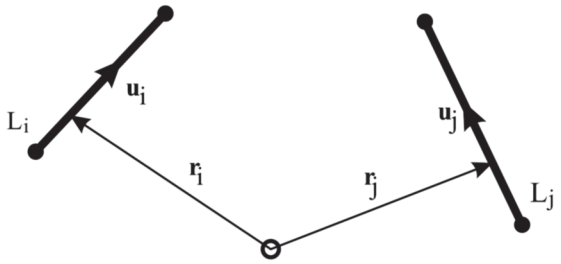

Figure 2.9 – Vector used to calculate the mutual coupling between two strand elements carrying current L_i and L_j [52].

The *j* integral in eq. (2.4) can be solved as:

$$\vec{A}_j(\vec{r}) = \frac{\mu_0 \vec{r}_j}{4\pi} \cdot \int_{L_j} \frac{1}{|\vec{r}|} dL_j, \qquad \textbf{(2.5)}$$

in which $\vec{A}_j$ is the magnetic vector potential normalized to the current in *j* at point $\vec{r}$. Therefore eq. (2.4), can be rewritten as:

$$\mathrm{M_{ij}} = \int_{L_i} \vec{u}_i \cdot \vec{A}_j(\vec{r}_j - \vec{r}_i) dL_i. \tag{2.6}$$

The resulting mutual coupling is numerically solvable. If the distance between the two strand sections (represented by lines) is large enough, then the ratio between their length and distance decreases and eq. (2.6) can be approximated by:

$$\mathrm{M_{ij}} = \left(\vec{u}_i \cdot \vec{A}_j(\vec{r}_j - \vec{r}_{i,c})\right) L_i. \tag{2.7}$$

Or for larger distances even as:

$$\mathrm{M_{ij}} = \left(\vec{u}_i \cdot \vec{A}_j(\vec{r}_{j,c} - \vec{r}_{i,c})\right) L_i, \tag{2.8}$$

where $\vec{r}_{i,c}$ and $\vec{r}_{j,c}$ point to the center of the line section *i* and *j,* respectively. In Jackpot, all three equations are used. Eq. (2.6) and (2.7) are used for strands in the same or adjacent grid segments and eq. (2.8) for strands at larger distances.

2.3.5. Magnetic field coupling

The coupling to an external magnetic field is expressed in terms of magnetic vector potential:

$$\vec{B} = \nabla \times \vec{A}. \tag{2.9}$$

Assuming an external magnetic field of direction –*x*, it can be written as:

$$B_x = \partial_y A_z - \partial_z A_y, \tag{2.10}$$

where A_y can be chosen as the only non-zero component, and eq. (2.10) becomes:

$$A_y = -|B_x| z. \tag{2.11}$$

The vector potential can be written depending on the magnetic field amplitude:

$$\vec{A} = A_y \vec{u}_y = -|B_x| z \vec{u}_y = |B| \vec{A}', \tag{2.12}$$

where $\vec{A}'$ is the vector potential normalized to the magnetic field amplitude.

Faraday's Law:

$$\Delta V = -\frac{d\Phi(\vec{\mathrm{B}})}{dt}, \tag{2.13}$$

shows that electromotive force is induced by the rate of change of the magnetic field flux. Using Stokes' theorem the magnetic field flux can be expressed as:

$$\Phi(\mathrm{B}) = \oint_{L_i} \vec{A} \cdot \vec{L}_i. \tag{2.14}$$

Combining eq. (2.13) and eq. (2.14) with eq. (2.12) and assuming *B* only time dependent and *A* only space dependent leads to:

$$\Delta V = -\frac{d|B|}{dt}\left(\oint_{L_i} \vec{A}' \cdot \vec{L}_i\right). \tag{2.15}$$

The integral is the coupling term with the time-varying external magnetic field.

The self field is calculated using Biot-Savart Law:

$$\vec{B}(\vec{r}) = \frac{\mu_0}{4\pi}\int_{L_i} \frac{Id\vec{L}_i \times \vec{r}}{|\vec{r}|^3}, \tag{2.16}$$

where $\vec{B}$ is the magnetic field calculated at the distance $\vec{r}$, generated by the current *I* that flows in the section L_i in the direction $d\vec{L}_i$.

2.3.6. System of Equations

The JackPot AC/DC equations system is based on Kirchhoff's first and second Laws and is applied using the voltage and currents nodes defined by the geometry.

The system of equation can be summarized as:

$$\begin{cases} G \cdot V^T + G \cdot V^T(B_{ext}) + D_i \cdot I = 0 \\ V^L(B_{ext}) + \Delta V + C_v \cdot V = \dfrac{MdI}{dt} \end{cases}, \tag{2.17}$$

where the terms are:

- $G \cdot V^T$ inter-strand current through the conductance matrix,
- $G \cdot V^T(B_{ext})$ transfer current induced by the external magnetic field,
- $D_i \cdot I$ current balance in axial direction,
- $V^L(B_{ext})$ induced voltage in strand longitudinal direction,
- ΔV voltage drop across the strand,
- $C_v \cdot V$ voltage different across current elements,
- $\frac{MdI}{dt}$ self- and mutual inductances.

2.4. Model with Partial Shielding zone (MPAS)

In a superconducting composite strand, the transverse currents between the filaments generate AC coupling loss. An applied external transverse magnetic changing field with amplitude B_a, creates a reacting field inside the strand of value $\tau(dB_i/dt)$ [41]. In this condition the power loss generated by the transverse currents is deposited inside the strand as volume and can be expressed by the equation:

$$P = \frac{2\tau\left(\frac{dB_{int}}{dt}\right)^2}{\mu_0}. \quad \textbf{(2.18)}$$

The structure of a CICC is significantly different, and very much more complex than of a strand. The use of a global time constant τ to represent the AC coupling loss of a multistage cable can be convenient and accurate for gradual variations of magnetic field (dB/dt), but this approximation fails to describe the behavior for faster field variations [73]. With the same methodology, the coupling loss can be fitted analytically assuming the presence of several time constants associated with respective volume fractions in a CICC, a concept which was proposed in [43] and later also adopted in [74], [75]. The Model with PArtial Shielding zone (MPAS) [76] uses some simplifications by adopting the concept of several stages, each represented by a time constant τ_i, with the idea of modeling the interactions between the stages. Unfortunately, these stages do not necessary reflect the real

contribution which every stage gives to the total coupling loss. The parameters of the MPAS are calculated for a given ITER conductor by fitting the measured AC loss data obtained in SULTAN in a given range of frequency, typically 0.1 to 5 Hz [73]. It is important to note that the parameters obtained from a fit to a coupling loss versus frequency curve, is only valid for the specified experimental conditions of selected frequency range and amplitude of the applied magnetic field. Furthermore, the same coupling loss measurements can be fitted with different sets of constants, which contribute to the unpredictability of the model far from the calibrating conditions.

2.4.1. Coupling loss calculation

MPAS is calibrated by fitting the SULTAN AC loss measurements using a set of multiple time constants τ_i and corresponding volume fractions k_i, in general one for every cabling stage. The coefficient k_i is smaller than 1 and represents partial shielding provided by the current loops generated by the external variable magnetic field. Once the time constants and the volume fractions are defined for a coupling loss versus frequency curve, the calculation of the coupling loss is straightforward. The expression used to calculate the power dissipated in the CICC is derived from eq. (2.18), where $B_{ext}(t) = B_a \sin(\omega t)$ is the sinusoidal applied magnetic field and B_{int} is the magnetic field inside the conductor, expressed as:

$$B_{int} = B_{ext} - \tau \frac{dB_{int}}{dt}, \tag{2.19}$$

which can be re-written as:

$$B_{int} = \frac{B_a}{\sqrt{\omega^2 \tau^2 + 1}} \sin(\omega t - \delta), \tag{2.20}$$

where B_a is the field amplitude, ω the angular frequency, τ the coupling current decaying time constant, $\delta = \arctan(\omega\tau)$.

The power dissipation can be calculated as follows:

$$P(t) = \sum_n \frac{k_n \tau_n \dot{B}^2_{int_n}(t)}{\mu_0}, \tag{2.21}$$

where n is the number of time constants chosen to model the conductor.

Finally the coupling loss $Q_{coupling}$ is found using:

$$Q_{coupling} = \int_{t_{pulse}} P(t)dt, \tag{2.22}$$

where t_{pulse} is one period of the applied sinusoidal magnetic field.

2.4.2. Stability calculation

For the stability test, instead of a continuous sinusoidal pulse, a single sinusoidal magnetic field pulse is applied to the conductor, see Figure 2.3. In terms of power the pulse shape can be expressed as a truncated sinusoid [73]. To model the stability trigger pulse it is necessary to modify eq. (2.20) into:

$$B_{intI} = \frac{B_a}{\sqrt{\omega^2\tau^2+1}}\left[\sin(\delta)\, e^{\left(-\frac{t}{\tau}\right)} + \sin(\omega t - \delta)\right] \quad \text{for } 0 < t < t_0, \tag{2.23}$$

$$B_{intII} = \frac{B_a}{\sqrt{\omega^2\tau^2+1}}\sin(\delta)\left(1 - e^{-\frac{t_0}{\tau}}\right)e^{-\frac{t}{\tau}} \quad \text{for } t > t_0, \tag{2.24}$$

where t_0 is the pulse period. The derivatives of eq. (2.23) and (2.24) are:

$$\dot{B}_{intI} = \left\{\frac{B_a}{\sqrt{\omega^2\tau^2+1}}\left[\omega\cos(\omega t - \delta) - \frac{1}{\tau}\sin(\delta)\, e^{\left(-\frac{t}{\tau}\right)}\right]\right\} \quad \text{for } 0 < t < t_0, \tag{2.25}$$

$$\dot{B}_{intII} = \left\{-\frac{B_a}{\tau}\frac{1}{\sqrt{\omega^2\tau^2+1}}\sin(\delta)\left(1 - e^{-\frac{t_0}{\tau}}\right)e^{-\frac{t}{\tau}}\right\} \quad \text{for } t > t_0. \tag{2.26}$$

The power dissipation can be calculated using eq. (2.25) and eq. (2.26) in eq. (2.21) for the truncated sinusoidal signal. The comparison between a perfect sine wave and the truncated sinusoid generated by the equations above is shown in Figure 2.10.

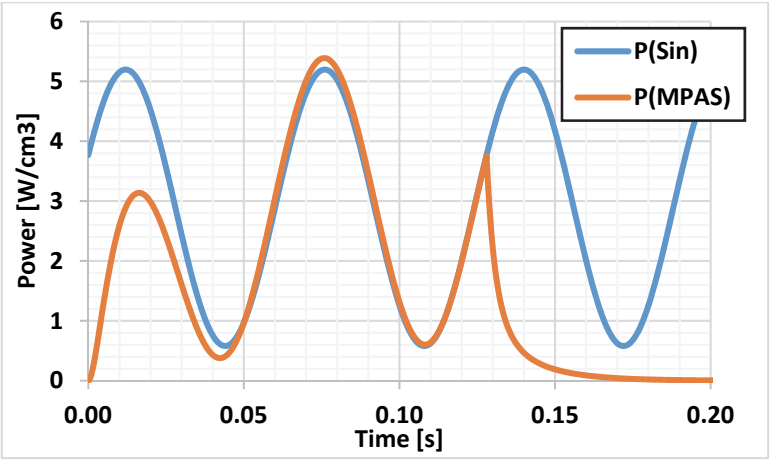

Figure 2.10 – Example of the compared power profiles for the permanent and the truncated sinusoidal power dissipation versus time corresponding to MPAS (t_0 = 128 ms, B_a = 0.2 T).

2.5. THEA

The THEA (Thermal, Hydraulic and Electric Analysis of Superconducting Cables) [77], [57] code is a 1-D model, used to analyze the thermal and hydraulic behavior of a cable in conduit superconductor. The model is divided in three sets of domains. The first domain, the conductor, is defined by using a set of thermal components as superconducting and copper strands and jacket. The second domain, representing the hydraulic components, is defined by the coolant parameters, like helium mass-flow, cross-sectional area of the bundle A, wetted perimeter W_p, and void fraction. The third domain, the electric components, is based on the current carrying elements for which the transport current behavior is described. The three domains are related through material properties and the relations between the state variables.

2.5.1. Cable model and SULTAN sample

The CICC is simplified to two thermal elements. The first element is the superconductor and copper composite modeled like a single component instead of hundreds of strands. The second element is the stainless-steel jacket. The superconductor and the copper, which acts as resistive stabilizer, see section 1.4.1, are assumed to be electrically and thermally in parallel. The jacket and the

superconducting component are not electrically connected. The hydraulic part concerns the supercritical helium, flowing in the bundle and in the channel. The hydraulic and thermal components are thermally connected through the contact surface, called wetted perimeter.

The NbTi and Nb_3Sn conductors are modeled here reproducing the SULTAN short sample design. The considered conductor length is 1.5 m, the current and the applied magnetic field are considered constant. The coupling loss dissipation is calculated using MPAS or JackPot and directly injected in the cable model as heat deposition. The heat is deposited only in the superconductor and copper composite. The heating zone is 0.39 m long representing the SULTAN AC coil length. The helium in the central channel is not taken into account because in the SULTAN sample the channel is closed to force the coolant to flow only in the voids of the bundle. However, few simulations including the central channel were performed to study its influence on the stability during fast and slow heat depositions.

2.6. Structure of the modeling

In this study, the THEA code is used in combination with MPAS or JackPot, to model the thermal behavior of CICCs for stability analysis for the first time. The aim is to evaluate the agreement between electromagnetic and thermal simulations and the recent stability experiments performed in SULTAN.

In Figure 2.11 the content of the study is shown schematically. MPAS and JackPot-AC/DC, both in combination with THEA, are compared for the analysis of the NbTi and Nb_3Sn conductors. JackPot-AC/DC is able to simulate the behavior of a conductor for every coil operating scenario since it has incorporated a very detailed description of the conductor geometry, transport and coupling currents in all strands. This way it is able to handle all transport current, self-field and applied field variations in time and extrapolative predictions are well possible. For the analytical MPAS, the modeling options are more constrained since the approach is based on sinusoidal applied magnetic fields without transport current and the wire bundles are represented by a selected number of single coupling loss time constants. In the following chapters, it is shown that by using the combination THEA and JackPot AC/DC it is very well possible to perform a complete characterization of the thermal and electromagnetic behavior of a CICC during fast magnetic field transients. Then it can be applied to predict the CIC Conductor performance when exposed to the ITER plasma operating scenario.

2.6. Structure of the modeling

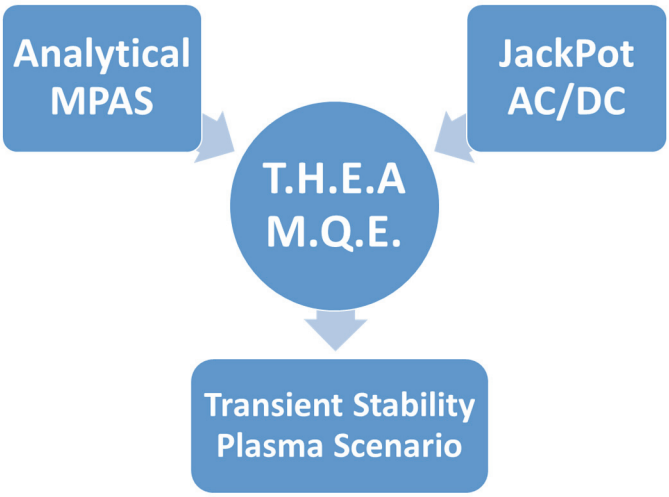

Figure 2.11 – Overall scheme of the present study. Both, MPAS and JackPot-AC/DC are used in combination with THEA to model the SULTAN stability tests in order to extrapolate towards the ITER Plasma Scenario performance.

3. MODELING STABILITY OF POLOIDAL FIELD COIL CONDUCTOR

3.1. Introduction

The MPAS-THEA models combination is used to analyze the stability experiments performed on ITER Poloidal field coil conductors and the results are compared to JackPot. The aim is to investigate and predict the operational temperature margin for various disturbance profiles relevant for the ITER plasma operating scenario.

The conductor is the one used for ITER Poloidal Field coils 1 and 6 made only of NbTi strands. The absence of segregated copper in this conductor simplifies the cable model. The SULTAN measurements on sample PFEU2 (Poloidal Field coil European Union sample number 2) [67] are used to calibrate and validate the codes. In this study the THEA code (CryoSoft, Horizon Technologies [57]) is used in combination with MPAS [76] to model the thermal behavior of the PFEU2 sample during Minimum Energy Quench (MQE) tests. The MQE tests are performed using a truncated single sine wave magnetic field pulse. The fast magnetic field variations generate current loops and heat dissipation, which cause a quench when exceeding a critical level of energy.

After validation of the models, the impact of the central channel and the effect of the jacket on the temperature detection for the calorimetric measurements are investigated for a sinewave magnetic field pulse.

3.2. PFEU2: conductor layout and parameters

The SULTAN PFEU2 sample is made from one conductor unit length bent into a U-shape [60]. The cable comprises of only superconducting strands, cabled in five twisting stages around a stainless steel spiral. Every petal is wrapped with partial coverage using a stainless steel foil to increase the inter-petal contact resistances and leave space for helium exchange between the petals. Finally the cable is inserted in a stainless steel 316L circular-hole-in-square jacket, see Figure 3.1 for cable and strand cross sections. The main parameters of the CICC are listed in Table 3.1 [66], [78].

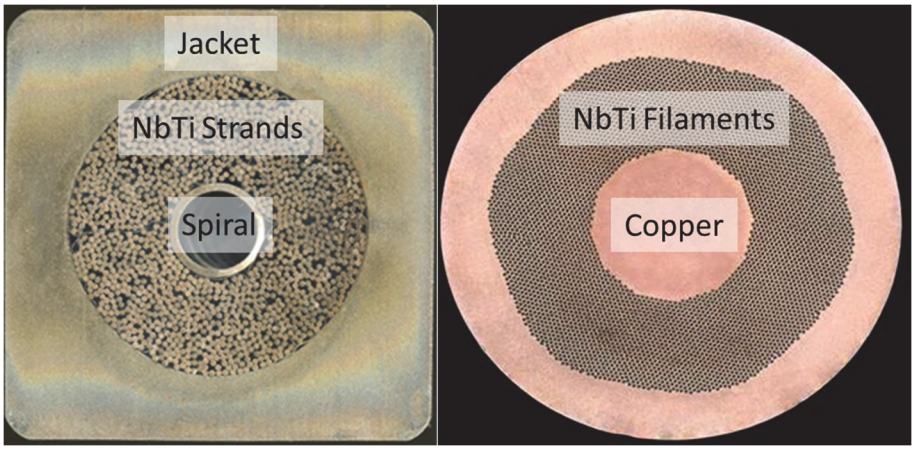

Figure 3.1 – Cross section of a PF1-6 conductor (left) and of a NbTi strand (right) [79].

Table 3.1 – Parameters of the ITER poloidal field coil conductor PFEU2.

	PFUE2
Shape	Circle-in-Square
Main outer dimension [mm]	53.8 x 53.8
Target jacket inner diameter [mm]	37.7
Target central spiral diameter [mm]	10-12
Cable layout	3Sc x 4 x 4 x 5 x 6
Jacket material	Stainless steel - 316L
Void fraction [%]	34.3
Joint layout	Hairpin
Strand manufacturer	Chepetsk Mechanical Plant (ChMP)
Strand Cu:nonCu ratio	1.59
RRR	>100
Petal wrap coverage [%]	50
Cable wrap overlap [%]	40
Number of Sc. strands	1440

The I_c and the T_{cs} of the sample are expressed by the parametrization of the function $J_c(B,T)$. The NbTi strand parameters used to model the critical current as function of temperature and magnetic field of the PFEU2 sample following eq. (1.1) are listed in Table 3.2 [79].

Table 3.2 – NbTi strand parameters for $J_c(B,T)$ characterization.

	PFEU2
C_1 [A/m^2]	$7.02 \cdot 10^{11}$
C_2 [A/m^2]	$7.36 \cdot 10^{10}$
B_{c20m} [T]	14.26
T_{c0} [K]	9.02
α_1	2.97
β_1	2.18
γ_1	2.91
α_2	0.56
β_2	1.78
γ_2	1.77

3.3. Stability tests

The MQE test data performed at the SULTAN facility, serve as input to study the stability of ITER conductors under various operating conditions. The tests are carried out in the presence of a magnetic background field and stationary current. The energy in the conductor is injected by applying a fast singular sinusoidal magnetic field pulse using the AC coil thereby inducing eddy and coupling current losses in the sample. The amplitude of the applied sinusoidal single pulse is progressively increased stepwise until a quench occurs. The MQE assessment procedure is detailed in [66]. The energy deposited is determined by the temperature difference measured between the temperature sensors upstream and downstream the High Field Zone (HFZ), see section 2.2.1, based on the mass-flow rate and the helium specific heat [80], see eq. (3.1):

$$Q \propto C_p \dot{m} \int \Delta T dt. \tag{3.1}$$

Only one leg of the sample is considered for analysis because the quench is generated only in one leg. Both legs are not perfectly identical. The differences generated during the production process cause one leg to quench before the other. The measured data of the test with number #Q010709 is shown in Figure 3.2 with the blue line representing the downstream-upstream temperature difference. The difference is integrated, using eq. (3.1), over the time interval between the magnetic field pulse (black line) and when ΔT has returned to zero. The error bar

involved in the energy extrapolation are considered 10%, due to the oscillation in the helium temperature and the fast magnetic field sinewave applied. The higher the initial temperature of the helium, the more unstable the temperature measurements are. The error in the temperature difference is minimized by subtracting the shift in temperature oscillation between upstream and downstream sensors in relation to the helium velocity, see appendix A for the detailed procedure.

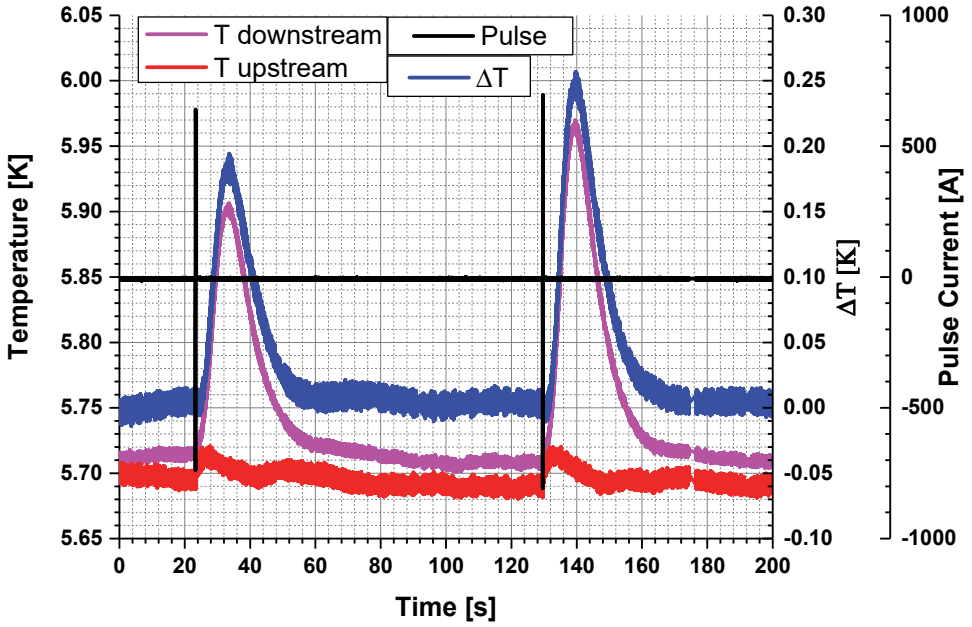

Figure 3.2 – Temperature versus time in PFEU2 sample, test run #Q010709. Red and pink lines are the temperatures measured upstream and downstream, blue line is the temperature difference and black line is the current of the AC coil to generate the magnetic field pulse.

A characteristic result of a global MQE test series is shown in Figure 3.3. The energy per unit of volume deposited during the fast singular pulsed field transition is represented as a function of the pulsed field peak value. The energy that initiates a quench is not directly measurable, because the self-heating generated during the quench increasing dramatically the temperature and obscures completely the heat deposition due to the magnetic field pulse. Therefore, the quench energy (yellow mark) is extrapolated by a linear fit from the previous values of energy with lower magnetic field pulse amplitude. The figure shows the impact of the operating

temperature on the MQE at a transport current of 44 kA. The effective global MQE is between the yellow mark and the last no-quenching point. The higher the operating temperature, the lower is the required deposited energy and consequently the magnitude of the magnetic field pulse necessary to initiate a quench. The boundary conditions applied to the PFEU2 sample during the stability test are listed in Table 3.3.

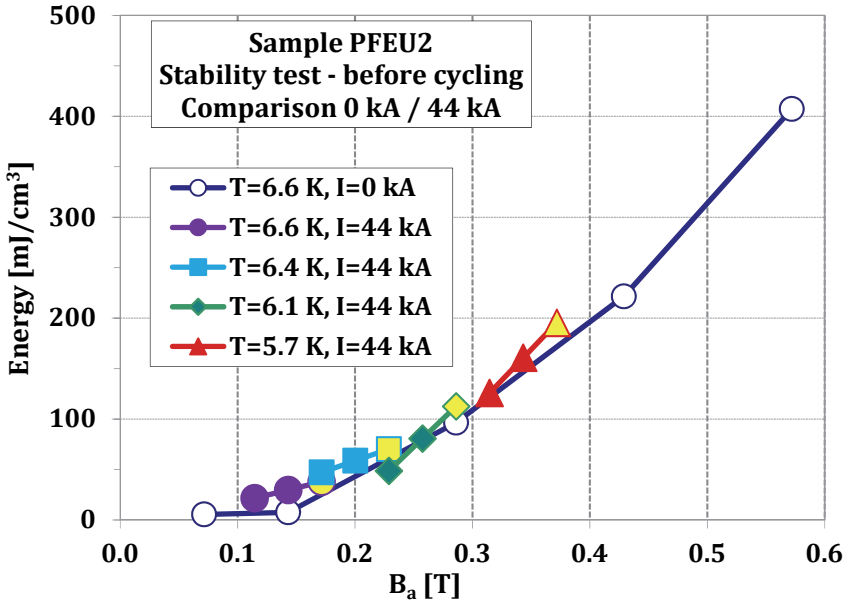

Figure 3.3 – Measured global MQE of the PFEU2 sample before the EM cyclic loading. The value B_a is the peak magnetic field applied to the conductor during the stability test. The yellow symbol is the estimated energy that initiates a quench in the conductor at each testing temperature.

Table 3.3 – Stability test boundary conditions for the PFEU2 sample.

	PFEU2
Peak magnetic field [T]	5.20
Background magnetic field [T]	4.52
Test current [kA]	44
Temperature range [K]	5.7 - 6.6
Pulse duration [ms]	128

3.4. Simulation using MPAS-THEA code

3.4.1. MPAS calibration

The MPAS simulation is calibrated by fitting the SULTAN AC loss measurement data using a set of multiple time constants τ_n and volume fractions k_n, one combination of τ and k for every cabling stage, as presented in eq. (2.21) [76]. They are listed in Table 3.4. The typical error of the fit is 5%. In Figure 3.4 the MPAS fit is compared to the measured coupling loss after subtraction of the hysteresis loss. The contribution of every stage in the total coupling loss as it is modeled in MPAS is also shown in the plot.

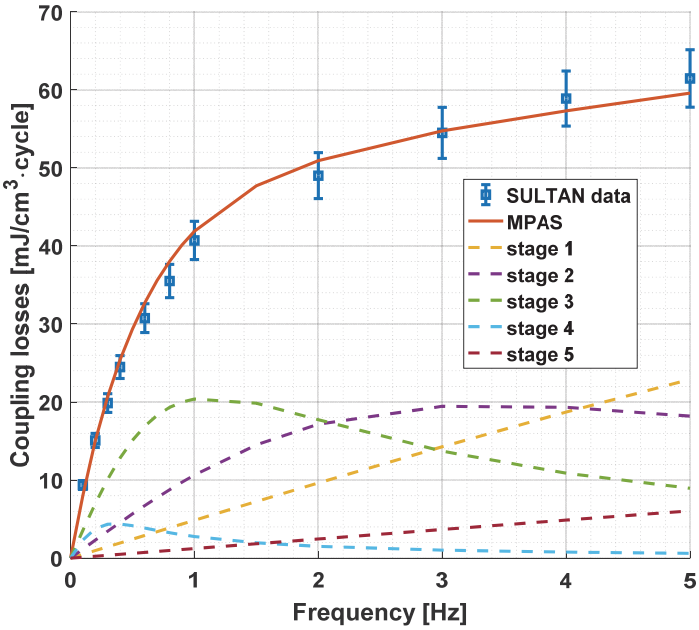

Figure 3.4 – MPAS fit of the PFEU2 coupling loss in virgin condition at B_{dc} = 4.52 T and I_{op} = 44 kA. Dots represent the SULTAN measured coupling loss, the solid line the MPAS fit, dashed lines are the separate stage contributions.

Table 3.4 – τ and k coefficients of the PFEU2 sample in virgin condition at B_{dc} = 4.5 T and I_{op} = 44 kA [79].

stage	***1***	***2***	***3***	***4***	***5***
τ_n *[ms]*	7.9	47.0	139.0	45.0	4.0
K_n	1.00	0.40	0.42	0.09	0.50

3.4.2. MPAS-THEA stability simulations

The MPAS is calibrated by fitting the SULTAN coupling loss measurements that are different in terms of temperature and magnetic field peak value from those used during the MQE stability tests. The difference can have impact on the power calculation since using different applied magnetic field pulse peak value assumes the prospective of scalability for MPAS. Meanwhile, the temperature affects the critical current possibly creating saturation of coupling current loops and different shielding effects for the involved time constants and volume fractions. Therefore, using the MPAS model to simulate the coupling loss in conditions far from the calibration conditions leads to unpredictable errors.

In Figure 3.5 the energy calculated with MPAS using the SULTAN MQE magnetic field peak value B_a, is compared to the MQE extrapolated from the stability tests.

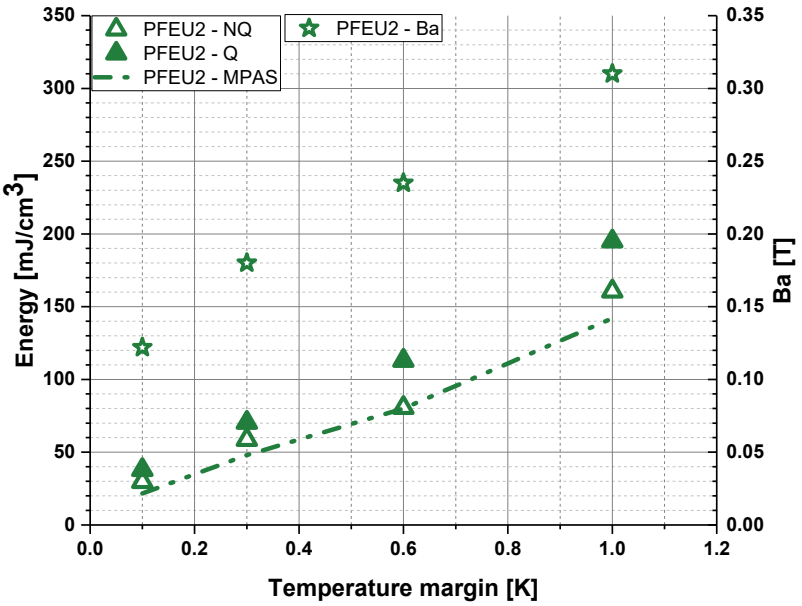

Figure 3.5 – On the left y-axis, measured and calculated energy of the sample PFEU2 as function of the temperature margin. Open dots represent recovery while full dots indicate quench. The dashed line is the energy calculated using MPAS. On the right y-axis, the magnetic field peak value used to achieve the quench versus temperature margin. The background field is 4.52 T and the transport current is 44 kA.

In all following figures, recovery is represented by open dots, while filled dots indicate a quench of the sample and the actual MQE is between these limits. The dashed line is the energy calculated by MPAS applying the magnetic field peak value B_a used during the stability test to generate the open dots, which is scaled on the right axis. The temperature margin is the difference between the T_{cs} and the operating temperature.

The results of the PFEU2 sample show a good match between MPAS simulation and experiment. The discrepancy at 1 K in temperature margin is probably related to the magnetic field peak value, about 0.31 T. As expected, the difference in applied magnetic field peak value and temperature generates is MPAS analytical model a discrepancy in the calculated energy. This type of behavior was already observed in [73].

The following THEA computations are based on the PFEU2 sample configuration. The conductor is modeled using two components: thermal and hydraulic. The superconducting strands and jacket represent the thermal elements while the coolant parameters, like helium mass-flow, cross-sectional area of the bundle, wetted perimeter and void fraction are the hydraulic elements. The parameters are summarized in Table 3.5 [68].

Table 3.5 – Sample PFEU2 hydraulic and thermal parameters as used for THEA.

	PFUE2
Hydraulic	
A_{Helium} $[mm^2]$	344
Wetted perimeter bundle [mm]	3667
Wetted perimeter jacket [mm]	118
Void fraction [%]	34.3
Mass flow [g/s]	2.5
Thermal	
$Area_{NbTi}$ $[mm^2]$	229
$Area_{Cu}$ $[mm^2]$	366
$Area_{bundle}$ $[mm^2]$	595
$Area_{jacket}$ $[mm^2]$	1432

An example of the THEA output based on the MPAS calculated results as input is shown in Figure 3.6. The generated heat deposition in the PFEU2 conductor during

a stability test is modeled by the truncated sinusoidal magnetic field pulse of 128 ms duration.

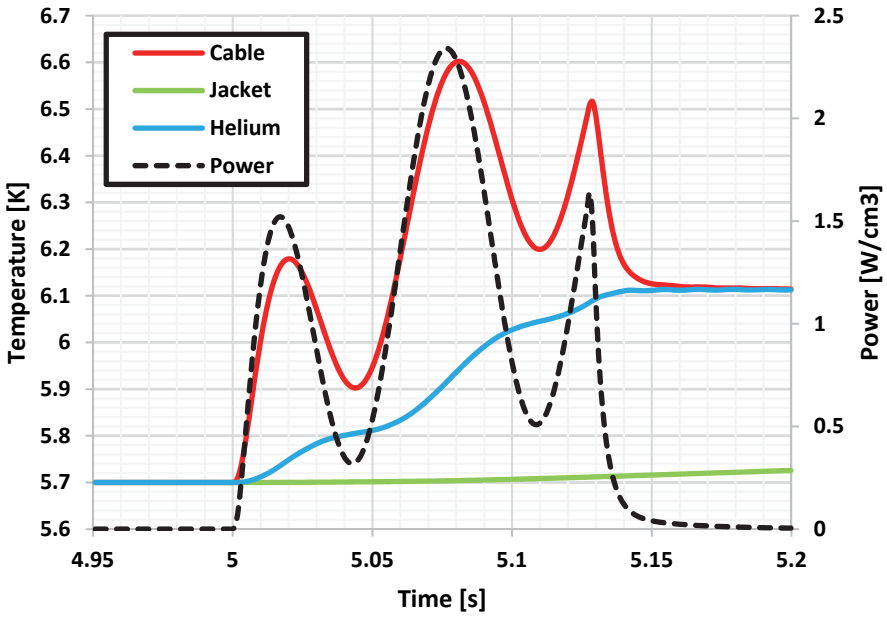

Figure 3.6 – On the left y-axis, the characteristic temperature variation of the PFEU2 components as function of the simulation time. On the right y-axis, the injected power deposition as function of the time simulated with the THEA code. The injected power (black line) is based on the truncated sinusoidal magnetic field pulse. The background field is 4.52 T and the transport current is 44 kA.

The increase of the cable temperature is faster than the helium heat removal, therefore the cable is able to reach and exceed the T_{cs}, even if the helium temperature is still lower. In the example, the cable reaches 6.6 K, while the helium is still at 6.0 K. The wetted perimeter and the helium heat transfer dominate the heat exchange between conductor and helium as computed by THEA.

In order to understand the effect of the applied perturbation profile on the MQE a second set of simulations is performed. Instead of using a sinusoidal profile in the MPAS-THEA model, the energy is injected using a constant heat deposition in time. The comparison between both power deposition profiles with same total energy is shown in Figure 3.7.

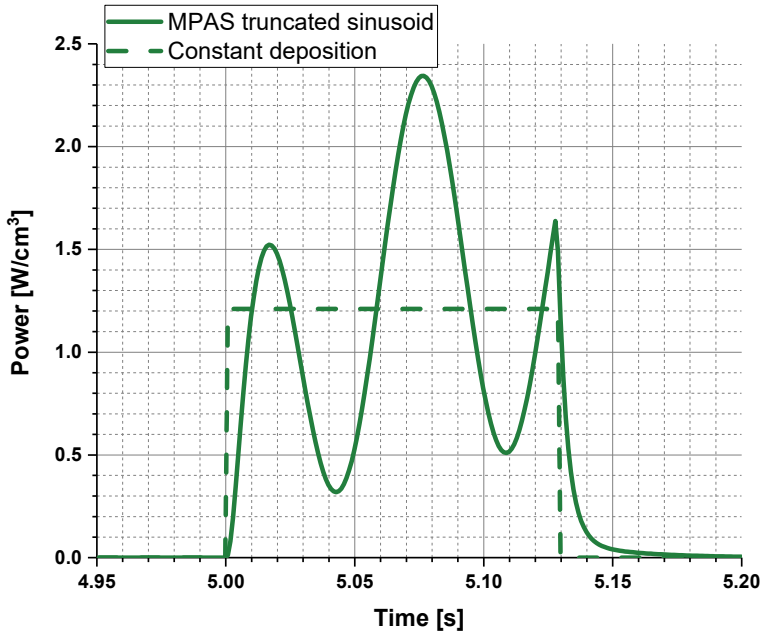

Figure 3.7 – Power deposition as function of time. The power per unit of composite volume, injected using the MPAS truncated sinusoid, is compared with an equivalent power injected with a constant deposition pulse.

In Figure 3.8, the MQE simulations for the PFEU2 using the two power deposition profiles are compared to the MQE measured data. All results in the figure are with the conductor conditions as listed in Table 3.3. The lines represent the MQEs calculated with MPAS-THEA from the truncated sinusoidal (solid) and constant deposition (dashed), while the markers are the data of the measured SULTAN tests. Constant energy deposition and MPAS profile have both 128 ms pulse duration. The simulations are performed increasing gradually the peak magnetic field, i.e. the energy injected in the conductor, until a quench occurs.

According to the results shown in Figure 3.8, it is predicted that the constant deposition case requires a higher level of MQE. By changing the profile of the heat deposition, the MQE is modified by about 20%. This means that the MPAS-THEA simulations are as accurate as the used analytical expression of the perturbation in the conductor. To arrive at correct representation of the MQE, it is evidently necessary to accurately evaluate the perturbation profile and it is not sufficient to use a pulse with constant power and the same energy.

The THEA model with MPAS input shows good agreement with the SULTAN MQE tests results even if it is a simplification of the real CICC layout. The simulated MQE is between the no-quench and quench measured limits.

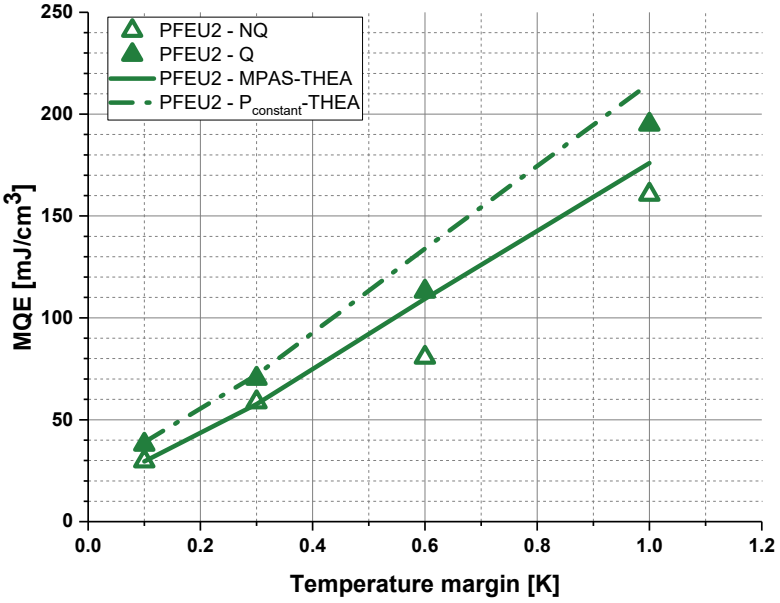

Figure 3.8 – MQE of the PFEU2 sample as a function of the temperature margin. The lines represent the MQEs calculated with MPAS-THEA from the truncated sinusoidal (solid line) and constant (dashed line) energy deposition. The markers are the experimental data of the SULTAN tests. Open dots indicate recovery, full dots represent a quench.

Following the temperature evolution of conductor and coolant it is possible to determine the start of the quench, see Figure 3.9. The energy is injected in the conductor using the truncated sinusoidal pulse and the maximum power is reached in the central peak (see Figure 3.7), which corresponds in this case to the maximum cable temperature. The temperature profile shows that the central peak indeed triggers the quench. It also appears that if the conductor remains superconducting when passing the central peak, the power deposition due to the third peak is not able to trigger a quench.

When a NbTi conductor exceeds the T_{cs} by a few mK, part of the NbTi changes from superconducting to normal state and the helium is not capable to recover superconductivity. Accordingly, as a result of an avalanche like process, the whole cable quenches. This sharp transition can be explained by the definition of the

current sharing temperature (T_{cs}) and the steepness of the transition from superconductive to normal state [55].

The T_{cs} is the temperature associated with a defined critical electric field E_c of $10\ \mu V/m$ [81]. The local electric field is expressed as:

$$E = E_c \left(\frac{I_{strand}}{I_c}\right)^n, \tag{3.2}$$

where I_c is the critical current, I_{strand} is the current flowing in the strand and n defines the steepness of the transition [82], which is assumed about 30 for ITER NbTi CICCs. The high value of n causes NbTi to have a sharp transition causing an irreversible runaway and to be unable to recover even from slightly exceeding the T_{cs}.

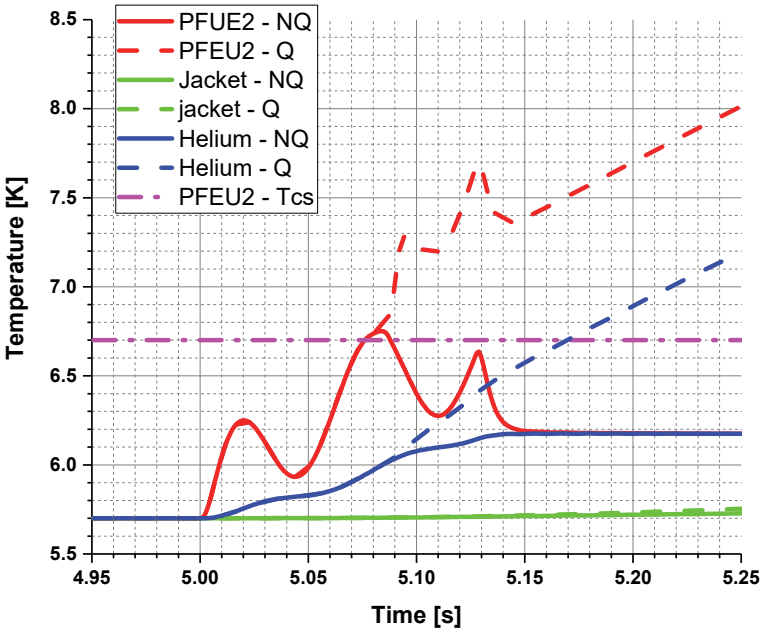

Figure 3.9 – Sample PFEU2 temperature versus time calculated by MPAS-THEA, the solid lines represent the temperature fluctuation during the MQE simulation for the cable and the helium, while the dashed lines represent the temperature evolution during a quench. The horizontal dashed line represents the measured T_{cs} of the PFEU2 cable.

3.4.3. Effect of the jacket on calorimetric measurements

As explained in section 2.2.1, the temperature sensors attached to the conductor jacket are four upstream and four downstream the HFZ, see Figure 2.1. The energy deposited in the conductor is calculated using the temperature difference between the average of downstream and average of upstream sensors. The temperature increase of the jacket is affected by the helium heat transfer and depends on the jacket wetted perimeter. Due to the complex cable structure, the percentage of jacket perimeter in direct contact with the helium is difficult to assess. By varying the wetting perimeter percentage in contact to the helium, the output temperature, calculated with MPAS-THEA, is compared with the temperature measured in SULTAN, see Figure 3.10.

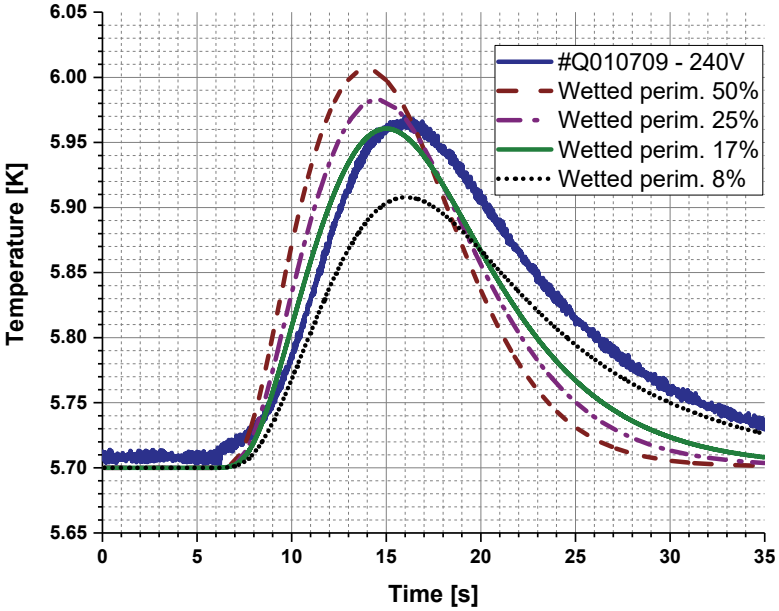

Figure 3.10 – Jacket temperature variation as function of time for different wetted perimeters. Solid blue line is the temperature measured during the PFEU2#Q010709 test run, the others lines are the MPAS-THEA temperature simulations for different percentage of the jacked wetting perimeter.

The blue line represents the measured data, while the others lines are the results of the MPAS-THEA simulations. The reference test run is PFEU2#Q010709 at 1 K temperature margin, chosen because of the well-defined temperature profile. The magnetic field pulse peak value used to generate the heat deposition is 0.31 T. The

best fit between measured and modeled temperature profiles is obtained for about 17% of total wetted perimeter.

The simulated peak temperature of the jacket decreases with the wetted perimeter, while the jacket cool down increases. However, the difference, between the integrals of the simulated curves, is less than 2% as long as the wetted perimeter is larger than 17%. For these cases the amount of helium in direct contact with the jacket will not affect the energy calculation but only the curvature of the measured temperature profile. For a wetted perimeter less than 17% (green dots in Figure 3.10), the discrepancy increases and the time integral of the jacket temperature does not reflect well the real energy injected in the conductor. In all studies presented in this chapter, the wet perimeter percentage in contact with the helium is considered to be between 17 and 20%, which corresponds to about 23.6 mm.

3.4.4. Effect of the central channel on short pulse MQE

The central channel of the conductor in the SULTAN sample is closed to force the helium to flow only the voids of the bundle. Therefore, it is not necessary to include the central channel in the model for SULTAN sample analysis. However, it is interesting to investigate the effect the channel has on the conductor stability. The channel is modeled as a second hydraulic component linked to the helium of the bundle using the parameters reported in [5].

The MQE calculated in the presence of a central channel is practically similar to that without a central channel. This is probably related to the short heat deposition time of 128 ms. For such a short pulse, the MQE is not dominated by the quantity of the coolant but by the wetted perimeter of the strands. The additional amount of helium in the central channel does not cause and increase of the MQE.

Although the channel does not influence the MQE, it has an important effect on the quench propagation velocity. The quench propagation for the two different configurations is calculated simulating a quench just above the MQE level defined in Figure 3.8. The quench is generated by applying a magnetic field pulse with B_a = 0.35 T over a length of 0.39 m.

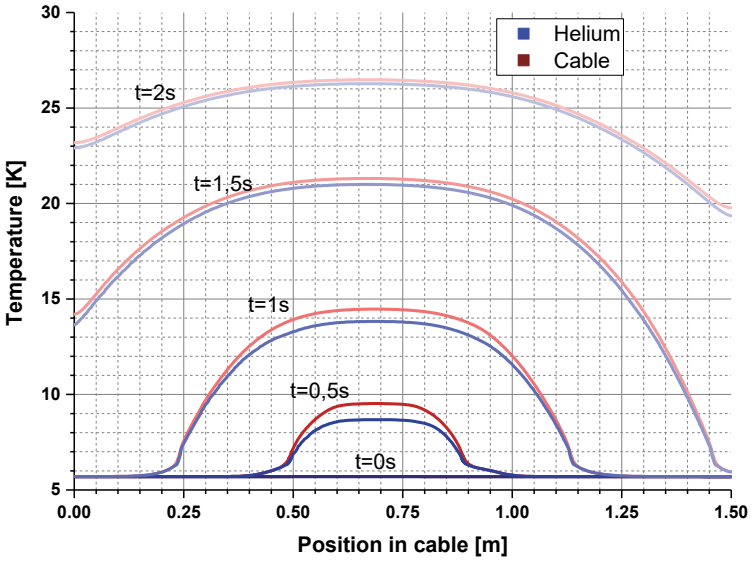

Figure 3.11 – Temperature profile of the quench propagation of the PFEU2 sample as function of the position in the cable and time, without the central channel. At t = 0 s the magnetic field pulse with peak value B_a = 0.35 T is applied.

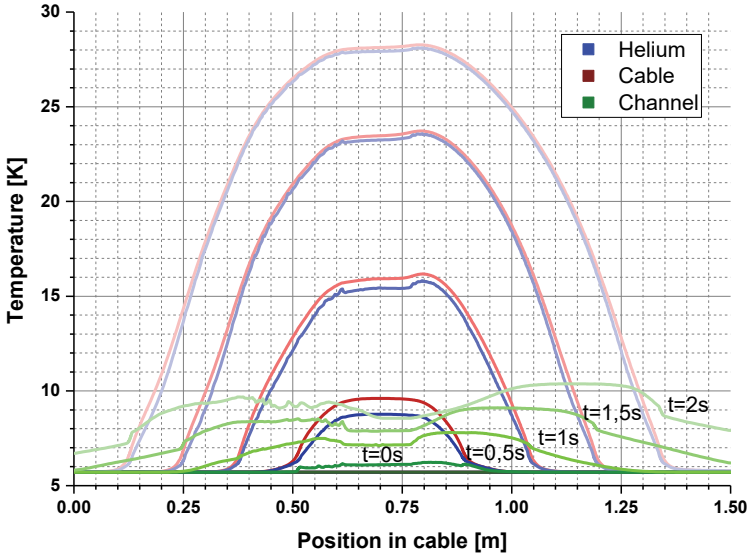

Figure 3.12 – Temperature profile of the quench propagation of the PFEU2 sample as function of the position in the cable and time, with central channel. At t = 0 s the magnetic field pulse with peak value B_a = 0.35 T is applied.

The quench propagation along the cable is shown in Figure 3.11 and Figure 3.12, without and with central channel, respectively. At t = 0 s the magnetic field pulse is started. In the following 2 s the temperatures of cable and helium reach more than 25 K in the center of the sample where the pulse is applied. The presence of more helium does not allow recovering the conductor once it has crossed the T_{cs}. In Figure 3.11 the sample of 1.5 m length without the central channel is entirely above 20 K in less than 2 s while in Figure 3.12 it is shown how the presence of the channel slows down the quench propagation. With the central channel, the helium temperature is above T_{cs} after 2 s, but in the bundle the cable is still in superconductive state at both ends of the sample.

3.5. Simulation using JackPot AC/DC

3.5.1. JackPot calibration

With JackPot-AC/DC a full CIC Conductor is simulated using a network model of superconducting and resistive elements describing the trajectories of all the strands inside the cable without any free parameters in the model except one: the value of the inter-strand contact resistance. This is calibrated using the SULTAN coupling loss results. The parameters, used for the conductor and the strands scaling law, are the same as used for the MPAS-THEA model listed in Table 3.1 and Table 3.2. During the SULTAN tests, the combination of magnetic field and transport current causes Lorentz forces in the conductor that influence the inter-strand and inter-petal resistivities. JackPot is able to account for the mechanical effect of the Lorentz forces on the cable's contact resistance by fitting the coupling loss measured in SULTAN.

The hysteretic loss from the SULTAN results is subtracted from the total AC loss as a constant value independent of frequency in order to compare only the coupling loss contribution. Figure 3.13 shows the measured and calculated coupling losses of the PFEU2 sample.

The resistivity parameters obtained from the fit are used for the MQE simulations since AC loss and MQE experiments have similar test conditions regarding background field and transport current.

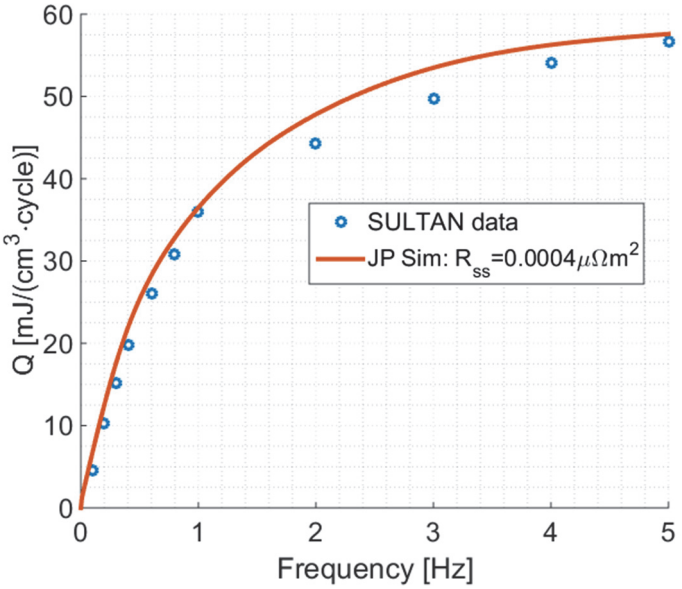

Figure 3.13 – Measured and calculated coupling losses versus frequency of the PFEU2 sample before cycling, at B_{dc} = 5.2 T and I_{op} = 44 kA with B_a = 0.2 T. Dots represent measured SULTAN data, while the line is the JackPot simulation.

3.5.2. JackPot simulations

After the calibration of the inter-strand contact resistance, the MQE tests can be simulated with JackPot. The output power calculated by JackPot is compared to the measured data and the analytical results calculated by the MPAS model. The temperature, background magnetic field and transport current are set to the same values as used for MPAS, see Table 3.3. The JackPot sinusoidal magnetic field pulse has the same peak value as the pulsed field used in the SULTAN stability experiment.

The power deposited versus time computed with JackPot is compared to the MPAS calculated profile in Figure 3.14. Although there is a difference between both model results, the profile generated with the simple MPAS analytical model resembles quite well the results of the more detailed JackPot approach.

The JackPot routines are not extended for simulation of the thermal quench initiation and propagation like in THEA. Therefore, it does not deliver the immediate value of MQE. However, JackPot is able to calculate precisely the momentary power

generated during a magnetic field pulse of any shape in time and the linked complex current distribution inside the cable. This makes JackPot a valuable tool for computation of the power dissipation in the conductors during plasma operating conditions and sudden plasma current disruptions.

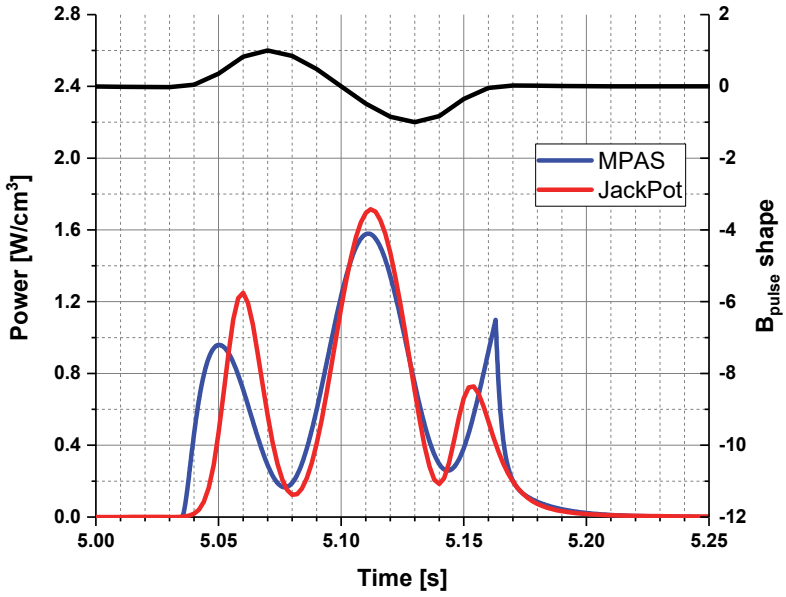

Figure 3.14 – Example of deposited power per unit of composite versus time. The red line is the power simulated by JackPot, while the blue line is the power calculated by MPAS. The black trace is the magnetic field pulse.

As for MPAS, the coupling current loss induced from the pulsed magnetic field inside the conductor computed by JackPot are compared with the energy deposited during the experiment in Figure 3.15. This illustrates that the discrepancy between the measured and simulated MQE is less than about 10% for the PFEU2 sample. The energy measured in SULTAN is well in agreement with the energy calculated by JackPot. The agreement between JackPot and MPAS for this particular sample is remarkably good, with only few mJ/cm^3 of difference between the two curves.

Finding the MQE by JackPot combined with THEA is far more time demanding than using the straightforward analytical MPAS-THEA method because it is necessary to run a JackPot simulation for every magnetic field pulse and every temperature margin. After already finding the good agreement between the PFEU2 measured

results and the MPAS-THEA analysis it is more interesting to invest calculation-time into the quench analyses of the Nb_3Sn conductors in the following sections.

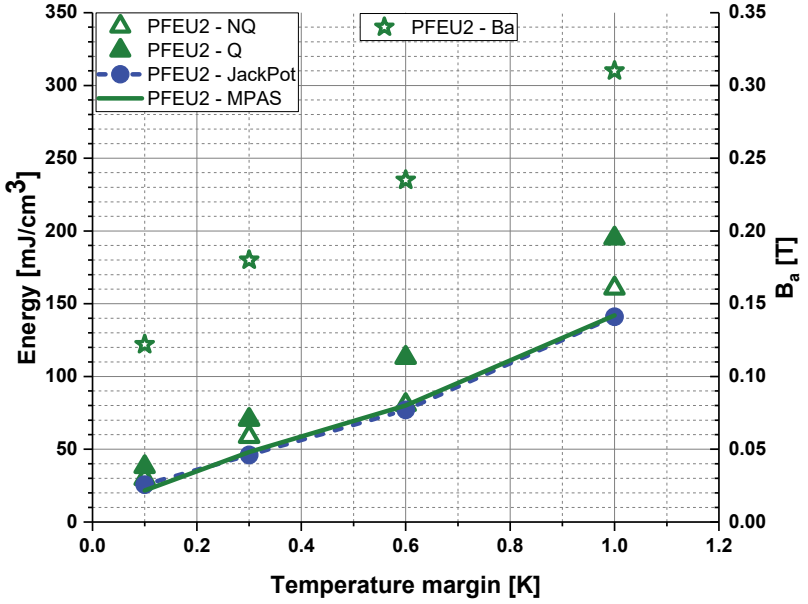

Figure 3.15 – Left axis: energy as function of the temperature margin of the PFEU2 conductor computed by JackPot and MPAS. The markers represent the experimental data from the SULTAN test (open dots indicate recovery, full dots quench) and the dashed line is the MPAS MQE simulation. The blue line with the dots represent the JackPot results for the SULTAN test in recovery conditions. Right axis: the experimental magnetic field pulse amplitude versus temperature margin used for the simulation.

3.6. Conclusion

Coupling loss power simulations using the dedicated analytical model MPAS and the network model JackPot were calibrated for the ITER PFEU2 NbTi sample, showing both good agreement with the measured SULTAN coupling loss data. The stability measurements performed at the SULTAN facility are reproduced using both MPAS and JackPot, and the simulations are maximum 10% different from the experimental data.

Using the analytical MPAS-THEA combination, the minimum quench energy (MQE) threshold is defined for the NbTi PF1 conductor. The discrepancy between measured and predicted MQE is less than about 10%.

The profile of the deposited power with time has a significant effect on the calculated MQE results. For a constant deposition the quench energy is increased by about 20% compared to a truncated sinusoidal magnetic field pulse.

The deposited power profile, analytically calculated with MPAS, is close to the JackPot simulated profile, showing a good comprehension of the power deposition mechanism in both models.

The helium flow blockage of the central channel in SULTAN samples does not significantly influence the quench threshold for short magnetic field pulses of 128 ms. However during these fast perturbations the presence of a central channel causes a small reduction of the quench normal zone propagation velocity.

4. MODELING TRANSIENT STABILITY OF THE CENTRAL SOLENOID CONDUCTOR

4.1. Introduction

The conductors in the ITER magnet system are subjected to fast changes of current and magnetic field during the plasma-operating scenario. Most critical concerning the level of magnetic field rates is the Central Solenoid (CS), capable of reaching over 13 T with a maximum rate of 1.5 T/s after the Start of Discharge. This extreme condition is not easily reproducible in existing experimental conductor test facilities. The only experimental data available for quantitative analysis were produced at the ITER Central Solenoid Model Coil (Naka, Japan) and at the SULTAN conductor test facility. However, conductor layout, time and magnetic field settings are quite different from the ITER operating conditions [83]. Particularly for the latter one, the test conditions for initiating a quench do not cover the ITER operating conditions. Nevertheless, the test results are very useful for calibrating the simulation codes as used in the analysis presented here.

After calibrating the MPAS code with the CSJA8 conductor AC loss test results, the MPAS-THEA [76], [77] analysis of the sample stability shows the limitations of the MPAS model for Nb_3Sn conductors. To achieve accurate transient stability predictions and to study the behavior at strand level for Cable-in-Conduit Conductors, it is necessary for a code to calculate AC loss with high accuracy and to manage variations in strand current, magnetic field and temperature. JackPot AC/DC [51], [52], [84] is a suitable code for the calculation of local ohmic loss since it is able to generate the internal geometry of a real CIC Conductor with strand level precision and to simulate the electromagnetic behavior of a conductor during stability tests and a Plasma Scenario (PS). The THEA code [77] is used to add a thermal routine to JackPot. The resulting combination of codes, in this study called JackPot-THEA, is able to predict the stability limit of a cable, starting only from conditions of current, temperature and magnetic field. The stability results for short magnetic field pulse, simulated with MPAS-THEA and JackPot-THEA, are compared to evaluate the effectiveness of the two models.

The purpose of the analysis presented here is to better understand the stability behavior of the CS conductor under realistic operating conditions. Starting with the results based on SULTAN short sample stability test results with very short pulse

duration (t_{pulse} = 128 ms) for further verification of the models for Nb_3Sn conductors. The simulation proceeds towards analysis of different perturbation times with longer pulse duration for extrapolation to Plasma Operating conditions for ITER CS conductors. The most severe condition for the CS coils during the 15 MA Plasma Scenario is during the plasma initiation for about 1 to 2 s [17], while the SULTAN singular sine wave pulse period is only 0.128 s. Although with cautiousness, the stability results obtained from the analysis of the SULTAN tests are used for extrapolation with JackPot-THEA and investigating the MQE for more relevant magnetic field disturbances by taking 1 and 5 s single sinusoidal pulses.

4.2. Minimum Quench Energy of the CSJA8 conductor

The SULTAN Nb_3Sn sample is inserted in a magnet system able to generate orthogonally oriented DC and AC magnetic fields. The stability tests are carried out in the presence of transport current and background magnetic field. A single fast sinusoidal field pulse generates the loss in the conductor using the AC coil. The pulse amplitude is increased stepwise until a quench occurs. The conductor sample used for this study is the CSJA8, of which the conductor parameters are listed in Table 4.1.

Table 4.1 – Parameters of the ITER Central Solenoid conductor CSJA8 [85].

	CSJA8
Shape	Circle-in-Square
Main outer dimension [mm]	49 x 49
Target jacket inner diameter [mm]	32.6
Target central spiral diameter [mm]	7 x 9
Cable layout	(2Sc+1Cu) x 3 x4 x 4 x 6
Jacket material	JK2L
Void fraction [%]	33.5
Joint layout	Praying hand
Strand manufacturer	KAT
Strand Cu:nonCu ratio	1
RRR	>100
Petal wrap coverage [%]	70
Cable wrap overlap [%]	40
Number of Sc. strands	576

The strand critical current is modeled using the ITER scaling law for Nb_3Sn wire [86]. Figure 4.1 shows an example of the ITER Central Solenoid conductor and KAT Nb_3Sn strand cross sections.

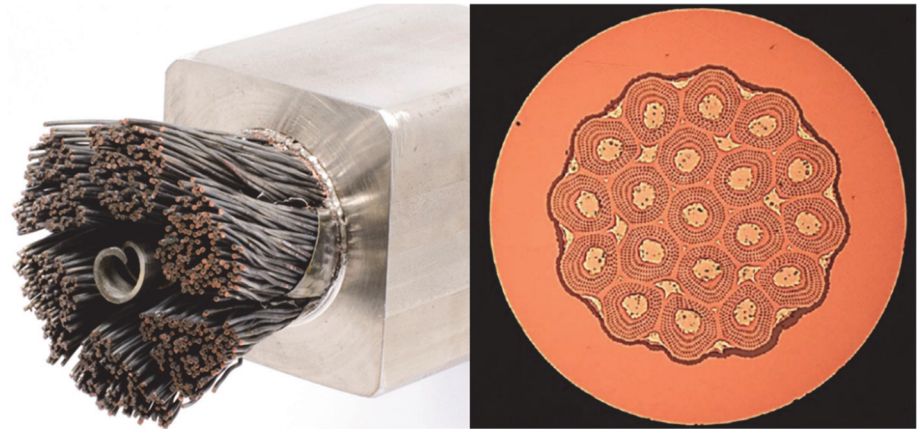

Figure 4.1 – On the left, cross section of a Nb_3Sn ITER Central Solenoid conductor [69]. On the right, cross section of the internal tin route Nb_3Sn strand for the ITER Central Solenoid conductor developed by KAT [87].

The critical current of the KAT strand [87] is modeled using eq. (1.5). The scaling law parameters were measured at the University of Twente and are summarized in Table 4.2 [88]. The only unknown free parameter to model the strand critical current of the sample is the axial strain applied to the Nb_3Sn filaments caused by the cooling down and the electromagnetic charging process. The measured current sharing temperature, T_{cs}, is used to determine the lacking applied strain parameter. The T_{cs} is defined as the temperature where the electric field reaches $E_c = 10\ \mu V/m$ [81]. Knowing the measured T_{cs} and the test conditions in terms of current and applied magnetic field, the Nb_3Sn scaling law can be used to calculate the effective strain. The electromagnetic forces applied on the conductor influence the effective strain. Therefore, the T_{cs} test conditions play an important role in the effective strain. In SULTAN, just before the beginning of the stability test, a measurement of the T_{cs} is performed using the same test conditions applied during the test. This T_{cs} measurement allows to calculate the exact effective strain necessary to model the MQE tests, in this case ε_{eff} = - 0.54%.

The test conditions used for the stability simulations are summarized in Table 4.3. In the following paragraphs the simulation results for 0.128, 1 and 5 s single

sinusoidal magnetic field pulse periods is analyzed and compared to the SULTAN MQE results. The sinewave is chosen in order to minimize the difference between the model and the SULTAN fast pulse experiment and to clarify the influence of the pulse period and magnetic field peak value. Magnetic field variations relevant for Plasma Operating conditions can be applied later on. The 5 s period analysis is also used to investigate the impact of the central channel on the conductor's stability.

Table 4.2 – KAT Nb_3Sn strand scaling law parameters for $J_c(B,T,\varepsilon)$ characterization [87].

	KAT strand
C_{a1}	45.33
C_{a2}	0.0
ε_{0a}	0.325%
ε_m	-0.164%
$B_{c2m(0)}$	29.26
T_{cm}	16.17
C	12499
p	0.419
q	1.431

Table 4.3 – Test conditions for the stability tests performed on conductor sample CSJA8.

	CSJA8
Background magnetic field [T]	9
Test current [kA]	40
Temperature range [K]	7.7 – 8.6
Sinusoidal pulse periods [s]	0.128, 1 and 5

A typical chart of an MQE test is shown in Figure 4.2. The energy deposited through the AC field per unit of volume is shown as a function of the pulse field peak value B_a. As explained previously, because of the self-heating generated by the normal zone avalanche-like process, the actual quench energy (full dots) can only be extrapolated from the energy generated from smaller pulses. The extrapolation is performed using a linear fit, because there are only few measured energies for each temperature margin, usually two, therefore it is not possible to define a better fit.

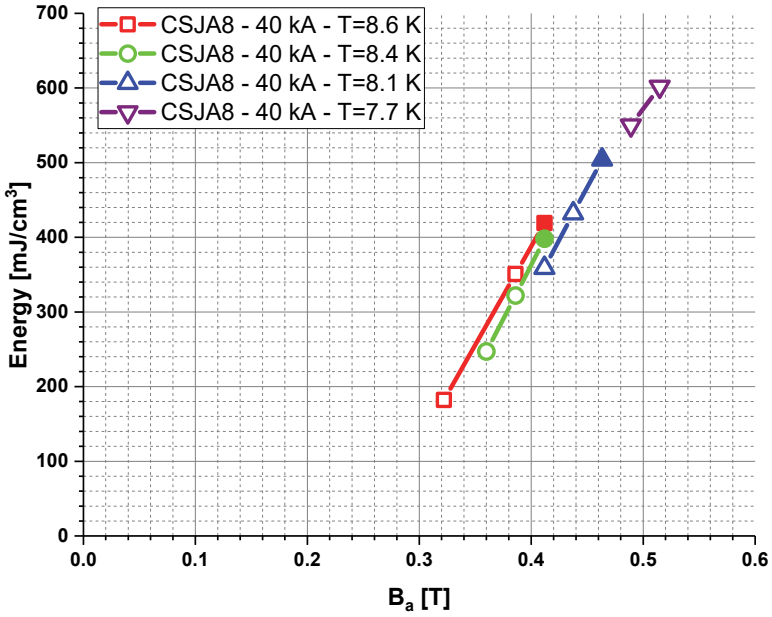

Figure 4.2 – Energy as function of the applied magnetic field pulse peak value, B_a, during the stability test of the CSJA8 sample performed in SULTAN. The open symbols represent recovery, while the filled symbols are the energy levels where the cable is quenching. The test is performed at B_{dc} = 9 T and I_{op} = 40 kA with t_{pulse} = 0.128 s.

The figure shows the impact of the operating temperature on the MQE at a transport current of 40 kA. The MQE is located between the last recovery and the quench energy. Obviously, the higher the operating temperature, the lower is the deposited energy necessary to initiate a quench, and consequently the lower is the magnitude of the magnetic field pulse. The quench energy calculated at T = 8.6 K, is higher than the one at T = 8.4 K. This is due to the linear extrapolation of the quench energy. Since the last recovery point of the 8.6 K curve is higher than at 8.4 K, consequently, the quench is higher. Even though for both energy pulses the same peak magnetic field was used. As said, the actual MQE is between the recovery and the quench points, in addition considering a 10% error in the measurement (section 2.2.2), it is not possible to define if the exact MQE at 8.6 K is higher than at 8.4 K. Only the modeling can show and explain the behavior of the MQE approaching the T_{cs}.

4.3. MPAS-THEA

4.3.1. MPAS calibration

The MPAS model is calibrated by fitting the SULTAN AC loss measurement results using a set of multiple time constants τ_n and corresponding volume fractions k_n, one combination of τ and k for every cabling stage, as explained in section 2.4.1. The k_n and τ_n values are listed in Table 4.4 and shown in Figure 4.3 where the MPAS fit is compared to the measured coupling loss, after subtraction of the hysteresis loss. The plot also shows the contribution of every combination of τ and k for every cabling stage in the total coupling loss as modeled with MPAS.

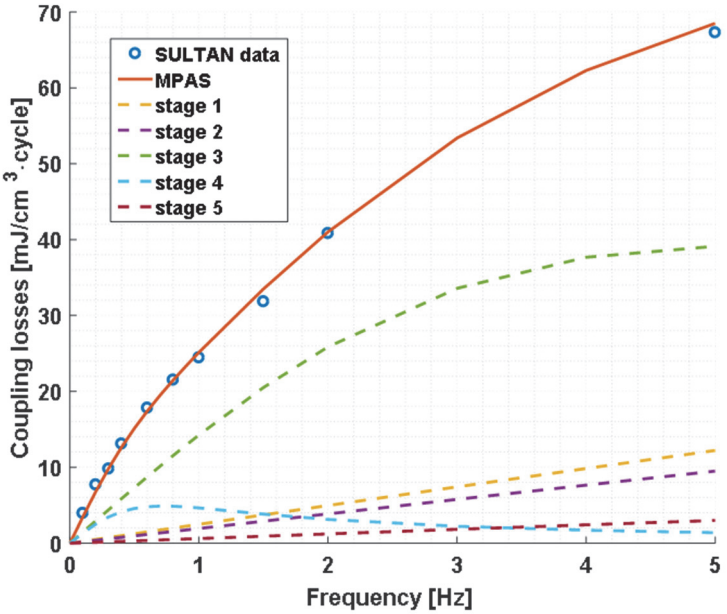

Figure 4.3 – Coupling loss versus frequency of the CSJA8 sample measured, after cycling, in the SULTAN facility and calculated using MPAS. The solid line represents the total MPAS coupling loss, the dashed lines are the separate stage contributions. The test is performed at B_{dc} = 9 T and I_{op} = 40 kA.

Table 4.4 – τ and *k* coefficients of the CSJA8 sample after cycling at B_{dc} = 9 T and I_{op} = 40 kA [89].

Stage	***1***	***2***	***3***	***4***	***5***
τ_n *[ms]*	4.5	4.5	30	220	5
k_n	0.9	0.7	0.8	0.1	0.2

4.3.2. MPAS-THEA stability simulation

The MPAS model is calibrated by fitting SULTAN coupling loss measurements that are different in terms of temperature and magnetic field pulse amplitude from those used during the MQE stability tests. These differences compared to the experimental calibration conditions of MPAS can have impact on the accuracy of the power calculation, as explained in section 3.4.2.

In Figure 4.4, the deposited energy calculated by MPAS using the SULTAN MQE magnetic field amplitude, B_a, is compared to the energy measured during the stability tests. The actual MQE is always between the recovery (open) and the quench (full) markers. The dashed lines are the deposited energies calculated using MPAS. The magnetic field peak value B_a used during the stability test to generate the open dots is used in MPAS to calculated the conductor loss and it is scaled on the right axis.

In Figure 4.4, a peculiar behavior is visible between 0.1 and 0.3 K of temperature margin. The energy deposited in the conductor is higher at 0.1 K than at 0.3 K, during both tests at 40 and 45 kA. The phenomenon was already observed in Figure 4.2, which considers the test at 40 kA. In addition, in the case at 45 kA transport current, the magnetic field pulse applied at 0.1 K is higher than at 0.3 K, 0.37 and 0.36 T, respectively. Using the MPAS model the relation between peak magnetic field, temperature and energy dissipated in the conductor is not straightforward. Therefore is not possible to provide a clear explanation for the phenomena. A realistic explanation can only be given after the analysis performed with JackPot, later in this chapter.

The MPAS calculated deposited energy is significantly below the measured values, about 100 to 200 mJ/cm^3 (∼35%) lower than the measured SULTAN deposited energy. In section 3.4.1, MPAS was able to reproduce correctly the energy deposited in the NbTi conductor. Since, the experimental setup and the test conditions are unchanged, excluding temperature and background field. The discrepancy between the stability tests and MPAS results is likely due to the fact that extrapolative scaling by the MPAS analytical expressions leads to an unpredictable error. MPAS does not consider the impact of the temperature nor the strand saturation in the conductor coupling loss calculation. Thus, the discrepancy is most likely imputable to the MPAS model.

The energy simulated for the Nb_3Sn sample by the MPAS analytical equation is scaled by a correction factor in order to match the measured energy values. The

correction factor depends on magnetic field, and it is a constant value empirically determined in order to match the measured energy to the energy calculated by MPAS. The scaled value is then used in THEA to model the power dissipation in time with the truncated sinusoidal profile. These results are indicated in the following as MPAS*.

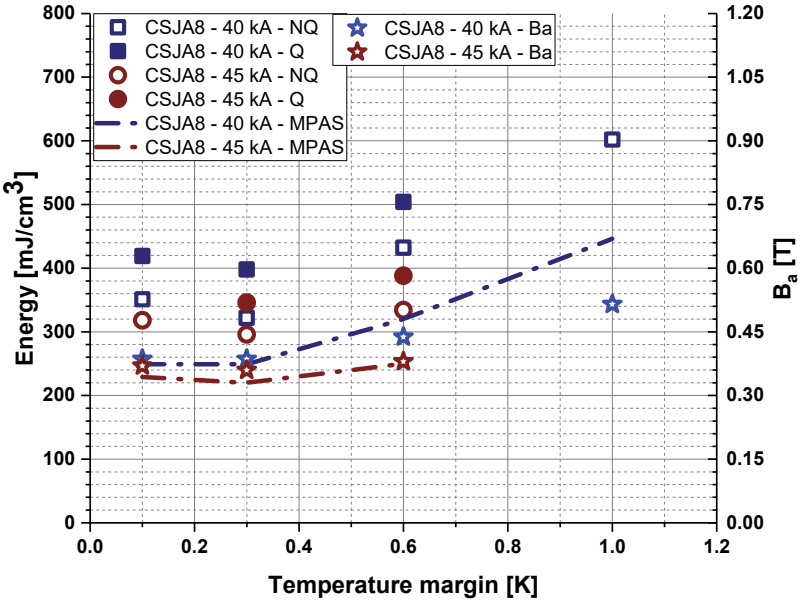

Figure 4.4 – On the left axis, the coupling loss versus temperature margin of the CSJA8 sample measured during the SULTAN stability tests and calculated using MPAS, open markers represent recovery while full markers indicate the occurrence of a quench. On the right axis, the magnetic field amplitude B_a as function of temperature margin used during the stability test. The test conditions are t_{pulse} = 0.128 s, B_{dc} = 9 T and I_{op} = 40 and 45 kA.

The THEA model computations are based on the CSJA8 sample configuration. The conductor is modeled using thermal and hydraulic components. The superconducting strands and jacket represent the thermal elements while the coolant parameters, like helium mass-flow, cross-sectional area of the bundle, wetted perimeter and void fraction are the hydraulic elements. The parameters are summarized in Table 4.5 [68].

In Figure 4.5 the MQE calculated using the MPAS-THEA simulations for the CSJA8 sample at different temperature margins and tweaked for the quantitative energy output are compared to the measured stability tests results. All results in the plot

were obtained with the conductor test conditions listed in Table 4.5. The solid lines represent the MQEs calculated with MPAS*-THEA while the markers indicate the experimental data measured in the SULTAN tests.

Table 4.5 – CSJA8 conductor hydraulic and thermal parameters used in the THEA model.

	CSJA8
Hydraulic	
$Area_{Helium}$ $[mm^2]$	259
Wetted perimeter bundle [mm]	2558
Wetted perimeter jacket [mm]	103
Void fraction [%]	33.6
Mass flow [g/s]	3.3
Thermal	
$Area_{Nb3Sn}$ $[mm^2]$	161
$Area_{Cu}$ $[mm^2]$	321
$Area_{bundle}$ $[mm^2]$	482
$Area_{jacket}$ $[mm^2]$	1566

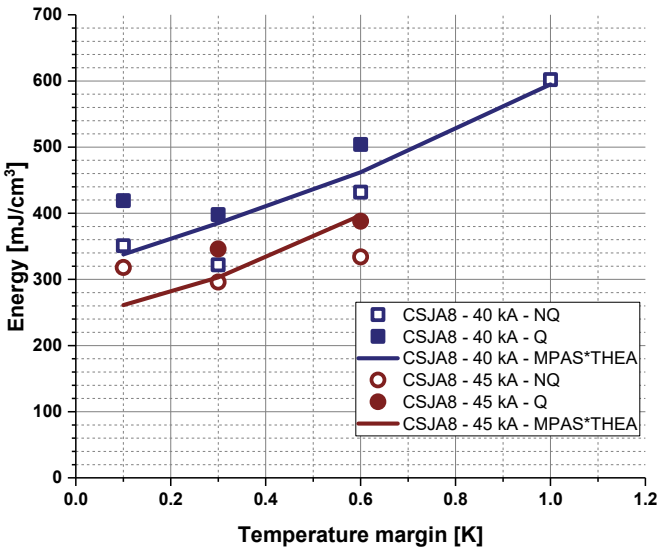

Figure 4.5 – Energy as function of temperature margin of CSJA8 conductor. The lines represent the MQE calculated with MPAS*-THEA, the dots are the experimental data of the SULTAN tests. The applied magnetic field pulse period is t = 0.128 s. Open markers indicate recovery, full markers represent a quench. The test conditions are B_{dc} = 9 T and I_{op} = 40 kA.

The THEA model with MPAS* input (MPAS adjusted for Nb_3Sn), even if it is a simplification of the real CIC Conductor layout, shows good agreement with the SULTAN MQE tests. The simulated MQE is mostly in between the no-quench and quench measured limits. The MPAS* results are not consistent with the data at 0.1 K but the lack of information on the peak magnetic field, due to the correction factor, does not allow to explain the reasons for the discrepancy. However, the different trend of the MPAS*-THEA results, compared to the measured data, suggests a possible larger error in the energy measurements at such small temperature margin.

Following the temperature evolution of conductor and coolant it is possible to determine the start of the quench, see Figure 4.6.

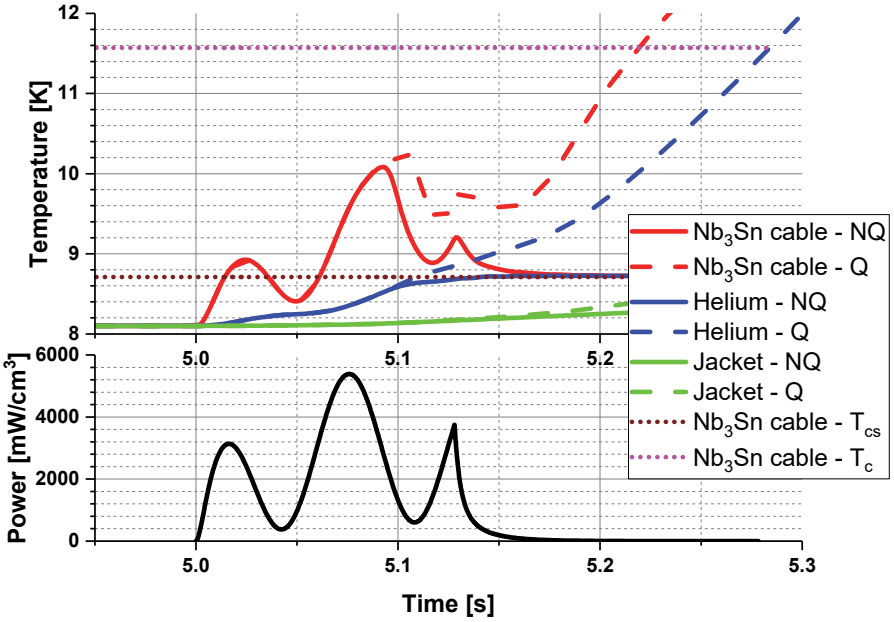

Figure 4.6 – Top: cable, jacket and helium temperature versus time calculated by MPAS*-THEA. The solid lines represent the temperature fluctuation in the case of recovery, while the dashed lines represent the temperature evolution during a quench. The horizontal dashed lines represent the measured T_{cs} and the calculated T_c of the CSJA8 cable. The test conditions are B_{dc} = 9 T and I_{op} = 40 kA. On bottom: power as function of time calculated with MPAS* and used in the THEA simulation.

The energy is injected in the conductor using the truncated sinusoidal pulse and the maximum power is reached in the central peak, which corresponds in this case to the maximum cable temperature. The result shows that the central peak

temperature, which is the most severe, triggers the quench. It also appears that if the conductor is able to survive the central peak, the power deposition from the third peak is not able to trigger a quench.

The Nb_3Sn conductor is still able to recover far above its T_{cs} (~8.7 K) [90], even reaching 10.1 K before initiating a quench. This behavior is different from the NbTi conductor (see section 3.4.2), where the conductor quenches just above the T_{cs}. The difference between the two types of conductors can be explained by the definition of the current sharing temperature (see section 1.4) and the steepness of the transition from superconducting to normal state [55]. The *n*-value defines the steepness of the transition, which is about 30 for NbTi and from 5 to 10 for the ITER Nb_3Sn CIC Conductors. The smaller value of n allows Nb_3Sn to have a much smoother transition and to recover even from temperatures locally exceeding significantly T_{cs}. An opposite result was found when comparing NbTi and Nb_3Sn wires, where a NbTi wire was able to recover even after crossing T_{cs}, while a Nb_3Sn wire was not [91]. The Nb_3Sn behavior was explained by the low conductivity of the bronze matrix but probably also the different *n*-value, compared to the CSJA8 strands, can be important.

4.4. JackPot-THEA

4.4.1. JackPot calibration by AC loss

In JackPot-AC/DC, the CIC Conductor is modeled as a network of superconducting and resistive elements describing the trajectories of all strands. The parameters used for the conductor and the strand scaling law are the same as used for the MPAS-THEA model listed in Table 1.4 and in Table 4.2. JackPot accounts for the mechanical effect of the Lorentz force on the cable by fitting the contact resistivity values used in the simulations to the CSJA8 AC loss measurements with and without transport current [52].

Figure 4.7 shows the measured and calculated eddy current and coupling lossed of the CSJA8 conductor sample. The resistivity parameters obtained from the fit were used for the MQE simulations since AC loss and MQE experiments have similar test conditions regarding background magnetic field and transport current. The simulated cable length corresponds to the effective length of the AC magnetic field, the region were most of the coupling loss is generated and the interaction with the

sample joint is neglected, while the second leg is considered incrementing the magnetic field, see Table 4.3.

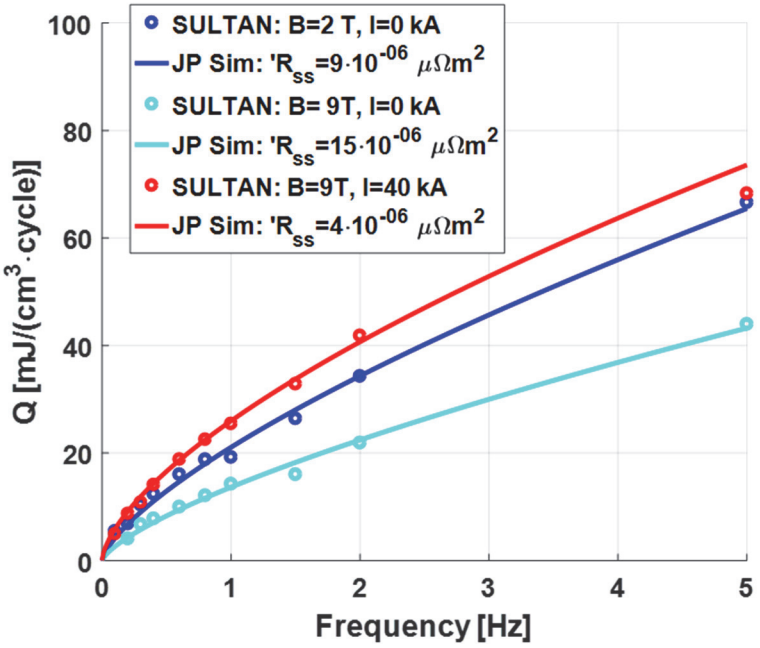

Figure 4.7 – Coupling and eddy current losses versus frequency of the CSJA8 sample. The markers represent SULTAN measurements while the lines represent JackPot (JP) simulations. The test conditions are B_{dc} = 9 T and I_{op} = 40 kA.

4.4.2. JackPot-THEA simulations

After the calibration of the inter-strand contact resistance, the MQE tests can be simulated by the JackPot-THEA combination. The output power calculated by JackPot is used as input in THEA, instead of using the analytical MPAS equation. Temperature, background magnetic field and transport current are set in JackPot as indicated in Table 4.3. The sinusoidal magnetic field pulse used in JackPot has the same peak value and shape as the pulsed field used in the SULTAN stability experiment.

By increasing the initial temperature of the simulation and approaching the current sharing temperature (T_{cs}), the strand can saturate. The strand I_c saturation is taken into account for computation of the coupling loss at high temperature and magnetic field. The current distribution among the strands including the transport

and coupling currents in the whole cable is considered for all strands. JackPot calculates the longitudinal electric field inside the strands using eq. (3.2). The electric field is calculated along all strands of the cable with sufficient discretization in length direction. The saturation is implicitly taken into account since reaching the superconducting transition for a part of the strands (and particular sections of strands depending on their location) will limit the current and will force other strands, which are not saturated, to take more current. This means that the saturation of coupling loss is fully taken into account, just as all shielding effects from all current loops of individually connected strands in the cable.

As for MPAS, the JackPot coupling current loss, induced by the pulsed magnetic field inside the conductor, is compared to the energy deposited during the experiment, illustrating that the discrepancy between the measured and simulated MQE is less than about 10% for the Nb_3Sn sample, see Figure 4.8. On the other hand, the applied peak magnetic field is measured with much better accuracy than the temperature. The energy measured in SULTAN is well in agreement with the energy calculated by JackPot. The measured data have a peculiar trend at 0.1 K of temperature margin as shown in Figure 4.2. Jackpot simulation shows the same tendency at 45 kA of transport current and the peak electric field calculation confirms the saturation effect of the strands at low temperature margin. The simulated peak electric fields are 236 mV/m and 227 mV/m at the temperature margin of 0.1 and 0.3 K, respectively. The energy and the electric field simulated at 0.1 K of temperature margin is larger than at 0.3 K because the peak values of the magnetic field pulses are 0.37 T at 0.1 K and 0.36 T at 0.3 K. Therefore, in the case of 45 kA, the increase of energy at lower temperature margin depends on the higher magnetic field pulse.

On the other hand, at 40 kA the JackPot simulation does not show the increase of energy at 0.1 K of temperature margin. Since the applied magnetic field pulse is the same in the tests at 0.1 and 0.3 K of temperature margin, the energy deposited in the conductor has to be comparable as in the JackPot simulation. The hypothesis is corroborated by the simulated peak electric field, which has a similar peak value in the two simulations, 249 and 252 mV/m, respectively. Therefore, the reason for the discrepancy can be related to the temperature control system of the SULTAN facility. The system is not able to provide a stable temperature above about 8.5 K. This causes temperature fluctuation in the conductor, which can affect the stability of the sample. Thus, the energy, calculated at 0.1 K of temperature margin, has probably a higher error than the initially estimated 10%.

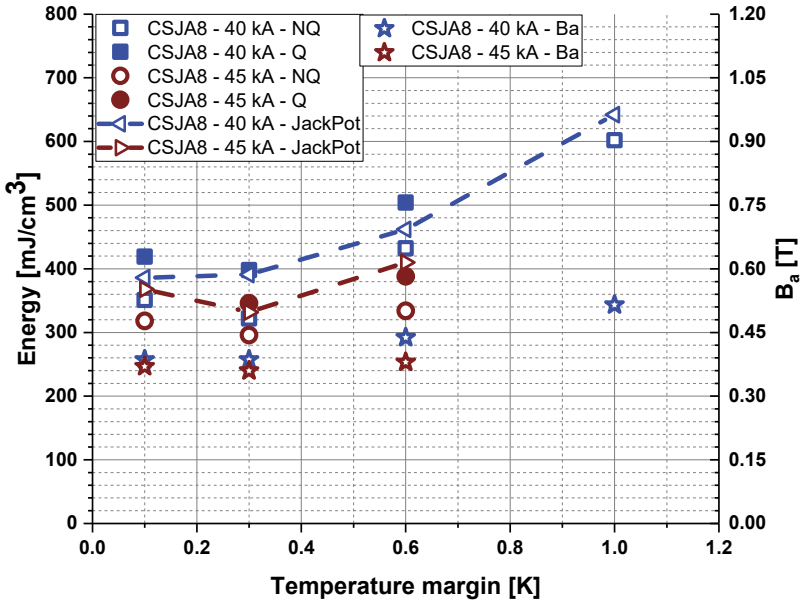

Figure 4.8 – Left axis: energy as function of temperature margin for the CSJA8 conductor. The markers represent the data from the SULTAN test (open symbols indicate recovery, full symbols quench) and the dashed lines represent the JackPot simulation of the SULTAN test in recovery conditions. Right axis: the magnetic field pulse peak value B_a, used for JackPot calculation. The test conditions are t_{pulse} = 0.128 s, B_{dc} = 9 T and I_{op} = 40 kA and 45 kA.

After the validation of the JackPot energy calculation, the combination JackPot-THEA is used to calculate the MQE as function of temperature margin.

Solving the MQE with JackPot-THEA is far more time demanding than using MPAS-THEA because it is necessary to run a JackPot simulation for every combination of magnetic field pulse and temperature margin. Therefore only one of the stability tests was reproduced with JackPot-THEA. The test at 40 kA was selected because of the larger temperature margin range, 0.1 to 1.0 K and because it corresponds to the CS operating current during the 15 MA Plasma Scenario. As in the experimental test, the energy in the conductor is generated by applying a fast singular sinusoidal pulsed field introducing coupling loss in the sample. The pulse is applied by stepwise increasing the peak value progressively until a quench occurs.

The JackPot-THEA computation results are shown in Figure 4.9. The red dashed line represents the calculated energy when the sample is still recovering from the pulse, while a quench occurs for the red solid line.

The combination of JackPot-THEA is able to predict well the experimental results within the entire range of temperature margin. The same can be said about the MPAS*-THEA combination although a correction factor was needed for the varies test conditions. This outcome implies that the JackPot-THEA combination can be used for extrapolation to different magnetic field peak values and time scale ranges, which opens the possibility of stability studies in the actual operating regimes of fusion conductors.

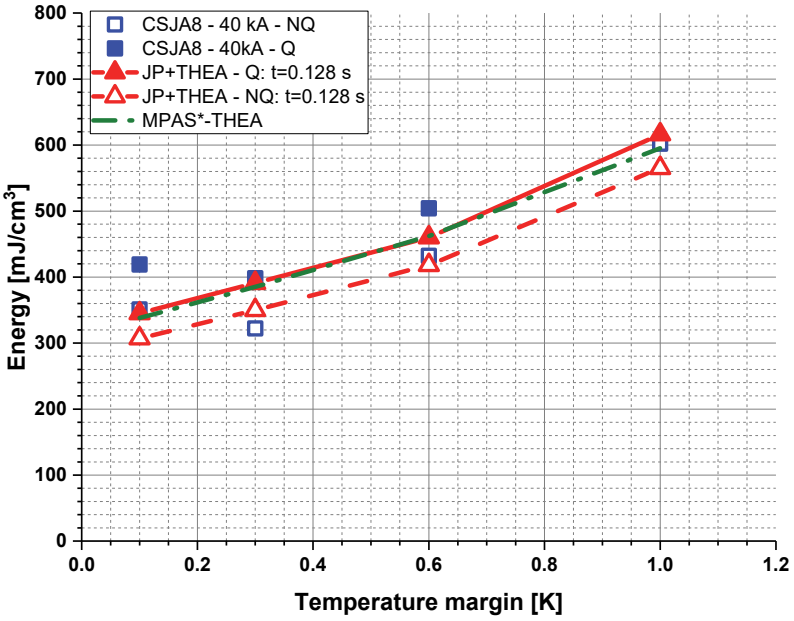

Figure 4.9 – Energy as function of temperature margin of the CSJA8 conductor. The square markers represent the data from the SULTAN tests, the red lines represent the JackPot-THEA MQE simulation results. The open markers and the dashed line indicate recovery, full markers and the solid line represent a quench. The green line reflects the MQE calculated with the MPAS*-THEA. The test conditions are t_{pulse} = 0.128 s, B_{dc} = 9 T and I_{op} = 40 kA.

4.4.3. Stability for 1 s pulse period

After the successful validation of the JackPot-THEA model, the stability simulation can be extended to different magnetic field disturbances, in order to evaluate the MQE for higher pulse durations and larger amplitudes. The electromagnetic and thermal test conditions are the same as used to model the SULTAN MQE tests, but the single sinewave pulse period is t = 1 s. With a longer pulse period it is necessary to increase the magnetic field peak value in order to initiate a quench. The magnetic

field peak value is selected in the range from 0.5 to 1.2 T. The predicted results of the MQE simulations are shown in Figure 4.10, together with the results obtained for a pulse period of 0.128 s. The effective MQE is between the solid and dashed lines, which represent quench and recovery of the conductor. Increasing the single sinusoid pulse period from t = 0.128 s to 1 s, equivalent to a factor of about 7.8, the MQE in the cable increases by a factor 2.1.

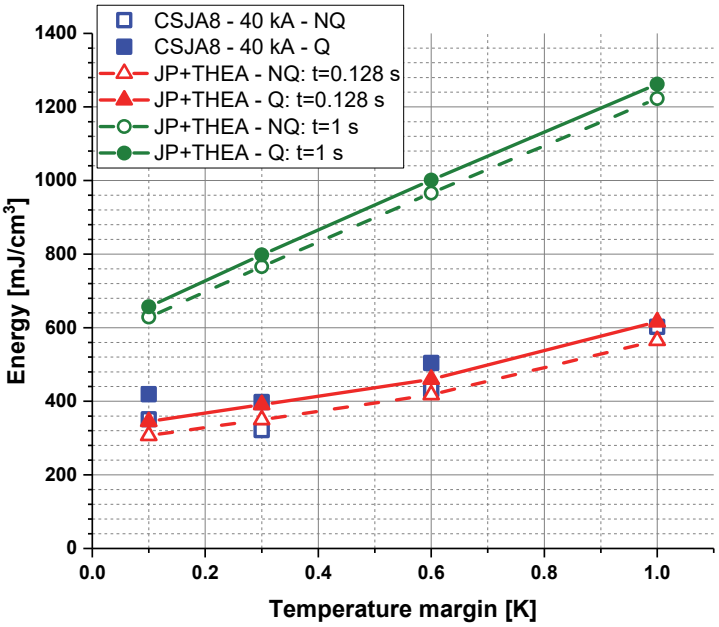

Figure 4.10 – Energy measured in SULTAN and calculated with JackPot-THEA, is shown as function of temperature margin. The square symbols are the data from the stability SULTAN test. The lines are the energy values calculated with JackPot-THEA, applying a magnetic field pulse of 0.128 and 1 s. Open symbols and dashed lines indicate recovery, filled symbols and solid lines indicate a quench. The test condition are B_{dc} = 9 T and I_{op} = 40 kA, B_a from 0.78 T to 1.14 T.

The saturation effect at a T_{margin} of 0.1 K, as observed for t_{pulse} = 0.128 s, seems to be not present at t_{pulse} = 1 s. This is likely due to the different current and electric field distribution in the strands associated with the larger pulse and longer heat diffusion time, extracting more heat from the strands and providing more scope for current redistribution.

The temperature profiles of the no-quench and quench simulations for 0.128 s and 1 s pulses are shown in Figure 4.11 and Figure 4.12 and the temperature is calculated in the high field zone.

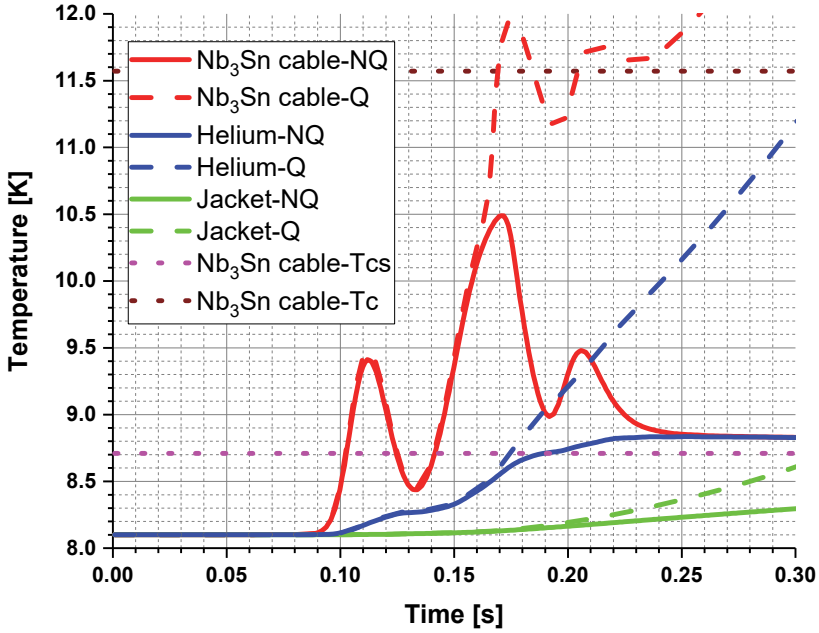

Figure 4.11 – CSJA8 conductor temperature versus time during JackPot-THEA stability simulation with 0.128 s sinewave pulse period. The solid lines represent the conductor recovery, while the dashed lines represent the temperature behavior during a quench. The horizontal dashed lines are the T_{cs} and the T_c of the sample. The applied test conditions are B_{dc} = 9 T and I_{op} = 40 kA.

For both simulations the initial temperature is T_{in} = 8.1 K. The quench starting point is different for the two pulses. For 0.128 s pulse period, it coincides with the second power deposition peak that corresponds to the maximum *dB/dt* of the sinusoidal pulse field. For 1 s pulse the third peak triggers the quench. The helium, due to the longer pulse duration, is able to extract more heat from the cable allowing a higher MQE for the 1 s pulse. Before quenching, the conductor can reach more than 10 K in both cases, while the helium temperature reaches 8.7 K during the fast pulse deposition and about 9.8 K with 1 s pulse. The helium shows a slower temperature increase than the cable, which is determined by the conductor wetted perimeter and heat transfer. The energy exchanged with the helium is directly proportional to the contact area. The wetted perimeter defines together with the helium heat transfer, the amount of heat that can be extracted from the cable per unit of time.

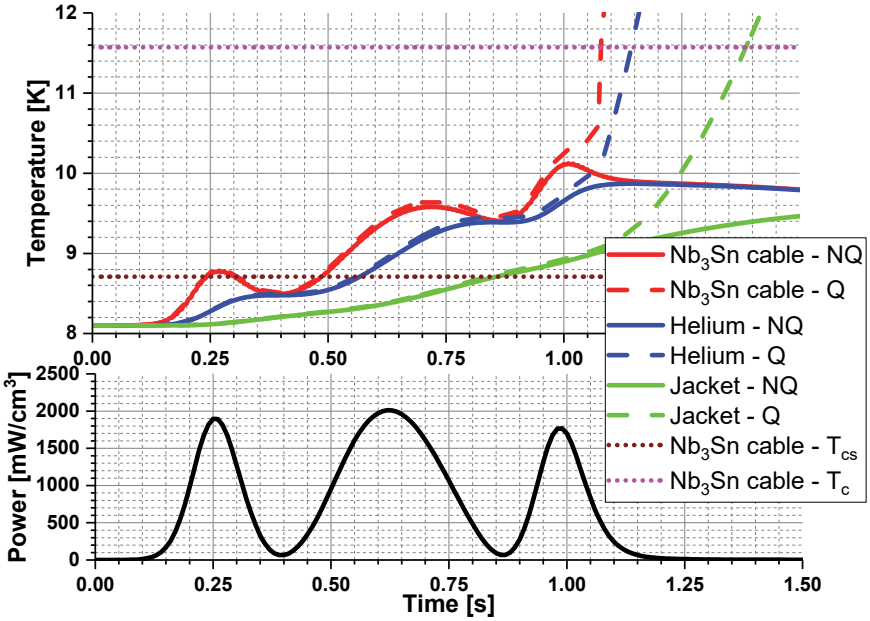

Figure 4.12 – Top: CSJA8 temperature versus time during JackPot-THEA stability simulation with 1 s sine wave pulse period. The solid lines represent the conductor recovery, while the dashed lines represent the temperature behavior during a quench. The horizontal dashed lines are the T_{cs} and the T_c of the sample. The test conditions are B_{dc} = 9 T and I_{op} = 40 kA. Bottom: power as function of time calculated with JackPot and used in the THEA simulation.

4.4.4. Stability for 5 s pulse period

Keeping the same approach and testing conditions as used for the 1 s pulse simulation, the pulse period is increased to 5 s. The magnetic field pulse peak value in the simulation is progressively increased until a quench occurs in the conductor. For a pulse period of 5 s, the helium temperature practically reaches equilibrium with the conductor. Therefore, both elements almost follow the same temperature profile. This implies that the helium cooling capacity [92] is completely used for a pulse period of 5 s, while it was not for faster pulses. The temperature profile of the stability simulation measured in the high field zone, starting at T_{in} = 8.1 K, is shown in Figure 4.13.

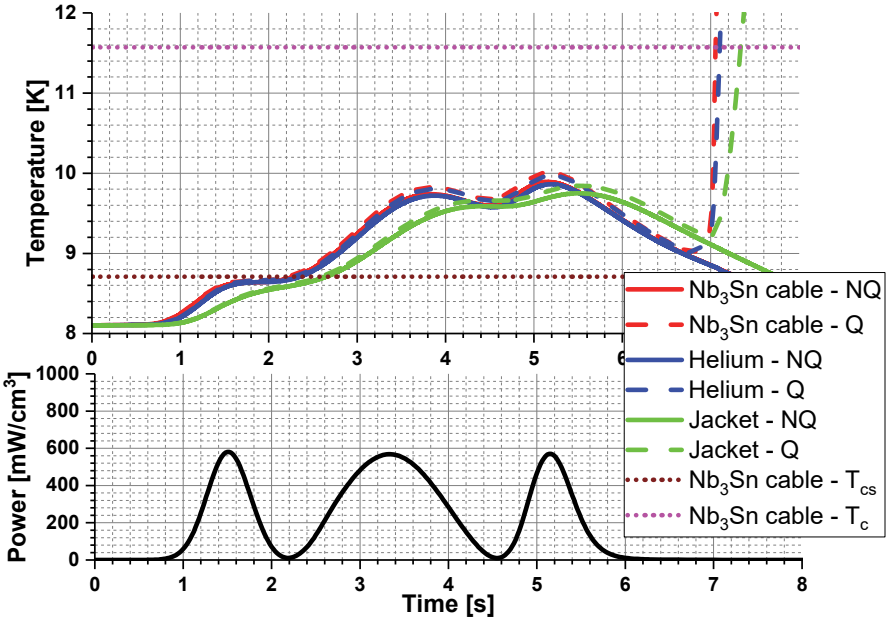

Figure 4.13 – Top: CSJA8 temperature versus time during the stability simulation with 5 s sinewave pulse period. The solid lines represent the conductor recovery, while the dashed lines represent the temperature behavior during a quench. The horizontal dashed lines are the T_{cs} and the T_c of the sample. The test conditions are B_{dc} = 9 T and I_{op} = 40 kA. Bottom: power as function of time calculated with JackPot and used in the THEA simulation.

The conductor reaches maximum temperature during the third power peak of the pulse and the cable quenches after a short decrease of temperature and time delay. This type of profile seems to be unrealistic at first sight, because of the temperature decrease before the quench. But this is due to the limitation of the 2D visualization that does not show the effect of the helium mass flow. The impact of the helium flow on the cable quench behavior can be understood from the plot of the temperature as a function of time and position in the cable in Figure 4.14. The two black solid lines define the high field zone boundaries. The T_{cs} is represented by the black dots on the surface. The helium flow direction is indicated in the graph. The temperature peak during the pulse deposition is reached at about 5 s, the temperature progressively keeps increasing, downstream the high field zone. The helium temperature is in quasi-equilibrium with the self-heating of the conductor, until the quench avalanche starts at around 6 s and the entire cable quenches. With 5 s pulse period, the effect of the mass flow becomes relevant. The helium flow is able to pass through the high field zone in about 7 s, therefore it is able to carry the

heat slug out of the high field zone during the heat deposition period, whereas the impact of the mass flow was almost negligible considering faster pulse period, like 0.128 s and 1 s.

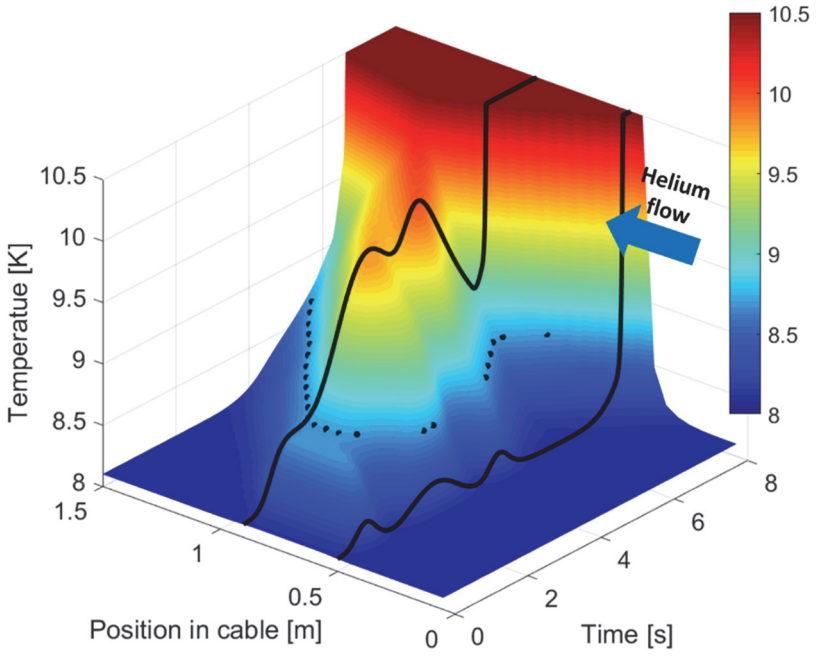

Figure 4.14 – CSJA8 conductor temperature evolution as function of time and position in the cable. The solid black lines define the high field zone where the heat is injected, the black dots the sample T_{cs}. Applied test conditions are: B_{dc} = 9 T, I_{op} = 40 kA and t_{pulse} = 5 s. The conductor central channel is blocked as in the SULTAN experiment.

Considering the quench temperatures (T_Q), see Figure 4.11, Figure 4.12 and Figure 4.13, it can be observed that T_Q decreases slowly with the increase of the single pulse period from 10.5 K for t_{pulse} = 0.128 s to 10.0 K for t_{pulse} = 5 s. For a longer perturbation able to generate a quench, the T_Q decreases but still holds $T_Q > T_{cs}$. The coolant flow, kept at the test initial temperature, removes part of the deposited heat from the cable, allowing the conductor to handle temperatures higher than T_{cs} for a short amount of time.

The results of the model in Figure 4.14 reproduce the SULTAN sample with the central channel blocked as for the original conductor. The increase of the magnetic field perturbation period raises the MQE because the helium has more time to

extract the heat from the conductor. Increasing furthermore the magnetic field pulse period, the MQE will probably saturate to a value related to the helium cooling capacity.

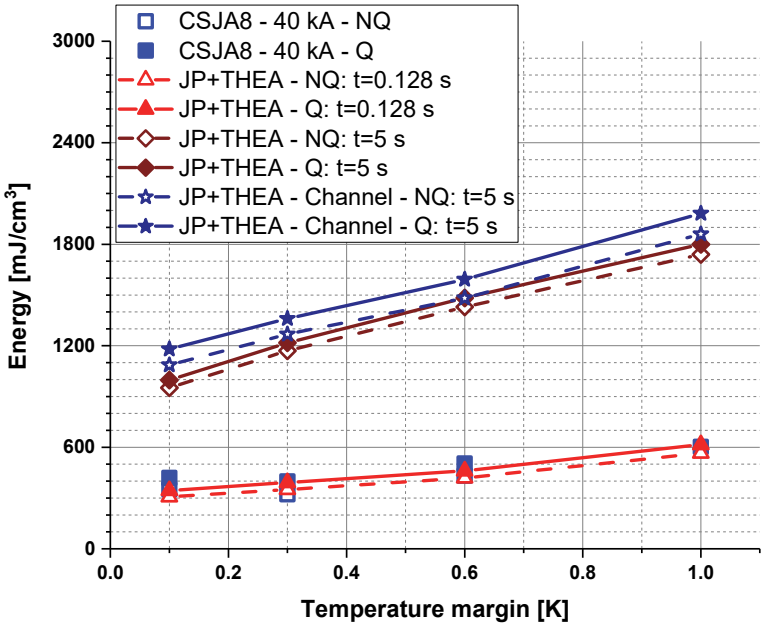

Figure 4.15 – Energy as function of temperature margin of the CSJA8 conductor. The square symbols are the data from the SULTAN tests, the lines are the energy values calculated with JackPot-THEA. Open symbols and dashed lines indicate recovery, full symbols and solid lines indicate a quench. The test conditions are B_{dc} = 9 T and I_{op} = 40 kA, B_a from 1.85 to 2.7 T. The applied magnetic field pulse periods are 0.128 and 5 s. The blue lines show the MQE of the conductor with open channel.

The absence of the central channel, by blocking it, has no impact on the stability test results, because the heat deposition period of 128 ms is too fast, as shown in section 3.4.4 [69]. In the THEA code, it is possible to implement the channel to study its effect at longer time period magnetic field pulses. The hydraulic parameters necessary to model the channel are taken from [5] and [93]. Appling the same testing conditions as used for Figure 4.14, i.e. same heat deposition profile, the sample with open channel is able to recover. The channel increases the MQE limit by improving the stability of the conductor in the case of a longer time period disturbance with lower *dB/dt* and higher amplitude. The stability simulation results, at different temperature margins with and without central channel, and compared to the test at 0.128 s pulse period, are shown in Figure 4.15. The increase of the MQE by unblocking the central channel is about 10% of the total energy deposited

in the conductor. The MQE for the 5 s pulse period is about 3.4 times higher compared to the MQE of the 0.128 s pulse period. In this case, the pulse period ratio is about 39.

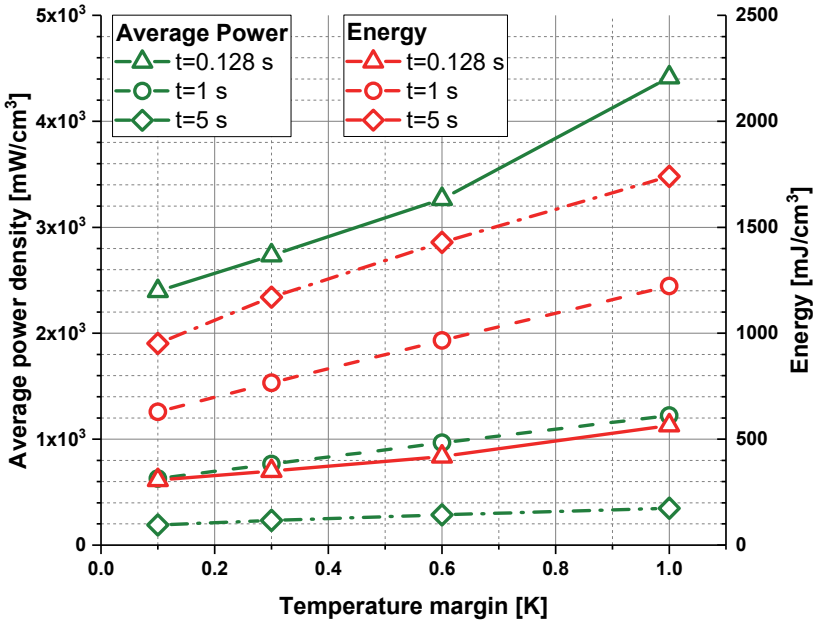

Figure 4.16 – Comparison of average dissipated power density and energy density versus temperature margin of sample CSJA8 simulated with JackPot-THEA at different pulse periods. The applied test conditions are B_{dc} = 9 T and I_{op} = 40 kA.

The comparison between the average power and the energy density dissipated in the CSJA8 sample during JackPot-THEA stability simulation with different perturbation pulse periods and temperature margins is shown in Figure 4.16.

Since the power profile is sinusoidal the average power is used to give an indication of the power deposition during the stability tests. The power has an opposite trend compared to the energy. Longer sinusoidal pulse perturbation periods correspond to a higher MQE, but the average power deposited during the perturbation is lower. To reach a quench in 5 s of heating, at 0.1 K of margin an amount of 950 mJ/cm^3 is required, whereas with a perturbation of 0.128 s it is sufficient to deposit about 300 mJ/cm^3.

4.4.5. Discussion

A clear tendency is observed for the MQE as function of the pulse time period in Figure 4.16. The relation between MQE and magnetic field pulse period can be roughly expressed as:

$$MQE = MQE_{ref} \cdot \left(\frac{t_{pulse}}{t_{ref}}\right)^{\frac{1}{3}}. \quad \textbf{(4.1)}$$

The MQE is proportional to the cubic root of the magnetic field pulse period. Considering the experimental MQE at t_{pulse} = 0.128 s as reference value, the modeled MQEs can be analytically calculated. The MQE and pulse periods for the 8.1 K simulations and their ratio are listed in Table 4.6.

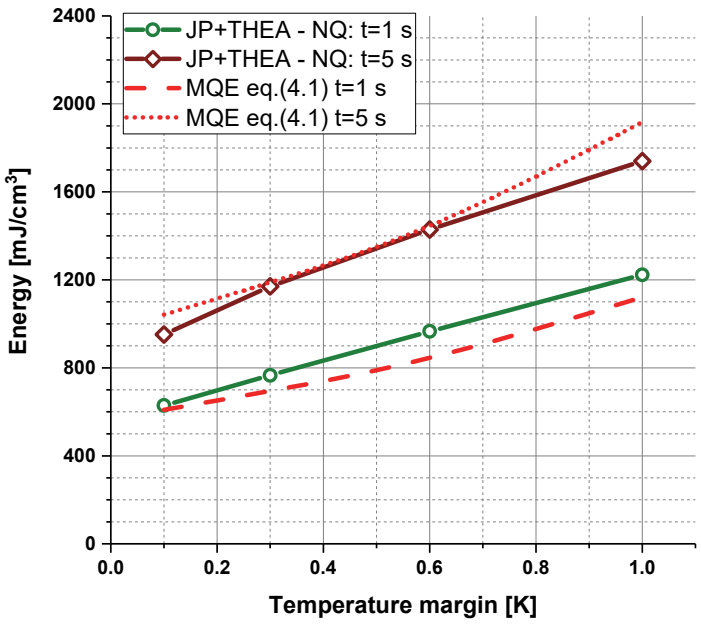

Figure 4.17 – Comparison between the MQEs versus temperature margin simulated with JackPot-THEA at different pulse period and extrapolated using eq. (4.1).

The energies calculated using eq. (4.1) are similar to the simulated MQE within 15% of error, see Figure 4.17. The trend of the curves calculated with eq. (4.1) is different from the curves simulated with JackPot-THEA because of the simplicity of the model. JackPot-THEA considers all the electromagnetic and thermal properties of

the system. While, eq. (4.1) rescales the MQE as function of the pulse period without considering the effect of the coolant, which changes increasing heat deposition period. Therefore, the relation can be valid only considering the test conditions constant and by varying only the magnetic pulse period and its peak value. This very simple approximation can be a useful rough estimation of the MQE for different perturbation periods. However, it does not give any information on the magnetic field peak value necessary to reach the MQE.

Table 4.6 – Summary of the magnetic field pulse periods and their MQE calculated at 8.1 K and the relative ratio's with the reference SULTAN pulse and MQE, t_{ref} = 0.128 s and MQE_{ref} = 418 mJ/cm^3 at T = 8.1 K.

	t_{pulse}/t_{ref}	*MQE [mJ/cm^3] (T = 8.1 K)*	MQE/MQE_{ref}	*MQE [mJ/cm^3] eq. (4.1)*
t_1 = 1 s	7.8	970	2.3	830
t_2 = 5 s	39	1430	3.4	1420

4.5. Conclusion

The power dissipation profile has an important impact on the cable stability, a more constant heat deposition, rather than a truncated sinusoidal deposition profile, can lead to a significantly different quench energy threshold. Further investigation on different dissipation-time profiles is necessary to better comprehend Plasma Scenario predictions.

The Nb_3Sn conductor, contrarily to the NbTi conductor, is able to recover from the power deposition even if the temperature crosses the current sharing temperature; the difference in *n*-value is probably in essence responsible for this phenomenon.

The MPAS and JackPot models were compared after combining them with the THEA model for computation of the MQE. For the MPAS-THEA model combination it appears that MPAS is not capable to precisely predict the amount of power generated during a time varying magnetic field pulse for the Nb_3Sn CICC, other than from the magnetic field perturbation, temperature and current boundary conditions applied to the cable in the experimental test.

The JackPot model is able to calculate accurately the energy deposited inside a cable for any, time dependent, applied magnetic field, current and temperature. However, it is not adapted to compute the evolution of the quench propagation,

although it can give the instant in time of reaching the current sharing temperature. Thus, JackPot as stand-alone code is capable to estimate the MQE of NbTi CICC conductors, because the quench transition occurs immediately when reaching the current sharing temperature. Nb_3Sn CIC Conductors, on the other hand, are able to reach temperatures far above the current sharing temperature before quenching, therefore JackPot alone is not able to predict their MQE accurately. Nonetheless, the combination JackPot-THEA is able to predict the SULTAN MQE test results for the ITER CSJA8 sample with excellent agreement. This implies that JackPot-THEA provides a good basis for stability analyses of ITER coils subjected to severe alternating magnetic fields like the plasma operating scenario. This is particularly useful in the case decisions have to be made about changes in the Plasma Operating scenario of ITER or another fusion reactor.

The JackPot-THEA extrapolated results towards longer pulse duration show the dependency of the MQE with the sinusoidal magnetic field pulse period. The MQE becomes larger with increasing magnetic field pulse period because the helium has more time to cool down the conductor thereby improving the stability. The cooling effect of the helium is more effective for long perturbation time, and thus the conductor is more unstable when it is subject to fast heat deposition.

The 5 s slow pulse simulation shows the influence of the central channel on the stability. Unblocking the central channel increases the MQE margin by about 10%.

The extrapolation of stability test simulations, from 0.128 s (SULTAN test results) to the 5 s range by using JackPot-THEA, makes it possible to perform a quantitative comparison between short sample stability tests and the ITER Plasma Scenario.

5. STABILITY OF ITER CENTRAL SOLENOID CONDUCTOR DURING THE 15MA PLASMA SCENARIO

5.1. Introduction

After the validation of the JackPot-THEA model and the extension of the stability studies of the CSJA8 conductor to conditions comparable to the baseline plasma operating scenario, it is feasible to analyze the performance of the ITER Central Solenoid and to predict the stability of the Central Solenoid conductor under realistic load conditions.

The current distribution calculated at strand level and the corresponding power dissipation allows the evaluation of the local peak electric field during the plasma scenario. The peak and the average electric fields generated during the 15 MA plasma scenario are compared to the electric fields of the short sample stability simulations. With JackPot-THEA, the temperature evolution in the conductor during the plasma scenario can be calculated. This is used to investigate the temperature evolution of one full layer of the CSU2 quadra-pancake exposed to the most severe magnetic field conditions.

5.2. ITER Central Solenoid design and plasma scenario

The Central Solenoid consists of a stack of 6 coil modules. All modules are identical circular coils built with Nb_3Sn CICCs. The total solenoid height is about 13 m and the diameter amounts to 4.3 m, see Figure 5.1. Each module comprises 7 pancakes wound with in total 40 layers of 14 turns each. The 7 pancake coils are 6 so-called hexa-pancakes and 1 quad-pancake [94]. The modules are identical and interchangeable. The CS winding configuration of each module is summarized in Table 5.1.

Table 5.1 – CS winding configuration for each module [94].

Pancake type	*CICC length [m]*	*Number of units*	*Number of turns*
Hexa	903	6	83.25
Quadra	601	1	55.5
Total module	6019	7	555

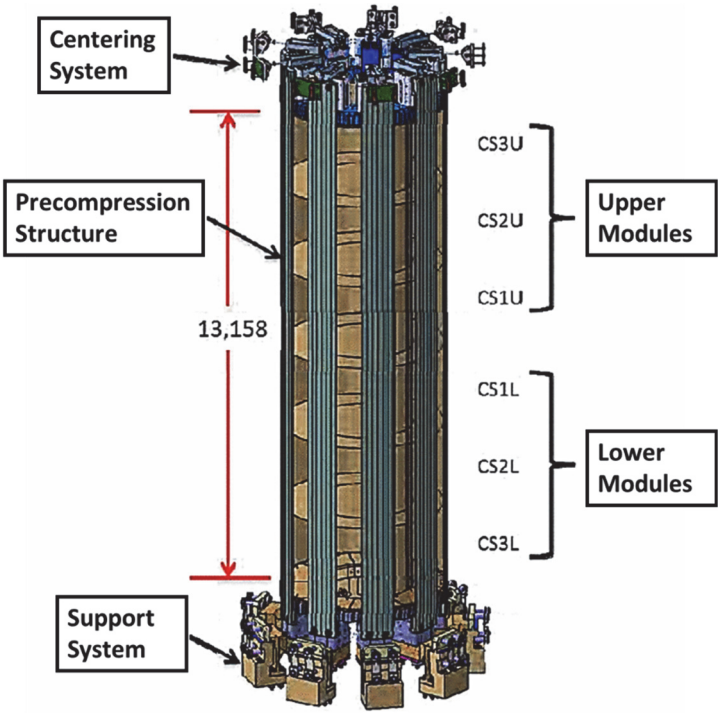

Figure 5.1 – Overview of the Central Solenoid [94].

The supply and return lines from the feeder ducts provide helium cooling. Helium is supplied with 20 inlets connected to the inner turns of the module. The in-lets are located in the inner bore between every two layers to supply the high magnetic field region with the coldest helium. Helium flows in both conductor directions away from the inlet joint. The helium outlet is reached after approximately 14 turns (1 layer), see Figure 5.2. Every outlet receives helium from two different inlets and they are placed at the outer side of the pancakes [95]. The plasma scenario chosen for the present study is the 15 MA Plasma Scenario as previously implemented in JackPot [96]. Figure 5.3 shows the currents in the CS modules during the 15 MA plasma scenario. The start of the discharge begins at t = 0 s, and the following seconds are characterized by the highest magnetic field rate. The worst conditions in the CS occur in the CSU2 and CSL2 modules [96], in particular in the inner turns of the quadra-pancakes since they experience the highest magnetic fields while fast ramping.

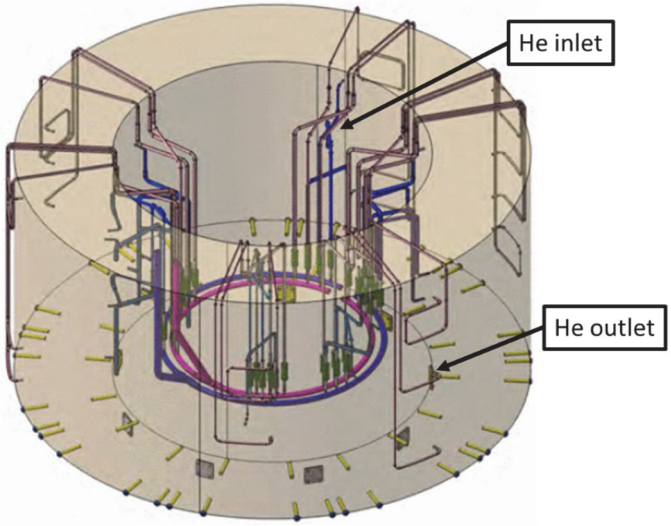

Figure 5.2 – Cooling system schematic of one module of the ITER Central Solenoid [94].

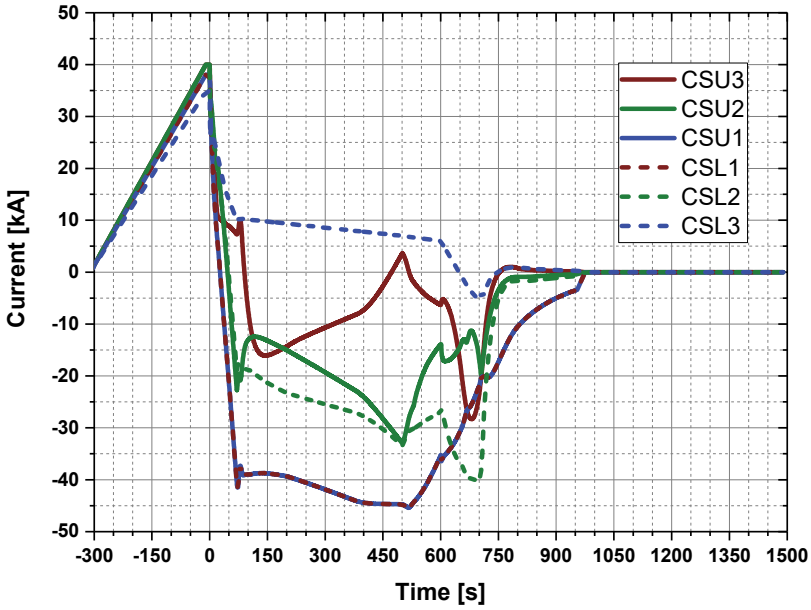

Figure 5.3 – Nominal operating current versus time in the six CS modules during the 15 MA plasma scenario. From -300 s to 0 s the currents in the coils are ramped up, and then quickly swept down generating the magnetic field rates.

5.3. JackPot-THEA electric field threshold definition

JackPot is able to calculate precisely the power generated during the magnetic field pulse and the linked current and electric field distributions in the cable, see section 4.4. The local electric field is calculated using eq. (3.2)**.** Knowing the moment the quench starts, the peak electric field for the MQE (E_Q) and the average of the electric field (E_{avg}) can be calculated. Since the coupling current is proportional to $(dB/dt)^2$, the power dissipation and the electric field are inversely proportional to the pulse period. Therefore, the electric field at the instant of MQE is lower for longer pulse periods. This is also related to the effective temperature of the helium during the energy deposition. For fast deposition, see Figure 4.11, the helium temperature is lower than the temperature of the conductor during the pulse. This allows the conductor to reach a very high peak electric field and yet being able to recover after the end of the pulse. Whereas for longer pulses, see Figure 4.12 and Figure 4.13, the temperature gradient between the helium and the conductor decreases and the conductor is not able to recover even if the peak electric field is lower than for a shorter pulse.

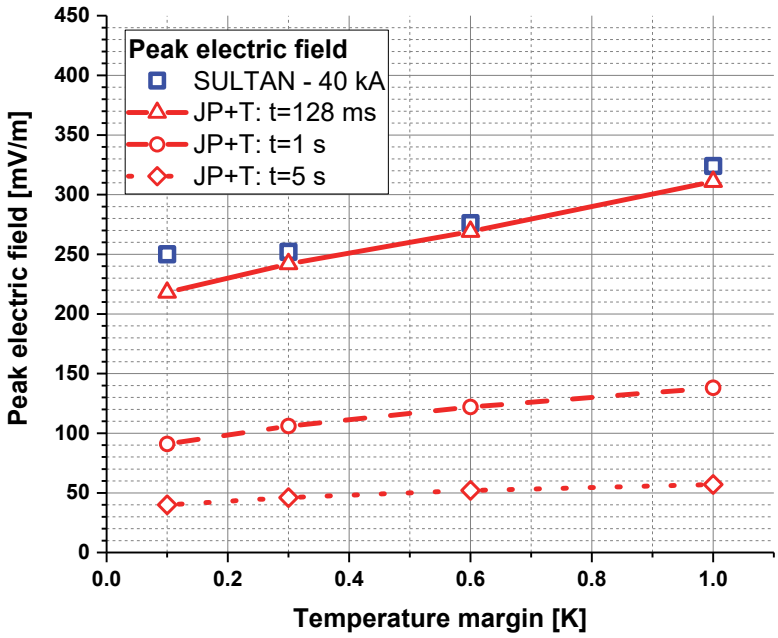

Figure 5.4 – CSJA8 conductor peak electric field as a function of temperature margin and pulse period simulated with JackPot-THEA, compared to the peak electric field calculated from the SULTAN stability test. In all simulations B_{dc} = 9 T and I_{op} = 40 kA.

The peak and the average of the electric fields as a function of the pulse period and temperature margin are shown in Figure 5.4 and Figure 5.5, respectively.

The E_Q is compared to the peak electric field calculated by scaling from the SULTAN fast pulse tests in Figure 5.4. The E_{avg} is compared to the average electric field measured during the T_{cs} tests on different CS samples [96] in Figure 5.5. When the magnetic field pulse period of 0.128 s is applied in the temperature margin range T_{margin} = 0.1 to 1 K, the simulated peak electric field E_Q is about 200 to 300 mV/m, while the average electric field E_{avg} is 5 to 8 mV/m. E_Q and E_{avg} are 4 and 2 orders of magnitude larger than the critical current criterion E_c (10 µV/m), respectively. When increasing the pulse period, the electric fields decrease and E_{avg} reaches a value of about 450 µV/m at t_{pulse} = 5 s. This value approaches the average electric field at quench, measured in quasi-steady state conditions on CS conductors during the T_{cs} tests performed in SULTAN, which is about 200 to 400 µV/m.

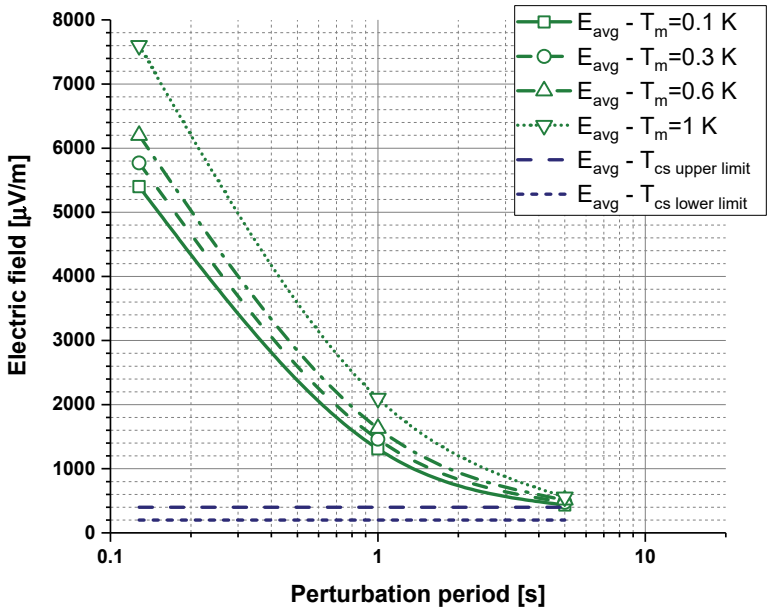

Figure 5.5 – Average electric field as a function of the perturbation period and the temperature margin of the sample CSJA8 simulated with JackPot-THEA and compared to the quench electric field measured in SULTAN T_Q tests performed on ITER CS samples [96]. In all simulations B_{dc} = 9 T and I_{op} = 40 kA.

Figure 5.5 also illustrates that the calculated average electric field for pulsed fields asymptotically approaches the values found for a quasi-steady state experimental

test with constant transport current and magnetic field but slowly increasing temperature. This is a valuable indication that the JackPot predictions are quantitatively correct. The simulated average electric field coincides with the experimental critical electric field measured in DC conditions, proving that the extrapolations made with JackPot-THEA are in good agreement with the SULTAN experimental results. In combination with the good agreement between experiment and computation of MQE for fast pulses, this gives confidence to the predictive potential of JackPot to quantitatively foresee the behavior of CIC Conductors which can be used to improve their design.

The electric field measured under DC conditions can be used to analyze the limits of quasi-stationary magnets in cases where the magnetic field is constant or has very long fluctuation periods. On the other hand, in varying current and pulsed magnets the conductors show the ability to amply cross the E_c criterion before quenching. From the simulation results, we can argue that the quench occurs after reaching a certain threshold of electric field. Consequently, E_Q and E_{avg} can be used as quantitative threshold for this type of conductors in relation to the operating conditions.

In practical terms, taking as example the ITER Central Solenoid, JackPot can be used to calculate the peak electric field during the plasma scenario. If the calculated electric field values are comparable or higher than the electric field threshold, the CS conductor will operate in critical condition. In other words, the CS conductor will operate in optimal condition if its peak electric field is significantly lower than the threshold.

5.4. JackPot Plasma Scenario short sample simulation

As mentioned, JackPot is able to simulate a Plasma Scenario for a relatively short section of conductor to limit the computation time for the given size of the matrix dimensions. One meter of CICC is a good compromise between computation time and minimum relevant sample length.

The entire ITER magnet system is taken into account for the JackPot computation, modeling the precise effect of the changing external magnetic field magnitude and orientation in time on the cable section. The magnets are represented using the current center lines [96]. This simplified model allows to describe the ITER magnetic

field distribution and to identify and define the region with the most extreme magnetic field conditions.

5.4.1. Magneto-resistance and Lorentz' force effect

During the coupling loss and MQE simulations for the SULTAN samples, the magnetic field and current are taken constant. While during the Plasma Scenario, they are varying continuously. The variation of the copper magneto–resistance and the Lorentz' forces, resulting from the changes in the applied current and magnetic field, have an effect on the inter-strand resistance. The coupling and eddy current losses generated in the conductor also depend on these two parameters. Unfortunately, the effects of these two phenomena cannot be easily predicted because it is not possible to directly measure the resistance variation in the conductor during operating conditions. The effect of the Lorentz force on the strand contact resistance was investigated in [70] and [97], but without transport current. To estimate the effects of current and magnetic field variation on the inter-strand contact resistance the SULTAN AC loss results after cycling are used. The CSJA8 conductor sample was tested at three different conditions, for each of them JackPot solved an inter-strand resistivity to match the coupling loss results, see Table 5.2.

Table 5.2 – CSJA8 conductor sample inter-strand resistivity simulated with JackPot and nτ determined from SULTAN AC loss tests.

Test conditions	*CSJA8 inter-strand resistivity [$\mu\Omega m^2$]*	*nτ [ms]*
B_{DC} = 2 T, I_{op} = 0 kA	$0.9 \cdot 10^{-5}$	105 ± 1
B_{DC} = 9 T, I_{op} = 0 kA	$1.5 \cdot 10^{-5}$	52 ± 1
B_{DC} = 9 T, I_{op} = 40 kA	$0.4 \cdot 10^{-5}$	117 ± 1

Assuming a linear dependence of the resistivity on magnetic field and current, a plane can be defined based on the three resistivities, see Figure 5.6. The inter-strand resistivity for every applied current and magnetic field is described by using the surface equation. In order to avoid negative values for the resistivity, a minimum is defined as $\rho_{\min} = 0.1 \cdot 10^{-5}\ \mu\Omega m^2$, although in practice the simulations did not reach this limit. The black line in Figure 5.6 represents the resistivity evolution in the most inner turn of the CSU2 unit as a function of the background

magnetic field and current during the 15 MA plasma scenario. To simplify the figure, only the absolute value of the current displayed.

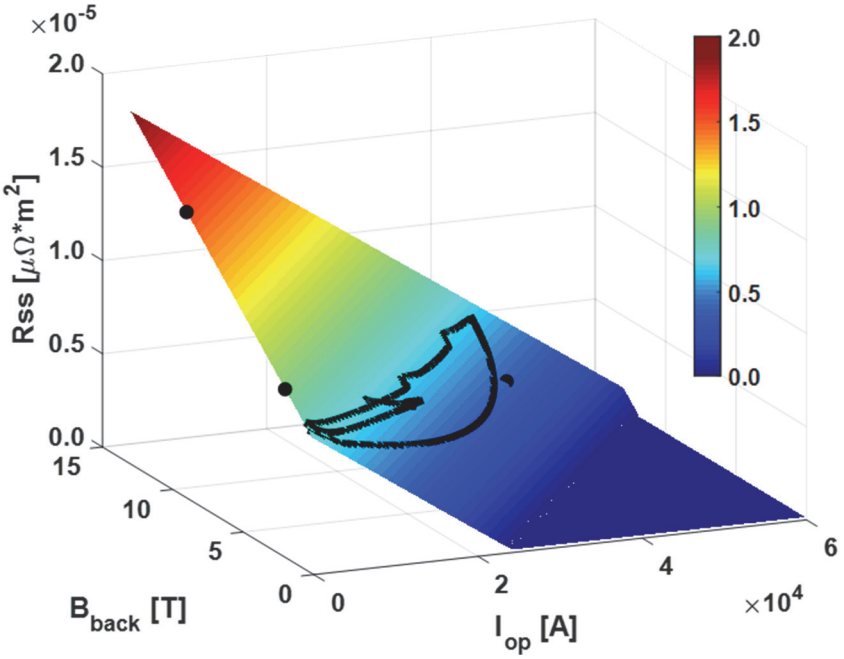

Figure 5.6 – Inter-strand resistivity surface, depending on the variation of background magnetic field and transport current. The black dots are the resistivity values listed in Table 5.2. The black line represents the resistivity variation during the first 100 s of the 15 MA Plasma Scenario simulation.

5.4.2. Simulation results

Using the CSJA8 conductor and strand parameters, listed in Table 4.2, the first 100 s of the ITER 15 MA Plasma Scenario were simulated. The chosen interval is the most severe one for the coil. The inter-strand resistivity is defined using the surface defined in Figure 5.6. The applied current and average magnetic field during the first 100 s after Start Of Discharge (SOD) of the coils are shown in Figure 5.7.

The resulting coupling loss, see Figure 5.8, is comparable with the simulation performed for the analysis of the Short Twist Pitch (STP) sample presented in [96]. The performance of the conductors are not directly comparable because the Lorentz force effect was not considered in [96], but still the results are quite similar. The highest coupling dissipation occurs during the first two seconds of the Plasma

Scenario. At *t* = 0 s the coupling and eddy current losses are about zero but due to the logarithmic scale the initial ramp is not visible. The initial power is not zero because of the charging of the coils, see Figure 5.3. The current ramp up and the increase of the background magnetic field generate small coupling and eddy current losses in the conductor, but they are negligible compared to the power loss after the plasma initiation.

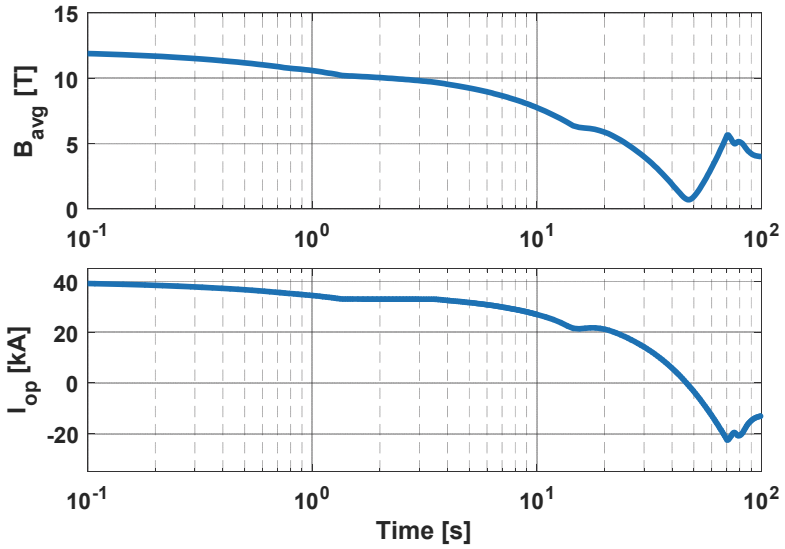

Figure 5.7 – Current and average magnetic field evolution as function of time during the first 100 s of the ITER 15 MA Plasma Scenario [17].

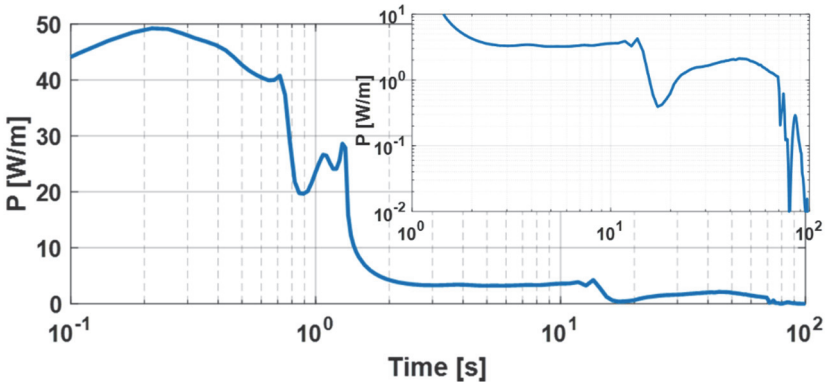

Figure 5.8 – Coupling and eddy current losses in watt per meter versus time of the CSJA8 conductor during the first 100 s of the ITER 15 MA Plasma Scenario. In the inset, the power versus time at t > 1 s is presented in logarithmic scale.

The hysteresis loss, see Figure 5.9, shows a similar behavior in the first seconds after the Start of Discharge compared with the coupling loss, but shows a prominent peak around t = 50 s. The peak is the result of a strong reduction of the magnetic field combined with a change of the angle between magnetic field and strands [96]. The hysteresis loss is negligible for most of the time; it is comparable to the coupling loss only during the peak at 50 s.

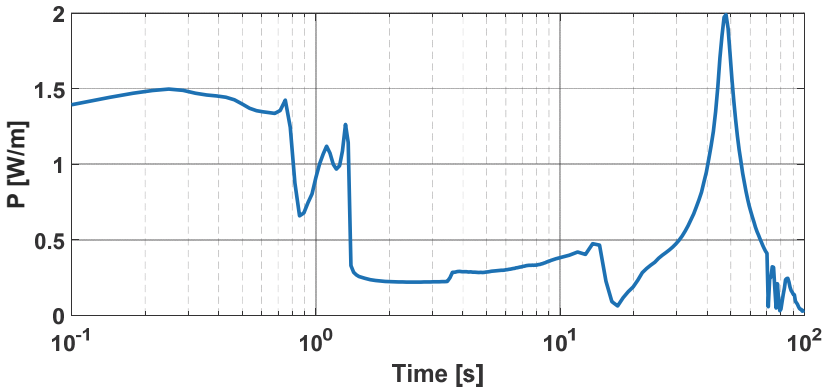

Figure 5.9 – Hysteresis loss in watt per meter versus time of the CSJA8 conductor during the first 100 s of the ITER 15 MA Plasma Scenario.

The stability of the conductor can be defined using the peak and average electric fields, as shown in Figure 5.4 and Figure 5.5, respectively. The average electric field of the conductor is compared to the electric field at quench measured during the SULTAN DC T_{cs} tests. The E_{avg} is always lower than the quasi-steady-state quench electric field limit in the range of 200 to 400 $\mu V/m$, see Figure 5.10. The stability is related to the time duration and space distribution of the disturbance [55]. As observed in Figure 5.4, a conductor in transient condition is able to reach higher local electric field and power deposition depending on the pulse duration. The CSJA8 short sample peak electric field simulated with JackPot-THEA is used as a threshold to study the stability of the conductor. The peak and the average electric fields after SOD reaches 7 to 8 mV/m and 180 to 190 µV/m, respectively, for a perturbation period of about 1 s, see Figure 5.10.

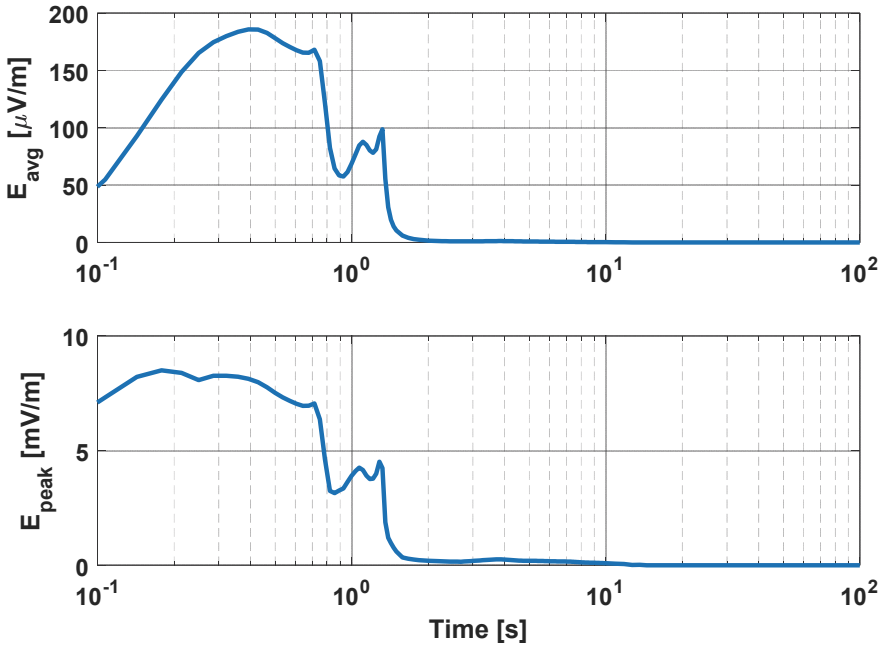

Figure 5.10 – Average electric field (top) and peak electric field (bottom) versus time, calculated for the first 100 s of 15 MA Plasma Scenario.

Crucial for the critical current of Nb_3Sn is the strain applied to the superconducting filaments. The effective strain applied to the strands depends on conductor cable pattern, coil design and forces applied to the conductor. The study performed on the ITER Central Solenoid Insert shows that the hoop strain mitigates the effective strain of the CS conductors by about 0.1% compared to the straight SULTAN samples, improving the T_{cs} with about 0.6 K [98]. In order to study the impact of the different effective strain on the electromagnetic performance of the CS, several simulations are performed varying only the effective strain applied to the superconducting strands. The results are presented in terms of peak- and average electric field and compared to the stability electric field thresholds calculated with JackPot-THEA, see Figure 5.11. The peak- and average electric fields during the plasma scenario are one order of magnitude lower than the stability threshold. The variation caused by the different effective strain is within 10%. Based on the defined electric field criteria, the 15MA plasma scenario should not have any stability issues.

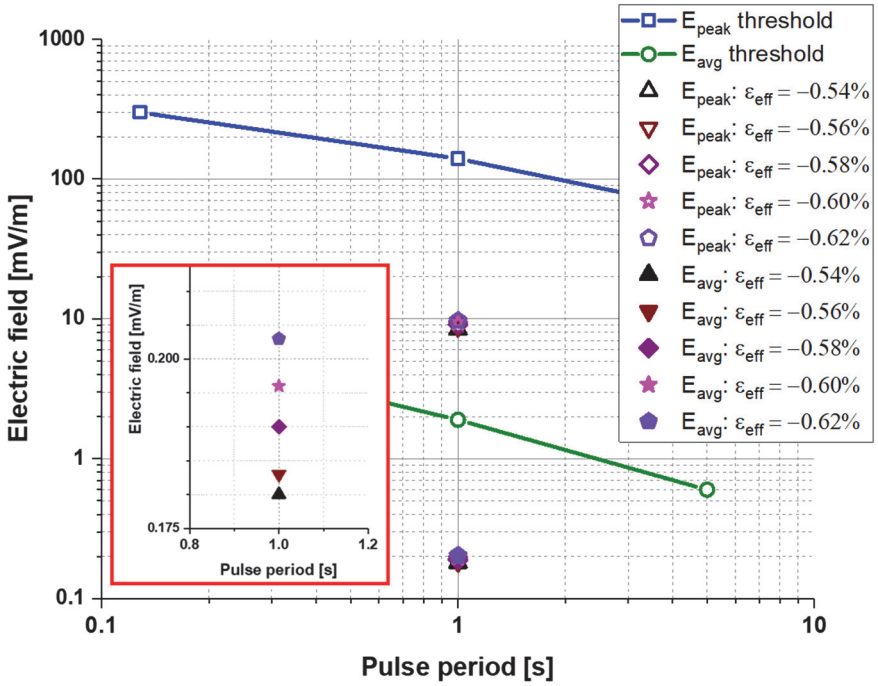

Figure 5.11 – Electric field as a function of the perturbation pulsed period. The open markers represent the peak electric field at different effective strain, while the solid markers indicate the average electric field at different effective strains, both calculated for the period with maximum dissipation during the 15 MA plasma scenario. The peak- and average electric field thresholds are calculated from the MQE simulations performed with JackPot-THEA. In the inset, average electric field versus perturbation period is presented in linear scale to show the scatter between the different effective strains.

5.5. Temperature evolution in a layer of CSU2 module

The aim of this study is to model the thermal behavior of the most critical layer of the CSU2 pancake from inlet to outlet during a full 15 MA Plasma Scenario cycle and subsequent cycles. The simulation is performed using the JackPot-THEA model as already validated and calibrated with the SULTAN short sample tests results. The simulation involves one layer of the CSU2 quadra-pancake, i.e. about 150 m of Nb_3Sn CICC. It is not practical to model such length of conductor at once with JackPot considering the amount of memory and CPU time necessary to simulate the entire conductor. A good compromise in terms of conductor length, computation time and available memory is to model fourteen 1 m long sections of CICC, one section for every turn. Afterwards, the electromagnetic performance of each section is scaled to the length of the entire turn. This approximation is valid because

the current applied to the conductor is the same in all turns and the external magnetic field changes radially depending on the distance to the axis of the coil. Therefore, the external magnetic field can be considered constant in each turn. The simulated time interval is 1800 s, corresponding to the duration of the 15 MA Plasma Scenario from the coil charge to the end of the recovery time, see Figure 5.3.

The coupling and eddy current losses computed with JackPot are used as input for THEA to calculate the temperature evolution in the pancake layer from the helium inlet to the helium outlet. Both hysteresis loss and coupling loss are considered describing the thermal behavior as accurate as possible. In THEA, the power is injected as heating power directly in the superconducting element of the model, since the dissipation is generated mainly in the superconducting elements. The model does not consider other types of loss and thermal exchange between the turns is neglected. The conductor and the helium cooling are modeled using the same parametrization as for the CSJA8 short sample simulations [5], [99]. The helium flowing in the central channel is considered thermally linked to the helium in the bundle [100], [101].

5.5.1. JaskPot-THEA results

The results of the simulation are presented in two different views: 3D in Figure 5.12 and 2D in Figure 5.13. The evolution of the temperature is shown as a function of conductor length and time from the plasma initiation to the end of a full 15 MA Plasma Scenario cycle. The helium inlet is located at the origin of the axis, whereas the helium outlet is at 150 m. The temperature maximum is generated in the first turns of the pancake layer during the plasma initiation, where the electromagnetic conditions are most severe. Then the heat slug with higher temperature moves along the conductor transported by the helium mass flow. The temperature peak, about 5.5 K, propagates almost unvaried along the conductor and after about 800 s the peak reaches the outlet.

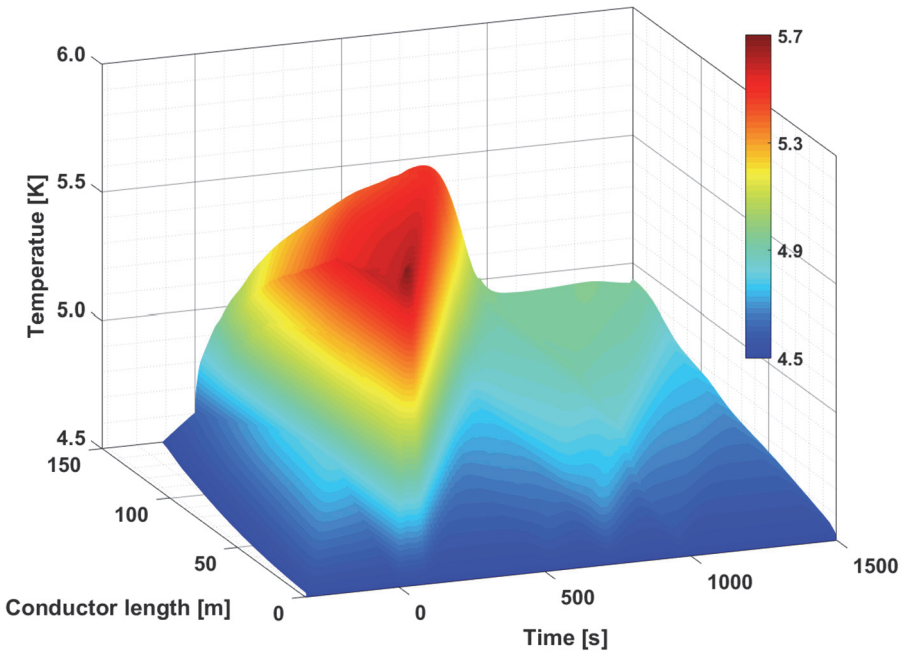

Figure 5.12 – Temperature evolution as function of conductor length and time inside the CSU2 quadra-pancake during the 15 MA Plasma Scenario. The plasma starts at *t* = 0 s, the current ramp up is not shown.

The absolute maximum temperature is located in the second turn, which is visible in Figure 5.13 at *t* = 100 s. The helium flows from the first to the second turn collecting heat from both turns and reaches the maximum temperature of about 5.6 K. The temperature peak becomes smoother in the following seconds, spreading the heat towards the coldest region, i.e. backward towards the helium inlet. The temperature maximum reaches the outlet after about 850 s from the start of the scenario. After this time, the temperature decreases progressively to less than 5 K. After *t* = 1500 s a new plasma scenario cycle can start with the current ramping up, see Figure 5.3. The aim of a tokamak is to drive multiple plasma cycles for a quasi-continuous energy generation, necessary for a power plant. From the final temperature, 4.5 K at the inlet and lower than 5 K at the outlet, multiple plasma cycle can be handled by the ITER Central Solenoid without overheating.

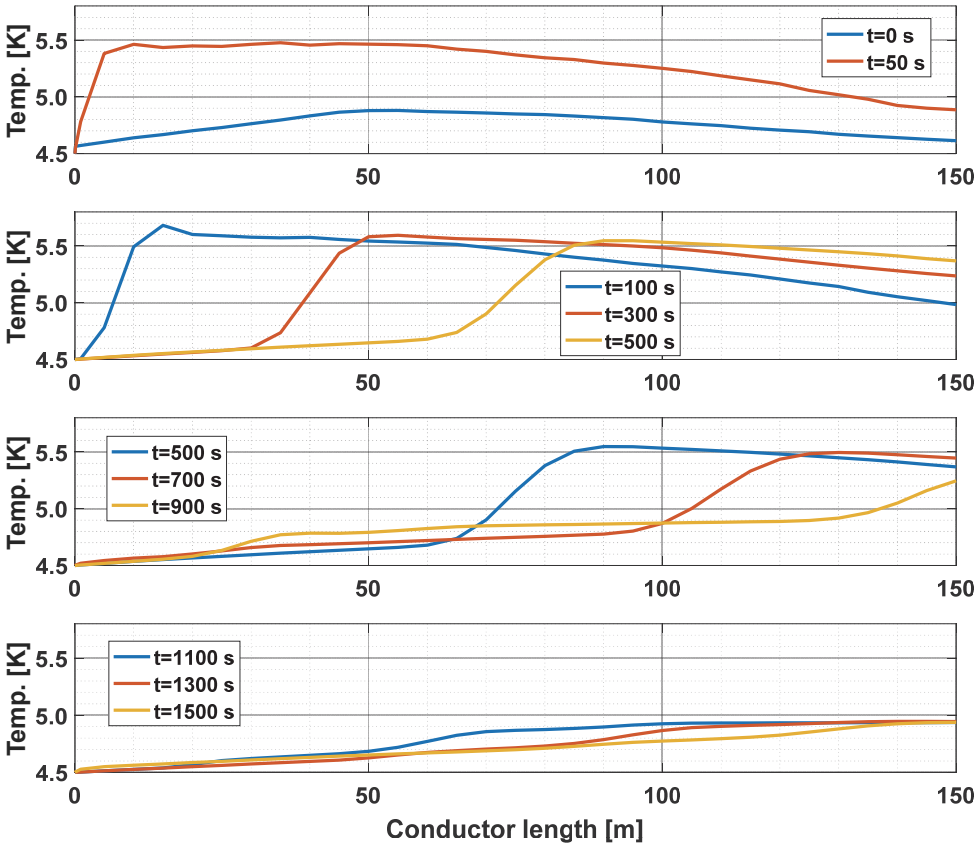

Figure 5.13 – Temperature evolution as function of conductor length and time inside the CSU2 quadra-pancake during the 15 MA plasma scenario. The plasma starts at *t* = 0 s, in the top figure. The temperature evolution during the Plasma Scenario cycle is shown in multiple time steps and ending at 1500 s in the bottom figure. The current ramp up is not shown.

5.6. Conclusion

It is essential for ITER operation to make sure that during a Plasma Scenario involving high field ramp rates the conductors in the Central Solenoid remains stable, i.e. no quench occurrence allowed during the peak value of the magnetic field change.

An electric field threshold for starting a quench in a characteristic Central Solenoid conductor is defined using the results from the JackPot-THEA simulations with

different pulse time periods. The E_Q and E_{avg} thresholds are significantly higher than the average quench electric field measured under stationary condition, in the range of 0.2 to 0.4 mV/m. However, the E_{avg} asymptotically approaches the experimental steady-state critical electric field for increasing magnetic field pulse period. This supports the credibility of the modeling.

During the 15 MA Plasma Scenario, the magneto-resistance and Lorentz force are taken into account considering linear dependences from operating current and applied magnetic field. The approximation allows simulating a more accurate model of the plasma scenario for determining the conductor stability.

The peak electric field during the Plasma Scenario always remains significantly below the quench electric field threshold. At the same time, also the average electric field of the conductor is way less than the electric field at quench under stationary condition. Given the defined electric field criteria, the ITER Central Solenoid does not show stability issues.

The simulation of the whole layer of the quadra-pancake of the CSU2 module provides a peak temperature of 5.6 K reached in the conductor. At the same time it describes the flow of the heat slug through the 150 m conductor in the pancake layer. The model confirms the capability of the Central Solenoid for continuous pulsed operation when exposed to the 15 MA Plasma Scenario burn cycles.

6. TOROIDAL FIELD CONDUCTORS FOR DEMO

6.1. Introduction

While ITER is under construction, the research and development for the next step demonstration reactor, in Europe called DEMO (DEMOnstration Power Station) is underway. Two different cable designs for DEMO's Toroidal Field coil conductors were developed by the Swiss Plasma Centre (SPC) and the Italian National Agency for New Technologies, Energy and Sustainable Economic Development (ENEA). The two conductors are referred to as WP1 and WP2, respectively.

DEMO conductors at present differ from the ITER ones not only in shape, being rectangular instead of circular [102], but also in the diameter of the strands, cable pattern and twist pitch. The WP1 and WP2 conductors were tested in the EDIPO facility at SPC and in the press facility at the University of Twente, under both DC and AC conditions. The experimental results are used to calibrate and validate the JackPot model for the new geometries. After the validation, a first stability analysis is performed to compare the peak electric field reached during a fast transient, to the ITER CS conductor electric field threshold as found in section 5.3.

In the last section of this chapter, the various diameters of the strands chosen for the ITER and DEMO Nb_3Sn conductors are evaluated. The diameter of the strand is 0.83 mm for ITER, 1.00 mm for WP2 and 1.50 mm for WP1. The impact of the strand diameter on the conductor stability is investigated by modeling three different ideal cable designs with JackPot. The conductor designs are chosen such that the effect of the different strand diameters is isolated from all other cable properties, as (sub)cable twist pitches, shape of the conductor cross section and segregated copper. The simulated electric field and coupling loss generated by the three samples are compared for an identical pulsed magnetic field condition.

6.2. Rectangular TF WP1 Conductor

The Winding Pack 1 (WP1, also called CRPP-RW1) conductor assembled at SPC is a React&Wind type of Cable [103], [21]. Figure 6.1 shows the schematic design of the conductor cross-section. The sample is composed of 17 petals, wrapped around a stainless steel strip in a rectangular shape, with every petal consisting of 18 Nb_3Sn

strands twisted around a copper core. The superconducting strands are distributed in two layers, containing 6 and 12 strands each, with twist pitches of 90 and 190 mm, respectively [104].

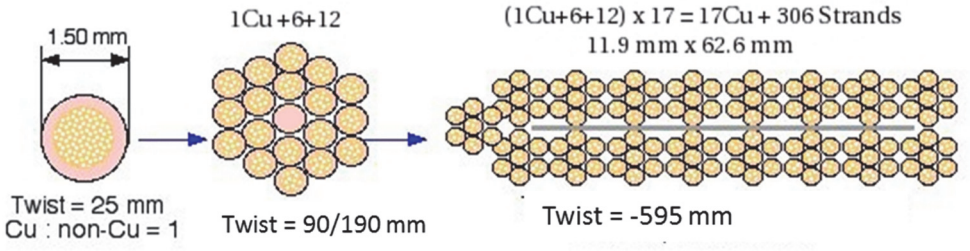

Figure 6.1 – Schematic design of the WP1 conductor [104]. The Rutherford type cable comprises 17 petals around a stainless steel strip, by which every petal is a double layer sub-cable with 18 strands superconducting strands in two layers.

The cable design is reproduced using JackPot AC/DC, see Figure 6.2. The geometry is particularly complicated to realize. For the ITER cable the petals rotate around the barycenter of the circular conductor cross-section, while for WP1 they have to follow a linear transposition along the plane sides of the conductor cross section, combined with an elliptical trajectory at the edges. To build this Rutherford-like geometry, a new-dedicated routine was added to JackPot. The resulting geometry is very similar to that of the real cable. The conductor shows a higher compaction at the edges, which in JackPot is converted to a larger overlay of strands. A 3D view of the WP1 geometry modeled in JackPot is shown in Figure 6.3.

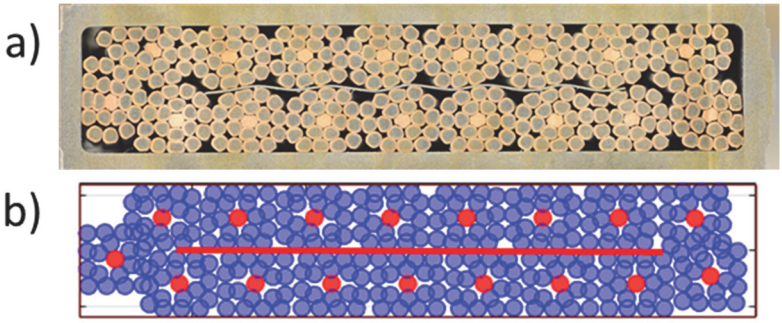

Figure 6.2 – Cross-section of the WP1 sample as tested at UT (a) and the JackPot geometry used for the simulations (b). Red dots are copper strands, while the red line is a representation of the stainless steel strip in the cable.

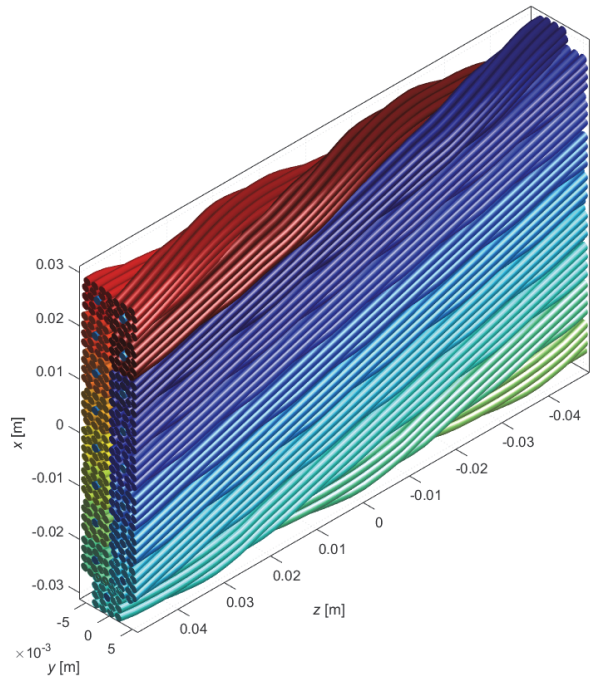

Figure 6.3 – 3D geometry of the WP1 sample modeled in JackPot AC/DC.

The Nb_3Sn strand in the WP1 conductor is produced by WST (Western Superconducting Technologies, Xian, China) according the internal Sn technology and has a diameter of 1.5 mm [103], see Figure 6.4. The wire specification and the characteristic critical current scaling law parameters, which follow eq. (1.5), are summarized in Table 6.1 [105].

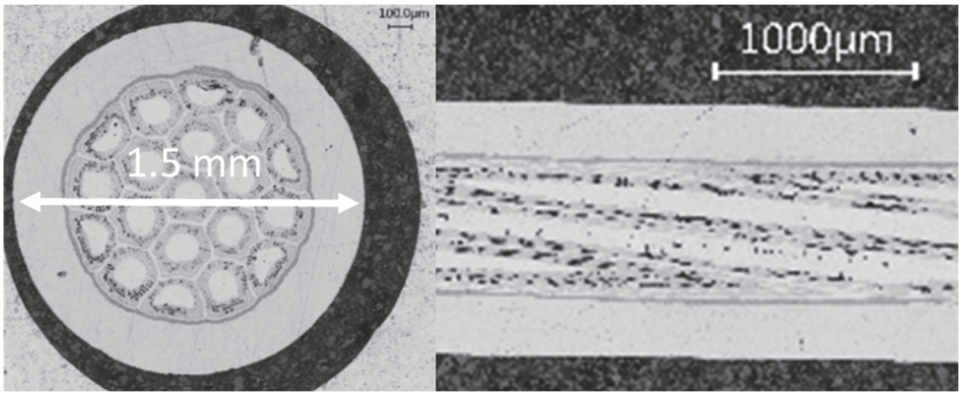

Figure 6.4 - WP1 Nb_3Sn strand cross section [106].

Table 6.1 – WP1 Nb_3Sn strand specification and parameters, used for the JackPot modeling [105], [107].

	WP1 - strand
Strand diameter [mm]	1.50 ± 0.02
Cu:non-Cu	1
RRR	>100
Critical current [A] at 4.22 K and 12 T	>800
B_{c20m}	33.24
T_{c0m}	16.34
C_{a1}	50.06
C_{a2}	0.0
ε_m *[%]*	-0.059
$\varepsilon_{0,a}$ *[%]*	0.312
ε_{appl} *[%]*	-0.03
p	0.593
q	2.156
C	73403
n_a	0.0
n_b	38.848
n_c	0.278

6.2.1. AC loss analysis

The AC loss measurements performed with the Cryogenic Cable Press and the AC Loss Dipole facilities, both at the University of Twente [108], are used to validate the JackPot simulation of the WP1 conductor. The sample was measured in virgin condition and after mechanical load cycling. Unlike the ITER type CICCs, the WP1 conductor cross section is rectangular and thus the AC loss depends on the orientation of the applied magnetic field. In the Twente Press facility, the DC background and AC magnetic field have the same orientation and they can be applied only in perpendicular direction to the sample, pointing to the broad side. However, in the AC Loss Dipole facility, the field direction can be parallel or perpendicular to the cable wide side, see Figure 6.5.

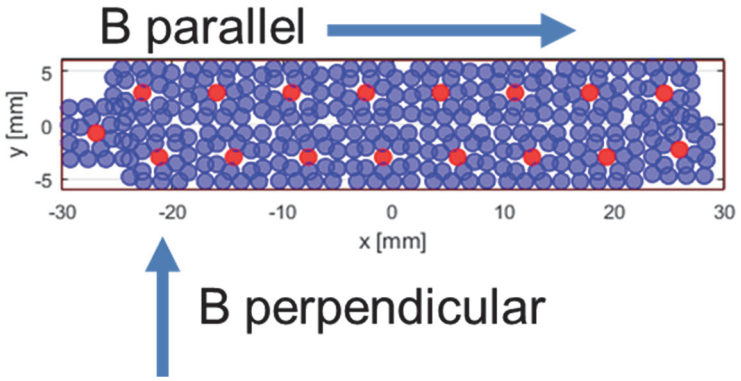

Figure 6.5 – WP1 magnetic field orientations during the AC loss measurements.

The hysteresis loss is linearly extrapolated to zero frequency and subtracted from the total AC loss [108]. The results of the coupling loss simulation in virgin condition for both directions of the magnetic field and after cycling (only available in perpendicular field) are summarized in Figure 6.6.

Using Jackpot, the coupling loss of the sample is always reproduced within 10% difference with the measured data. The coupling loss time constant of the conductor changes with the magnetic field orientation, showing the impact of the strong anisotropy of the sample on the coupling loss. The coupling loss measured in parallel magnetic field direction is one order of magnitude less than in perpendicular direction.

The WP1 sample does not have petal wraps. Instead there is a stainless steel foil between the two layers of petals causing an increase of the contact resistance and a reduction of the current sharing between top and bottom layers in the Rutherford cable, see Figure 6.2. The steel foil is modeled as increased contact resistance between the two layers, which is sufficient to block practically entirely the current transfer. The inter-strand and inter-petal resistivities are not influenced by the magnetic field orientation because the mechanical compression generated by the Lorentz forces (or force in the press) is considered as a homogeneous volume stress, equally distributed in all directions in the cross-section. Due to the absence of petal wraps, it is not necessary to use different values for inter-petal and inter-strand resistivities, but the strong overlay between different petals in the short edge of the model geometry, visible in Figure 6.5, requires a dedicated value of resistivity. JackPot finds a good agreement with the measurements for the perpendicular and parallel-applied magnetic field coupling losses in virgin condition

using the same resistivity values for both directions. With load cycling, usually the contact resistance increases and, in the model, this corresponds to an increase of inter-petal resistivity.

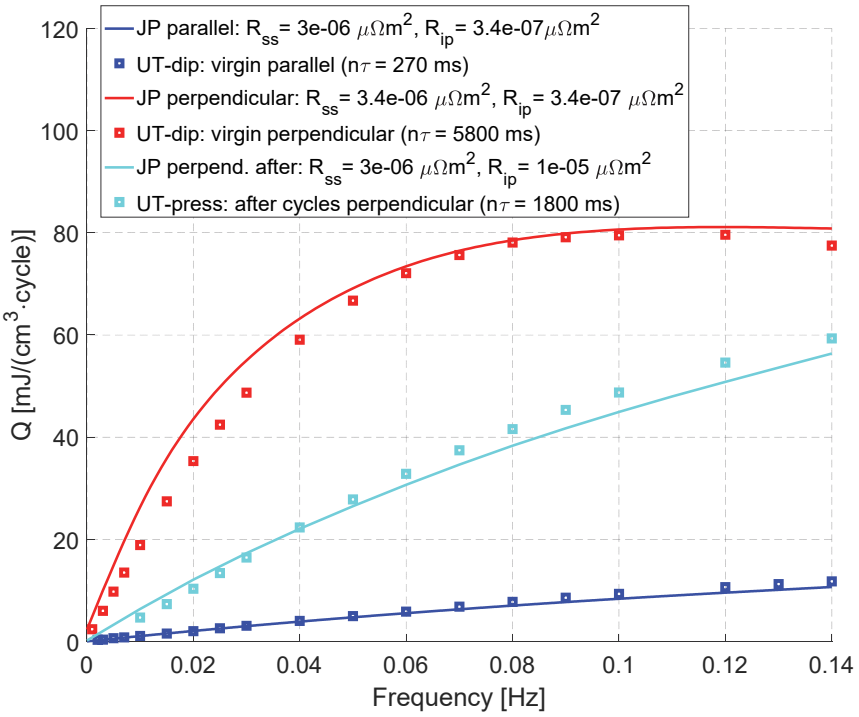

Figure 6.6 – Coupling loss as function of frequency. The dots represent the WP1 coupling loss measurements in the University of Twente Press and Dipole set up. The lines are the simulations performed with JackPot (JP), using B_{dc} = 0.35 T, B_a = 0.15 T and I_{op} = 0 A as boundary conditions.

Since JackPot was never validated before for a rectangular geometry nor for a Rutherford type of cable, it is necessary to benchmark the resistivity values extrapolated from the coupling loss simulation with the experimental contact resistance measurements. The direct measurement of the inter-strand and inter-petal contact resistances was performed in the Twente Press facility in virgin condition and as function of load cycles [108]. The contact resistance is determined from the voltage drop generated by an injected constant current between selected strand combinations. The scheme of the strand selection is shown in Figure 6.7.

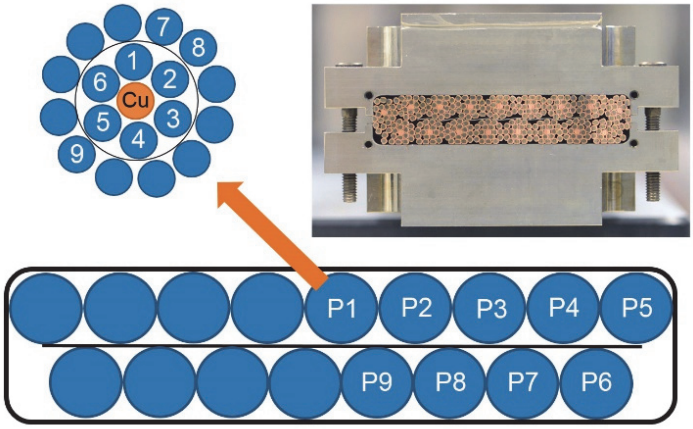

Figure 6.7 – Scheme of strand selection for the inter-strand and inter-petal contact resistance measurements [108].

The contact resistance measurement is reproduced in JackPot by using the same method followed during the experiment. Pairs of strands are connected to a constant current generator and the voltage drop between them is determined. The contact resistance is straightforwardly calculated by using Ohm's law. The simulation is performed using the same conditions as for the experiment, also following a similar scheme for selection of strand pairs, see Figure 6.7. The comparison between the measured and simulated contact resistances is shown in Figure 6.8.

At initial condition and after cycling, the measured resistance values are comparable with the model results. The maximum discrepancy is found for the inter-petal resistances after cycling, where the modeled inter-petal resistivity is two times bigger than the measured ones. The reason for the discrepancy can be related to the concentrated compression and strand overlap at the edges of the conductor in the model. The large overlap at the edges of the modeled conductor obviously does not reflect completely the real strand contact distribution. Since in JackPot, the calculated overlap is directly proportional to the variation of contact conductance, see section 2.3.3, a larger overlap corresponds to a larger contact surface and lower contact resistance. In the real conductor, see Figure 6.2, the strand compression in the corners looks less severe than in the model. To compensate for the overlap it is necessary to increase the inter-petal resistivity, which results in a higher inter-petal average contact resistance.

After the validation of the new cable geometry, using both coupling loss and resistance measurements, it is possible to provide a first stability evaluation for this type of cable.

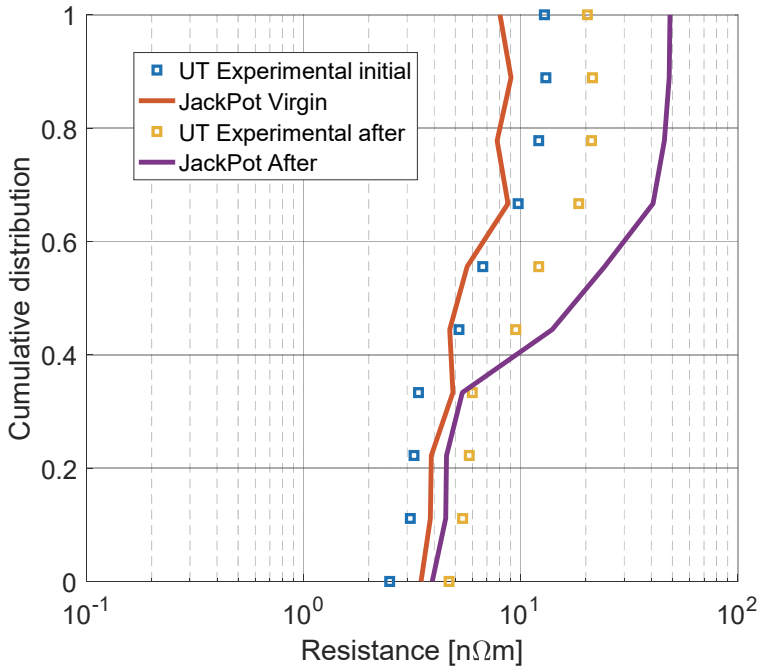

Figure 6.8 – Cumulative distribution of the inter-strand and inter-petal contact resistances of the WP1 sample. Dots are measured data [108] and lines are the simulation results in virgin condition and after cycling.

6.2.2. WP1 stability analysis

The measurements performed on WP1 are in low background field and without transport current. The effect of the Lorentz force on the contact resistance in operating conditions with high background field and transport current has to be taken into account. Considering previous simulations on CS conductors (Figure 4.7), the inter-strand resistivity at low background field and without transport current is of the same order of magnitude as the resistivity at high field and with current. In addition, the low void fraction of the WP1 cable ($\sim 15\%$) does not allow large displacement of strands. Therefore, as a first order assumption, the resistivity used for the stability test is taken to be the same as obtained from the coupling loss after cycling.

The WP1 conductor is designed to operate under different conditions than the ITER CS cable. To make an MQE simulation directly comparable to a simulation of the CS conductor and its calculated electric field threshold, the current and background magnetic field settings are selected such that a similar current sharing temperature and temperature margin are achieved. The applied magnetic field pulse is similar to the one used in the CSJA8 MQE simulations, see section 4.4.2. The background magnetic field is set to 11.7 T, the current at 60 kA and the calculated current sharing temperature is 8.5 K. In order to analyze the MQE anisotropy of the conductor the pulse is applied in both, parallel and perpendicular, directions.

The current distribution in the sample cross section at the center of the modeled conductor is shown in Figure 6.9.

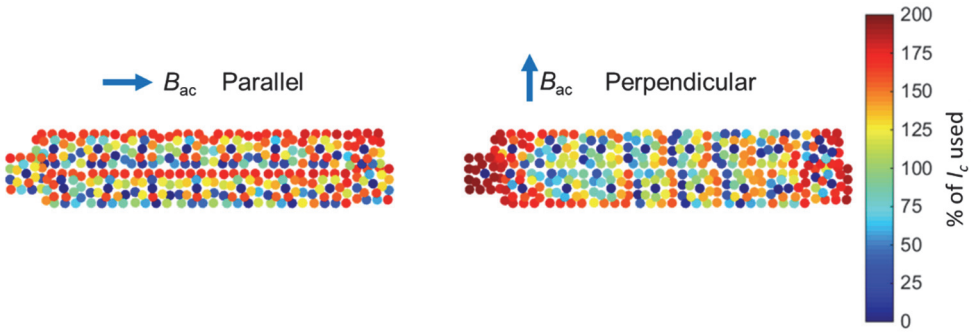

Figure 6.9 – Current distribution calculated for the WP1 MQE stability test in the conductor cross-section in the centre of the sample. The plots show the distribution of the current as ratio I_{str}/I_c (%) at maximum power. Coupling currents follow different paths depending on the magnetic field orientation. The applied magnetic field pulse in perpendicular orientation generates higher induced currents than in parallel configuration.

The model considers 400 mm of conductor, the same length as measured in the Twente facility. The current is represented as the percentage ratio of I_{str}/I_c. In both configurations, there are strands exceeding I_c but for the perpendicular AC field direction the current reaches the highest value. The current distribution inside the conductor is strongly different for both cases. In parallel configuration the current is more distributed over the cross section of the cable, while in perpendicular configuration there is a concentration of current at the edges of the conductor cross section causing locally very high electric field. Obviously, the geometry of the conductor is playing an important role for the stability. Consequently, if the magnetic field orientation along the windings of a coil is not carefully evaluated,

even a relatively small magnetic field perturbation in perpendicular direction may cause a stability issue.

To arrive at a more complete understanding of the conductor's behavior, the peak electric field calculated in the two configurations with different pulse duration periods is compared to those of the ITER CS Nb_3Sn conductor calculated with JackPot-THEA, see Figure 6.10.

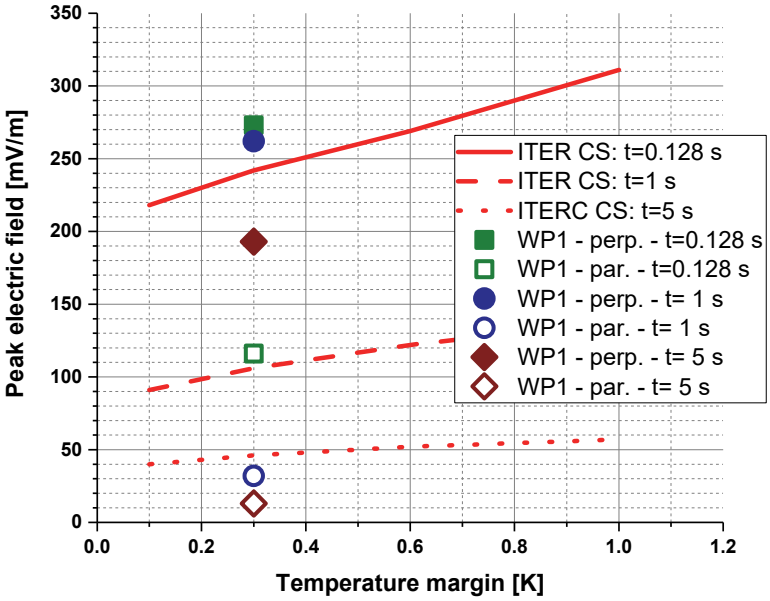

Figure 6.10 – Peak electric field as function of temperature margin. Comparison between the ITER CS type conductor and the WP1 sample in parallel and perpendicular applied pulsed field directions. The lines are the electric field threshold simulated for the ITER CS conductor. The full markers are the peak electric field in perpendicular direction while the open markers in parallel direction.

The peak electric field in parallel configuration of WP1 is significantly lower than the corresponding threshold of the ITER-CS for each pulse period. Therefore, the cable seems able to handle applied pulsed magnetic fields with higher peak value. On the other hand, in perpendicular configuration, the peak electric field exceeds the critical threshold found for the CS conductor study, suggesting that the cable will probably quench. It should be noted that the WP1 cable type was not subjected to MQE tests and therefore, it is not totally excluded that such a different cable pattern can lead to different quench behavior with a different peak electric field level.

6.3. Rectangular TF WP2 Conductor

The WP2 conductor was designed by ENEA, adopting the Wind & React technique. The design is derived from ITER conductors, but modified to obtain a rectangular shape. The cable is made of 6 petals twisted around a core of copper strands. Two of the petals contain a central spiral of steel serving as cooling channel with sub-cables twisted around them, while the other four are twisted around cores of copper wires, see Figure 6.11 [109].

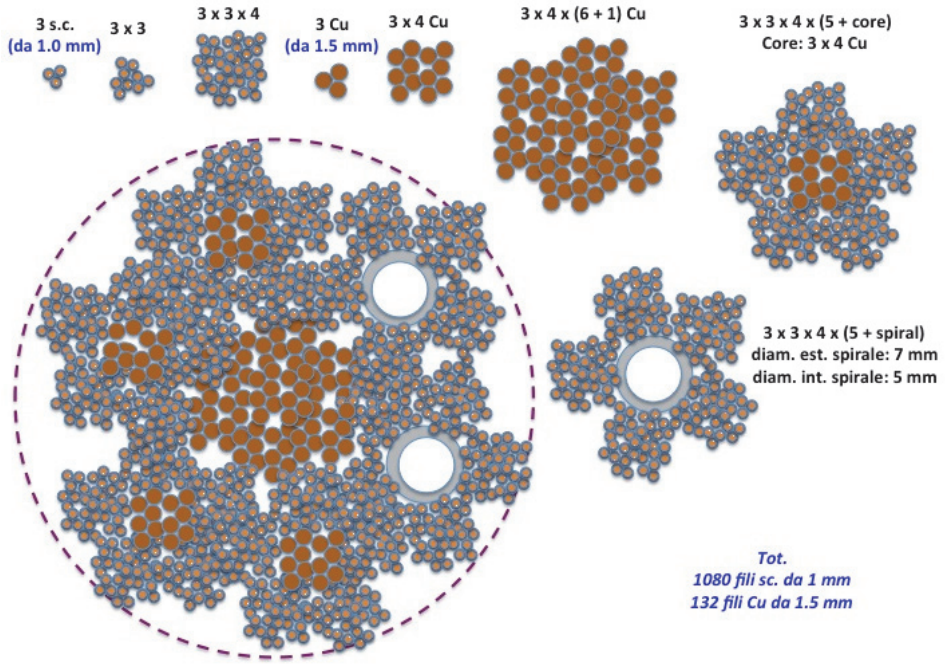

Figure 6.11 – Design of the WP2 – ENEA cable [109].

After jacketing, the cable is compacted towards a rectangular cross section reaching the target void fraction of ~25%. The cable was tested for AC loss at relatively low magnetic field and no transport current in both the EDIPO facility at SPC and in the University of Twente facilities. The cable geometry was reproduced using JackPot AC/DC, see Figure 6.12. The picture of the real conductor shows that the cable is not perfectly rectangular after the compaction.

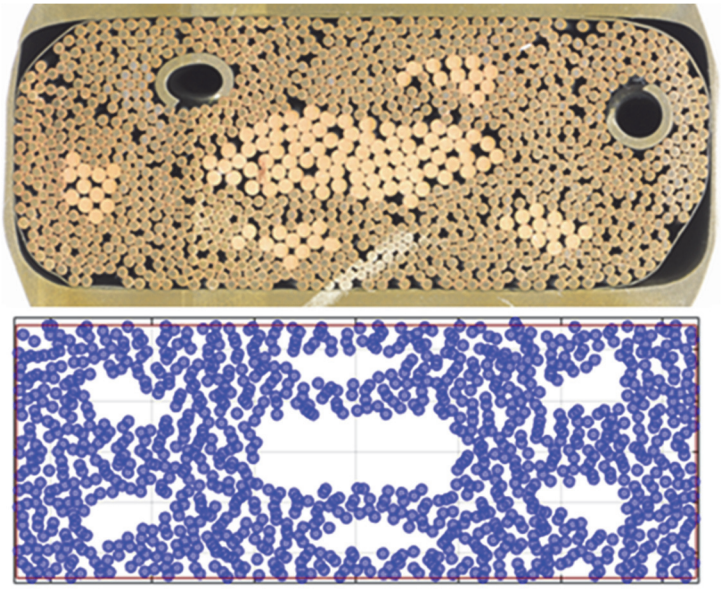

Figure 6.12 – WP2 sample tested at the University of Twente and the JackPot geometry used for the simulations. Only superconducting strands are plotted for the simulation (blue dots) [108].

The voids in the corners are difficult to reproduce with JackPot, where effort was made to distribute the strands more homogeneously in the available space. This void effect is caused by the cable wrapping in the real conductor, which mechanical role is not incorporated in the JackPot modeling. In Figure 6.13, the 3D geometry plot of the cable is presented.

The Nb_3Sn strands used in the WP2 sample is produced by WST (Western Superconducting Technologies, Xian, China) using the internal Sn technology and has a diameter of 1 mm [107], see Figure 6.14. The scaling law parameters for the critical current, following eq. (1.5), are summarized in Table 6.2 [105].

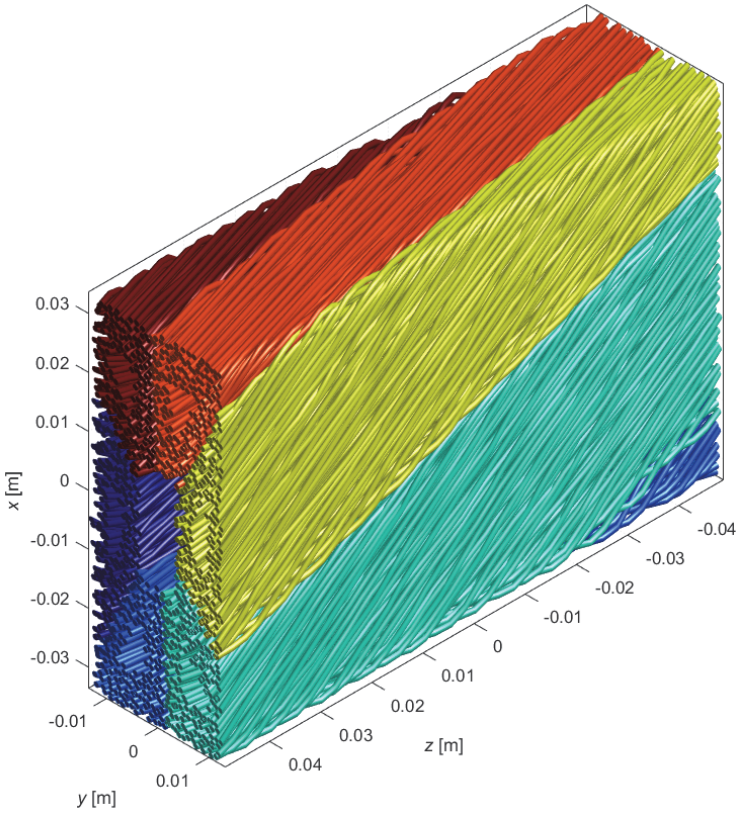

Figure 6.13 - 3D geometry of the WP2 conductor generated by JackPot AC/DC. Only superconducting strands are shown.

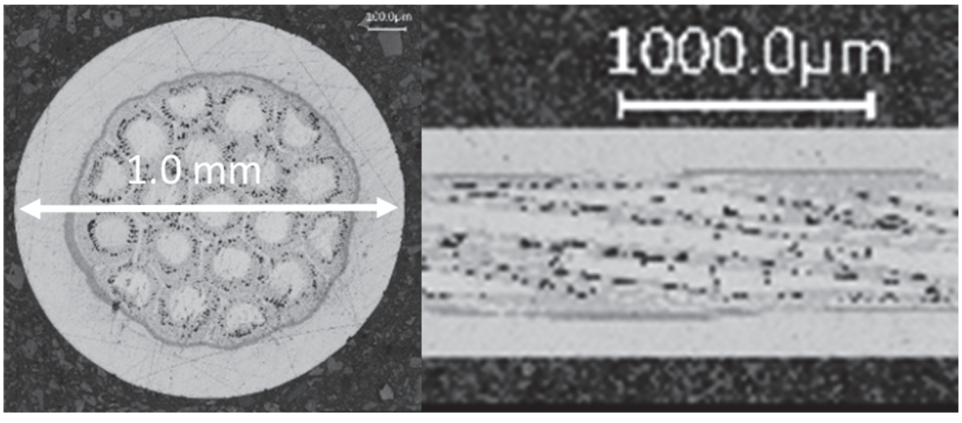

Figure 6.14 - WP2 Nb_3Sn strand cross section [106].

Table 6.2 – WP2 Nb_3Sn strand specification and parameters used for the JackPot modeling.

	WP2 - strand
Strand diameter [mm]	1.00 ± 0.05
Cu:non-Cu	1
RRR	>100
Critical current [A] at 4.22 K and 12 T	>350
B_{c20m}	33.24
T_{c0m}	16.34
C_{a1}	50.06
C_{a2}	0.00
ε_m *[%]*	-0.059
$\varepsilon_{0,a}$ *[%]*	0.312
ε_{appl} *[%]*	-0.21
p	0.593
q	2.16
C	73403
n_a	0.0
n_b	3.88
n_c	0.278

6.3.1. AC loss analysis

The AC loss measurements performed at the University of Twente and at the EDIPO facility [110] are used to validate the JackPot simulations of the WP2 conductor. As the WP1 sample, also WP2 is rectangular, thus the AC loss depends on the orientation of the magnetic field. In EDIPO, the background magnetic field is oriented perpendicular to the alternated magnetic field for the AC loss [111]. While, in the Press facility at the University of Twente both have the same direction. In addition, EDIPO and Twente use different values for the background magnetic field and the applied magnetic field pulse, which are 0.2 T and 0.15 T, respectively, see Figure 6.15.

In order to directly compare the results of Twente and EDIPO, it is necessary to apply a correction for the different AC magnetic field amplitudes. The coupling loss is proportional to the squared value of B_a, so the Twente data points, after the hysteresis loss subtraction, have to be multiplied by a factor $(B_{a_EDIPO}/B_{a_Twente})^2$, in

this case $(0.2/0.15)^2$, to make them comparable to the EDIPO's results. The analysis of the hysteresis loss for the EDIPO measurements is explained in the following section.

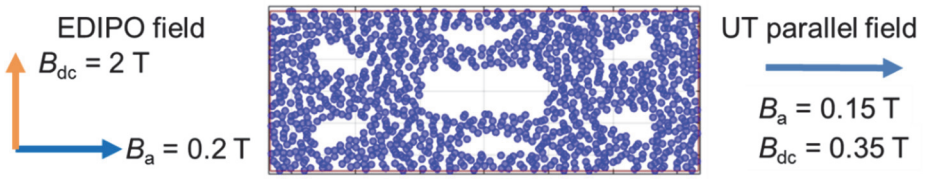

Figure 6.15 – Stationary field and AC magnetic field orientations and amplitude of the EDIPO and Twente facilities related to the cable WP2 sample cross section.

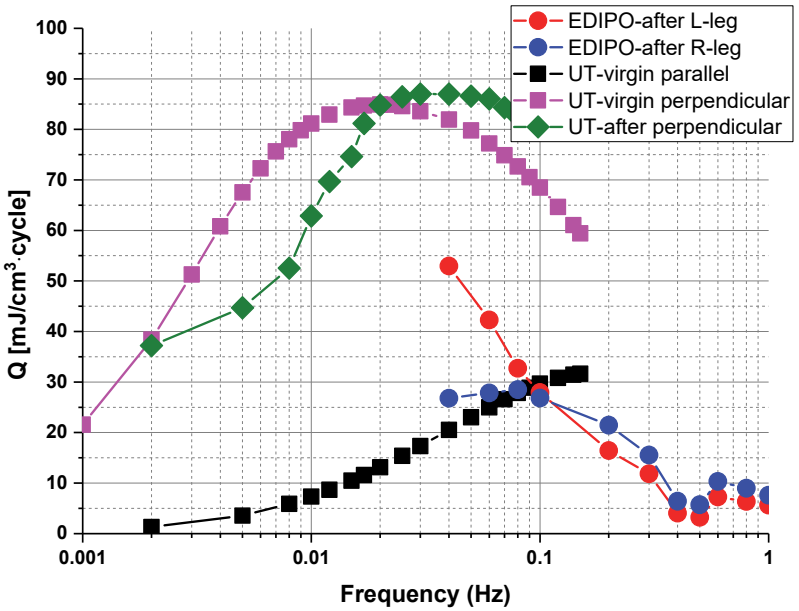

Figure 6.16 – Comparison between UT and EDIPO coupling loss measurement results for the WP2 conductor. UT data are scaled for applied field amplitude in order to compare them with EDIPO results.

The EDIPO frequency is in the range from 0.1 to 1 Hz and a more extended range from 0.04 to 1 Hz was explored after cycling. While at Twente, a range from 0.001 to 0.15 Hz is taken. Because of its wider range, only the EDIPO curves after cycling

are used in the comparison. The UT measurements are shown in both parallel and perpendicular configurations in virgin condition, while after cycling they are available only in perpendicular orientation. The measurements results attained at EDIPO and Twente are remarkably different, see Figure 6.16. For the EDIPO measurements, even the two legs differ considerably. The result is clearly not satisfactory, but the explanation for the difference between EDIPO and Twente results is not known. Further investigation is needed. In previous tests mostly of ITER conductors in general a rather good agreement was found between SULTAN, Twente Dipole and Twente Press AC loss results.

JackPot is used to reproduce both EDIPO and UT measurement results. Since the WP2 cable is quite demanding in terms of computation time for the JackPot solver, due to the large number of strands and the cable anisotropy, only the UT parallel and EDIPO configurations are modeled. Starting from the EDIPO coupling loss, the fit with the measurements is shown in Figure 6.17.

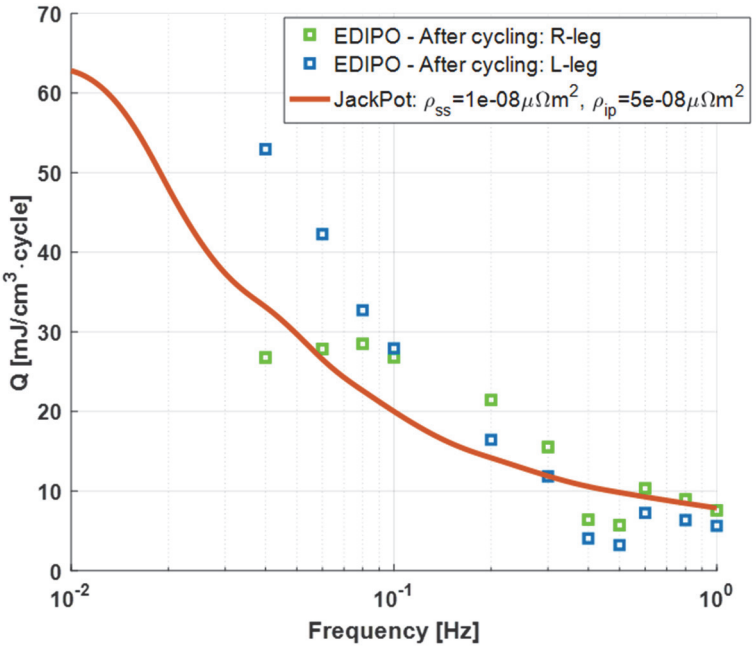

Figure 6.17 – WP2 conductor coupling loss versus frequency. The dots represent the data measured in EDIPO after cycling, the solid line is the best fit obtained with JackPot.

The JackPot simulation is not able to fit convincingly the experimental points and the resistivity required to fit the measurements is $\rho_{ss} \sim 10^{-8}\ \mu\Omega m^2$, two orders of magnitude lower than the resistivity usually applied in ITER Nb_3Sn conductors to find good fits, see Table 5.2.

The measured CS strand-to-strand contact resistance varies from $7.3\ n\Omega\mathrm{m}$ in virgin condition to $11.9\ n\Omega\mathrm{m}$ after cycling [112], while for WP2 the measured contact resistance starts at $3\ n\Omega\mathrm{m}$ in virgin condition increasing to $6.0\ n\Omega\mathrm{m}$ after cycling [108]. Therefore, the expected inter-strand resistivity for the WP2 sample should be two or three times lower than the usual CS inter-strand resistivity. Looking at the simulations, the inter-strand contact resistance for CSJA8 at 2 T is $\rho_{CSJA8} = 9 \cdot 10^{-6}\ \mu\Omega m^2$, thus the expected resistivity for the WP2 sample should be $3 \cdot 10^{-6}$ to $5 \cdot 10^{-6}\ \mu\Omega m^2$, two orders of magnitude larger than the values obtained with the simulation.

The large discrepancy between the EDIPO and the Twente coupling loss results combined with the anomalous JackPot resistivity necessary to fit the EDIPO measurements, strengthen the idea of some malfunction in the EDIPO facility results introduced during the measurements.

As for the WP1 conductor, also for the WP2 conductor, the inter-strand contact resistance and the AC coupling loss were measured in the Twente Press [108]. The contact resistance was measured in stationary condition between pairs of strands distributed over the cross-section of the conductor. The scheme of the selected strands is shown in Figure 6.18.

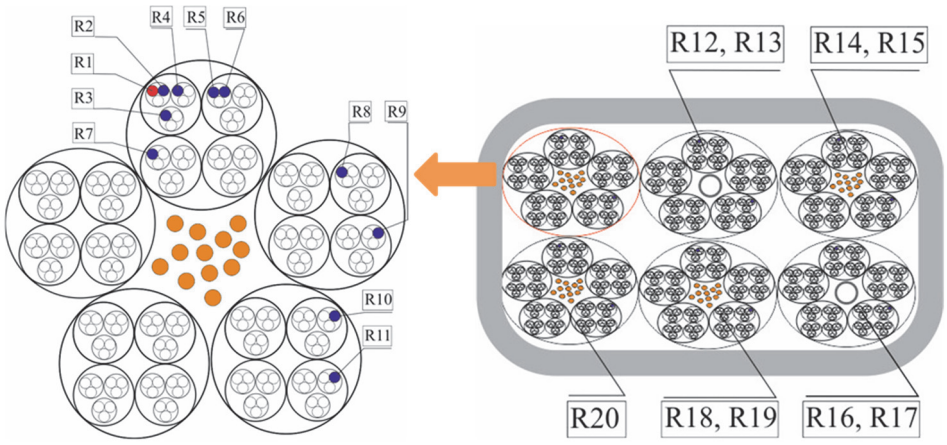

Figure 6.18 – Scheme of strand selection for contact resistance measurement on WP2 conductor sample [108].

A significant difference is observed between the contact resistance resulting from the EDIPO coupling loss and the contact resistance measurements performed at the University of Twente, see Figure 6.19.

The best agreement between Twente measured contact resistance and JackPot simulation is achieved with a resistivity in the range from 2 to $4 \cdot 10^{-6} \mu\Omega m^2$, see Figure 6.19. This resistivity value is in good agreement with the expected value based on the AC loss measurement and simulation. It is also important to mention that the absence of petal wraps allows the use of the same value of resistivity for both inter-strand and inter-petal contact resistances.

The three different resistances from Figure 6.19 are selected to simulate the coupling loss measured at the UT facility, see Figure 6.20. The best match is obtained using $\rho_{ss} = 3 \cdot 10^{-6}\ \mu\Omega m^2$. This value, satisfying both the experimental contact resistance and coupling loss measurements, is used for the stability analysis.

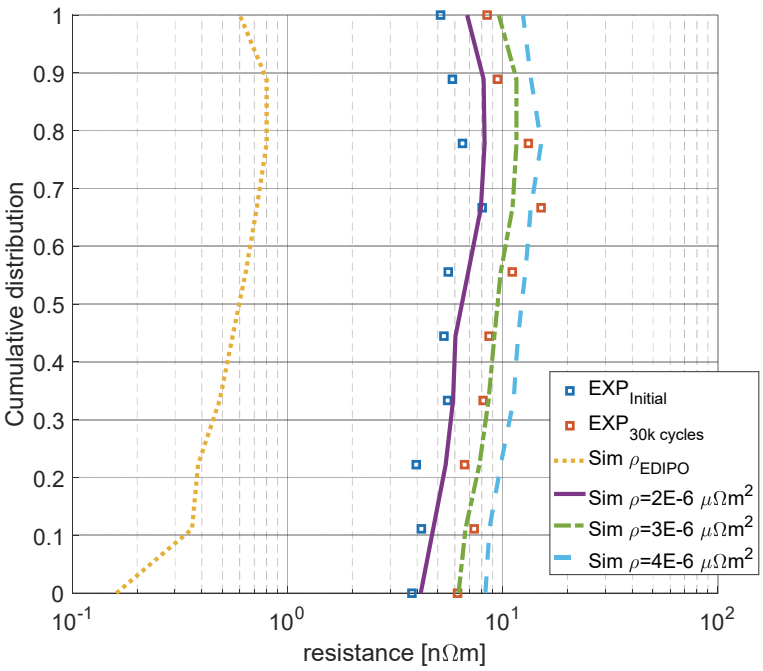

Figure 6.19 - Cumulative distribution of the inter-strand contact resistances in the WP2 sample. The markers represent the UT measured contact resistant measurements [108] in initial condition and after cycling. The lines represent the contact resistance used to fit the EDIPO coupling loss and the resistivity values used to fit the UT coupling loss data.

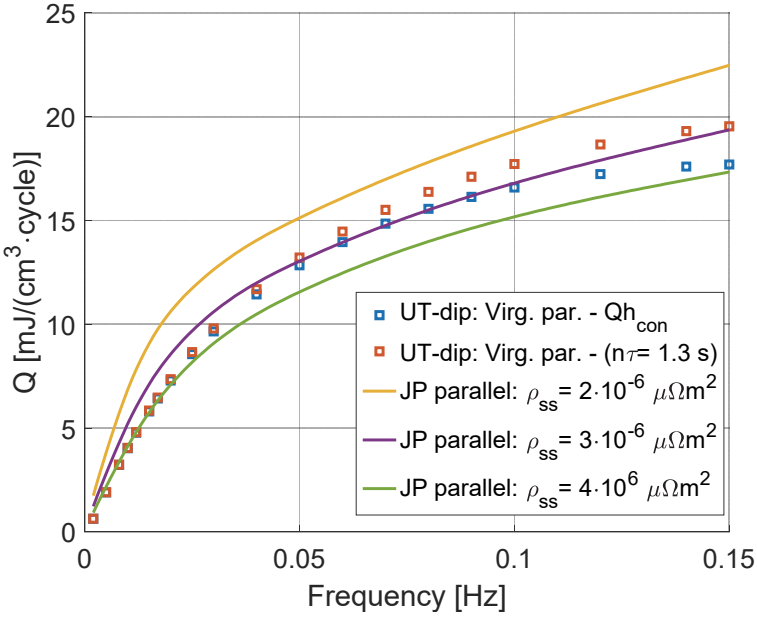

Figure 6.20 – Coupling loss as function of frequency of the WP2 sample calculated with JackPot (JP), the experimental points are from the University of Twente measurements performed in the dipole set up, B_{dc} = 0.35 T, B_a = 0.15 T and I_{op} = 0 A.

WP2 Hysteresis loss analysis of EDIPO measurements

The hysteresis loss can be directly estimated by fitting the initial slope of the total loss at low frequency. The loss defined by the fit at zero frequency is a good estimation of the hysteresis loss. The absence of the initial slope at low frequency in the EDIPO total loss does not allow a direct extrapolation of the hysteresis loss. The WST strand of 1.0 mm diameter used for the ENEA conductor has the same internal geometry as the ITER TF WST strand with 0.82 mm diameter [107]. Therefore, an estimate of the hysteresis loss of the WP2 sample can be derived from the ITER strand AC loss data. After reaching the full penetration of the magnetic field, the hysteresis loss depends linearly on the effective filament diameter [33]. Assuming that this remains valid for the physical dimension in terms of wire diameter, the hysteresis loss can be scaled from the ITER TF to the used DEMO TF WP2 strand.

For this purpose, the hysteresis loss is determined for the ITER samples with identification CNTF4 and CNTF5 having WST strand with similar layout as used in

the WP2 sample. The magnetic field levels used to test the AC loss of the samples in SULTAN are B_{dc} = 2 T and B_a = 0.3 T, while for the DEMO TF sample tested in EDIPO the values are B_{dc} = 2 T and B_a = 0.2 T. The hysteresis loss depends linearly on the applied magnetic field amplitudes when exceeding the penetration field. Therefore, after determining the hysteresis loss of the ITER TF samples, extrapolating to the expected DEMO TF sample hysteresis loss is straightforward. The hysteresis loss is calculated as follows:

a. The total loss after cycling of the CNTF4 and CNTF5 ITER samples is normalized to the volume of superconducting strand. The hysteresis loss at zero frequency is linearly extrapolated from the initial slope of the total loss as function of the frequency. The average value is $Q_{st} = 26.7\ mJ/cm^3 \cdot cycle$.

b. The hysteresis loss is then multiplied by a factor $(0.2/0.3)$, corresponding to the difference in applied magnetic field amplitude, see section 1.4.2.

c. Finally, the value obtained from the previous step is scaled multiplying it by a factor $(1/0.82)$, corresponding to the difference in strand diameter, from 0.82 mm to 1.00 mm. The hysteresis loss is assumed as first approximation linearly related to the strand diameter.

The final DEMO TF hysteresis loss is then obtained as $Q_{st} = 21.7\ mJ/cm^3 \cdot cycle$.

The measured total loss versus frequency of the WP2 sample rapidly decreases with frequency and saturates at about 0.3 Hz, towards about 10 mJ/cm^3·cycle. Usually the hysteresis loss is considered frequency independent, because the coupling loss becomes mostly dominant at high frequency. However in this case, when the hysteresis loss is subtracted from the total loss, the coupling loss becomes even negative, so this first order approximation is not valid (see Figure 6.21, red symbols).

In the late 1970's, Zenkevitch [113] studied the dependence of hysteresis loss and frequency on applied magnetic field. For an external field amplitude larger than the penetration field ($B_e > B_p$), as in this case, the ratio Q_h/Q_{st} is defined as:

$$\frac{Q_h}{Q_{st}} = (1 + \pi^2 \nu^2)^{-0.5}, \qquad \textbf{(6.1)}$$

where Q_h is the hysteresis loss and Q_{st} is the hysteresis loss at zero frequency. In the case of a generic perturbation B_e of duration τ, $\nu = \tau_0/\tau$, when the

perturbation has a sinusoidal shape, $\nu = \pi^{-1}\omega\tau_0$, where ω is the angular frequency and τ_0 is the coupling loss time constant of the conductor.

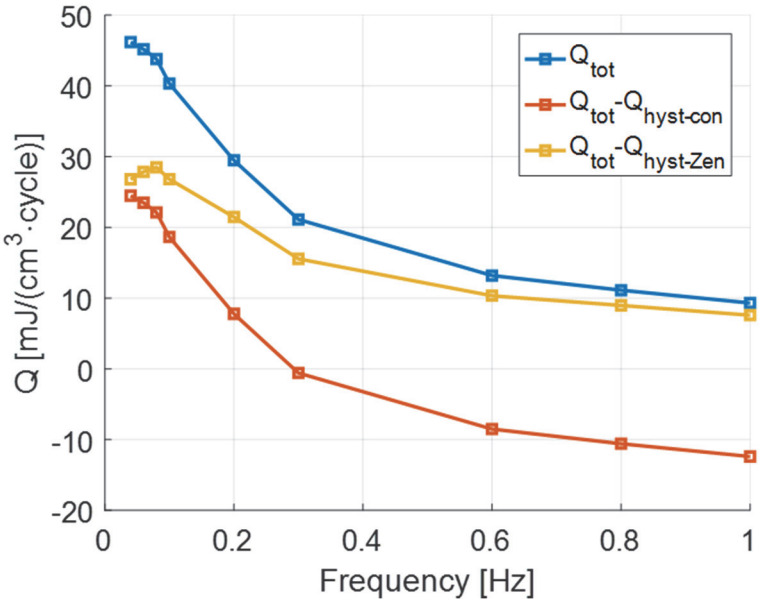

Figure 6.21 – Total and coupling losses versus frequency. The yellow curve is the coupling loss calculated using the Zenkevitch hysteresis loss correction from eq. (6.2). The red curve is the non-realistic coupling loss calculated using a constant value for the hysteresis loss.

Therefore for a sinusoidal perturbation, eq. (6.1) can be rewritten as:

$$\frac{Q_h}{Q_{st}} = (1 + \omega^2\tau_0^2)^{-0.5}. \tag{6.2}$$

The penetration field B_p for a Nb_3Sn strand can be expressed as [33]:

$$B_p = \frac{2\mu_0\alpha J_{nonCu} d_{eff}}{\pi}, \tag{6.3}$$

where α is the ratio between the total cross section area and the superconducting area of the strand, d_{eff} is the effective filament diameter, J_{nonCu} is the current density referred to the non-copper material and μ_0 is the magnetic permeability. The values for the variables α and d_{eff} are taken from [35] and the J_{nonCu} is calculated using the $J_c(B, T, \varepsilon)$ scaling law [27] with the strand parameters listed in Table 6.2. For a background field of 2 T, the penetration field is about 0.15 T and,

since $B_e > B_p$, eq. (6.2) can be applied. Using this approximation the derived coupling loss does not show negative values. Instead, it becomes almost constant at relatively high frequency as shown in Figure 6.21 (yellow symbols).

6.3.2. WP2 stability analysis

As for the WP1 conductor, also the WP2 conductor's low void fraction does not allow large changes in contact resistivity when applying high magnetic field and transport current. Therefore, the inter-strand resistivity used for the stability test is the one obtained from the UT measurement, $\rho = 3 \cdot 10^{-6}\ \mu\Omega m^2$. The WP2 conductor is designed to operate under different conditions than the ITER CS conductor, therefore, as for the WP1 sample, the current and background magnetic field were selected to achieve a T_{cs} similar to that of the ITER CS sample MQE tests. The background magnetic field is set to 11.8 T, the current is 80 kA and the calculated current sharing temperature is 8.5 K. In order to analyze the MQE anisotropy of the conductor, the magnetic field pulse is applied in two directions, parallel and perpendicular to the wide side of the conductor. To investigate the stability, different magnetic field pulses are applied to the WP2 conductor, using the peak value and pulse period simulated for the CSJA8 MQE tests, see section 4.4.2.

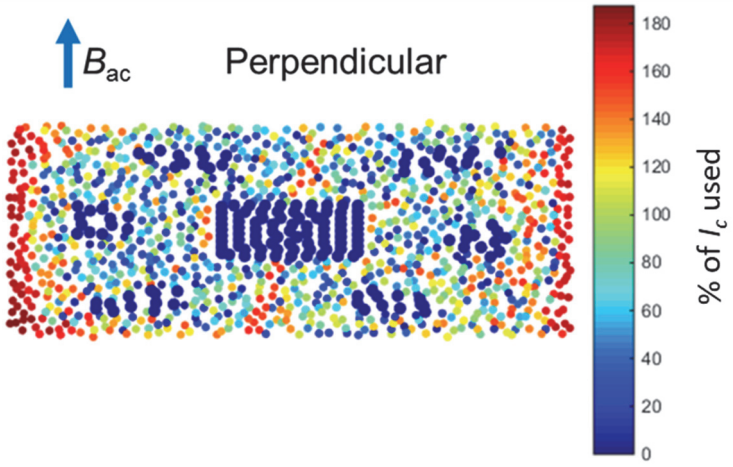

Figure 6.22 – Distribution of the strand's current ratio I_{str}/I_c (%) at the maximum peak power for the WP2 stability test. The applied pulsed field is in perpendicular direction and the cross-section of the conductor is taken in the middle of the sample.

The distribution of the ratio I_{str}/I_c along the conductor cross section in perpendicular configuration is shown in Figure 6.22. The strand currents are significantly higher at both short sides of the cable. The cross section shows the percentage of critical current flowing in the superconducting strands, the current carried by the copper strand is not displayed. The two cooling channels are substituted by ropes of copper strands in order to simplify the cable geometry in the model. Due to this difference the simulation result is probably underestimating the current carried by the superconductive strands due to the higher amount of segregated copper.

Looking at the same calculation conditions but then with parallel magnetic field orientation, see Figure 6.23, the current distribution is strongly different. The sample shows a high current along the petal boundaries and in the corners of the conductor cross-section. The current is accumulated in these regions, even if the inter-petal resistivity is equal to the inter-strand resistivity. This is probably related to the twist pitch pattern of the conductor and the low transverse resistivity, the current flows on the edges of the petals, creating an outer layer of saturated strands while inside the petals the current level is below I_c.

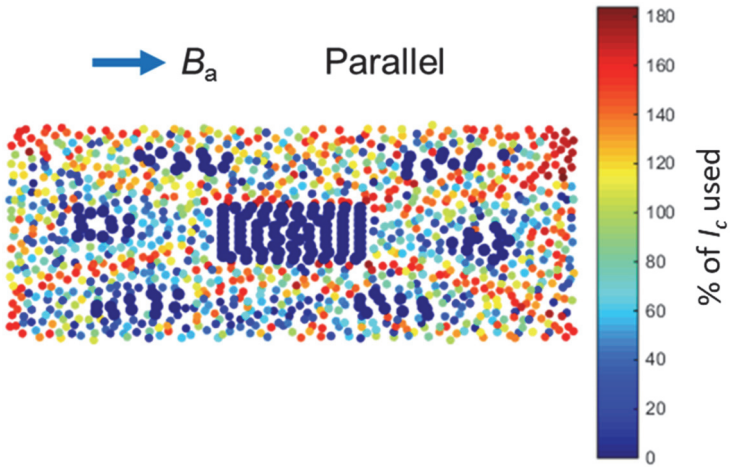

Figure 6.23 – Distribution of the strand's current ratio I_{str}/I_c (%) at the maximum peak power for the WP2 stability test. The applied pulsed field is in parallel direction and the cross-section of the conductor is taken in the middle of the sample.

The peak electric field during the magnetic field pulse is shown in Figure 6.24 as a function of the temperature margin. The peak electric field for fast pulse (t_{pulse} = 0.128 s) is lower than the threshold level for ITER CS type conductors, in both perpendicular and parallel configurations. While for longer pulse periods the WP2

peak electric field becomes about five times more, which is significantly higher than the ITER CS threshold. This phenomenon is directly related to the high coupling loss time constant of the conductor, $n\tau_{parallel}$ = 1.3 s and $n\tau_{perpendicular}$ = 35 s [108]. The low interstrand contact resistance and the absence of petals wraps cause an increase of the current decay time of the conductor at low frequency. The large coupling currents generated by the applied magnetic field pulse cause high electric field levels in the strands. Whereas at high frequency, the strands saturate generating a shielding effect, which limits the electric field peak. Therefore, this conductor design is likely less stable in the low frequency regime than ITER type CS conductors. Note that the CS conductors are obviously subjected to more severe pulsed conditions than TF conductors but for CS conductors with rectangular shape, the WP2 design is far from optimal.

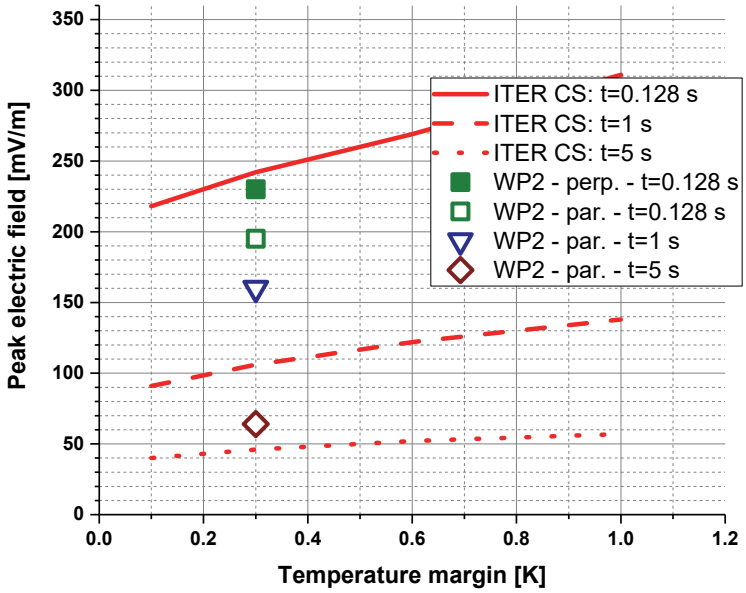

Figure 6.24 – Peak electric field as function of temperature margin. Comparison between the ITER CS type conductor and the WP2 sample in parallel and perpendicular applied pulsed field directions.

There are no results in perpendicular magnetic field for longer pulse, $t_{pulse} \geq 1$ s, because JackPot appeared instable for this condition with large magnetic field peak value and huge coupling currents leading to abnormal high electric fields. Anyway as for the WP1 sample, the WP2 cable also has higher peak electric field in perpendicular condition than in parallel configuration, due to the anisotropy of the

conductor design. Since in parallel field orientation the peak electric field of the WP2 conductor is already higher than the quench threshold of ITER CS conductor, the electric field is expected to be, also in perpendicular condition, far above the quench threshold.

In conclusion, the WP2 shows significantly lower stability margin compared to the ITER CS conductor at low frequency, which implicitly means less margin under plasma operating conditions and significantly higher risk of quench when this design would be used for the CS conductor.

Considering the magnetic field pulse direction, the difference between the peak electric field in WP2 conductor is less than the difference for the WP1 conductor, see Figure 6.24 and Figure 6.10, respectively. This can be explained by the different cable pattern, void fraction and cable's aspect ratios. The cable pattern is completely different: Rutherford-like for WP1 and ITER-like for WP2. The ratio between long and short sides of the cable cross-section is about 2.5 in the WP2 cable, while in the case of WP1 conductor the ratio is about 5. The WP1 conductor has the strongest anisotropy that corresponds to the biggest difference between the simulated peak electric fields depending on the magnetic field orientation, compared to the WP2 conductor. The effect of the anisotropy on the conductor stability has to be taken into account in the coil design. The direction of the applied magnetic field plays an important role in the conductor stability behavior together with the inter-strand contact resistance, which on its turn depends on the void fraction and presence of petal wraps.

The performance of the different conductors can also be affected by the strand diameter, which is different in the DEMO conductors and on their turn also different from ITER conductor strands. The strands used in DEMO WP1 and WP2 conductors have a larger diameter than ITER strands, which results into a lower number of strands in the conductors. This will affect the mechanism of current redistribution, coupling loss, strand saturation and peak electric field.

The next section is dedicated to a simplified numerical study investigating the effect of the strand diameter on the stability of CIC Conductors.

6.4. Strand diameter effect study

Three different types of CIC Conductors (ITER CS, DEMO TF WP1 and WP2) were analyzed with every conductor having a different cable pattern, number of cabling

stages, strand diameter and void fraction. In order to study only the effect of the strand diameter on the conductor performance, it is necessary to adopt three conductor configurations with minimum differences with respect to other properties. As baseline design, the ITER CS conductor cable pattern is chosen, because the circular cross section minimizes the radial anisotropy regarding applied magnetic field and its associated current distribution. The other two cables with different strand diameters are scaled to have similar void fraction, superconductor cross sectional area and cable pattern. In Table 6.3, the strand geometry properties are listed.

Table 6.3 – Geometrical properties of the three different strands. The ratio between the different cross sections is used to adapt the scaling law for different diameter.

	Strand 1	***Strand 2***	***Strand 3***
Diameter [mm]	0.83	1.00	1.50
Area [mm^2]	0.54	0.79	1.77
Ratio scaling law (StrX/Str1)	1.00	1.45	3.27

Table 6.4 – Cables pattern, twist pitches, void fraction and cable dimensions of the three conductor types.

	Cable 1	***Cable 2***	***Cable 3***	***Twist pitch [mm]***
Stage 1	3(1Cu)	2	-	45
Stage 2 [x3]	9	6(2Cu)	3(1Cu)	85
Stage 3 [x4]	36	24	12	145
Stage 4 [x4]	144	96	48	250
Stage 5 [x6]	864	576	288	450
Equivalent strand surface [mm^2]	467	452	509	
Void fraction [%]	33	33	33	
r_{in} [mm]	6	6	6	
r_{out} [mm]	16.05	15.85	16.65	

The strand scaling law parameters are the same as used for the CSJA8 KAT strand [87], see Table 4.2, and the I_c is linearly scaled to the different diameters. The use of only one scaling law is again to minimize the differences between the cables.

In Table 6.4 the cable patterns of the samples are listed, the twist pitches for corresponding cable stages are the same for all conductors. The r_{in} is fixed, while r_{out} is adjusted to maintain the same void fraction while respecting the equivalent strand cross sectional area ratio. The cross section of the three cables is shown in Figure 6.25, where blue dots represent superconducting strands and red dots copper strands.

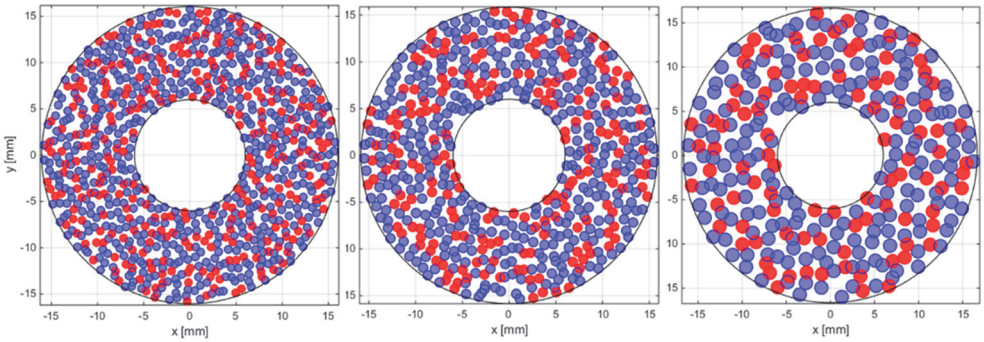

Figure 6.25 – Cable cross sections of the three different designs used for the strand diameter effect study. From left to right Cable 1 (d_{str} = 0.83 mm), Cable 2 (d_{str} = 1.00 mm) and Cable 3 (d_{str} = 1.50 mm).

6.4.1. Coupling loss

The coupling loss of the three conductors is simulated with JackPot AC/DC, using the same inter-strand resistivity for all samples. The contact resistivity is taken from the CSJA8 sample ($\rho_{ss} = 4 \cdot 10^{-6}$ $\mu\Omega m^2$). The same test conditions, as used in the SULTAN experiments, are applied to all samples, B_{dc} = 2 T, B_a = 0.2 T, I_{op} = 0 kA, f = 0.1 to 1 Hz.

The simulated coupling loss results are shown in Figure 6.26. The cable with highest coupling loss is Cable 1 (d_{str} = 0.83 mm). This is probably due to the higher number of contacts between superconducting strands, leading to a larger number of loops with strands linked through strand-to-strand contacts. However, Cable 2 has lower loss than Cable 3, which is probably caused by the slightly different cable pattern. The first stage is made with only two superconducting strands and the copper strands are added in the second stage, thereby changing the strand distribution inside the cable. In the cable cross section of Cable 2, the strand distribution is less homogeneous than for both other designs. There are some areas where only copper or only superconductive strands are grouped together, see Figure 6.25. This

illustrates the importance of the contact distribution among strands and the influence that it can have on the coupling current loss.

From the coupling loss analysis at low magnetic field and without current, the simulations show that a higher number of strands corresponds to more contacts and as a consequence higher coupling loss for similar cable concepts (same twist pitches, cabling stages, inter-strand resistivity, etc.).

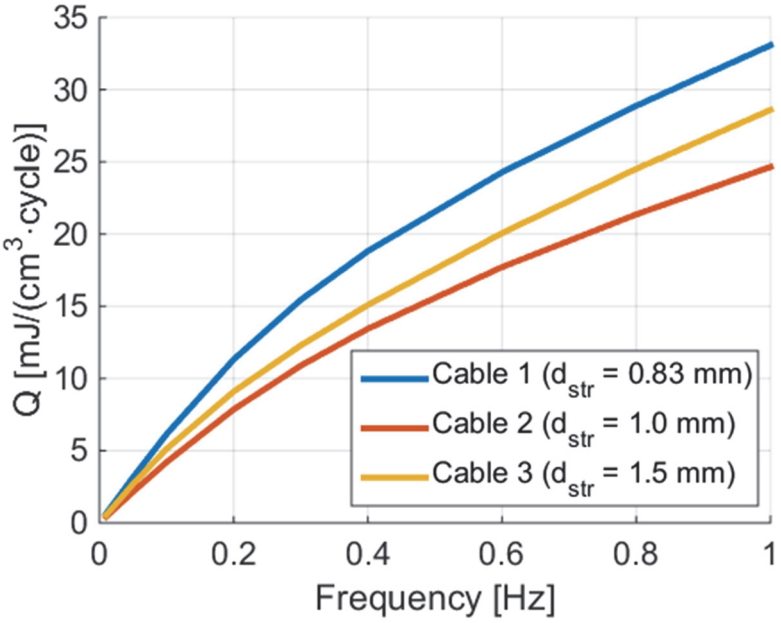

Figure 6.26 – Coupling loss as function of frequency simulated for the three different cable designs. The coupling loss is calculated at 2 T background magnetic field and zero transport current.

6.4.2. Stability analysis

The stability analysis is performed for the three cables in order to evaluate the relation between strand diameter and stability performance. The simulations replicate the SULTAN stability tests. A sinusoidal magnetic field pulse is applied to the conductor in the presence of a background magnetic field, transport current and relatively high temperature. To reduce the calculation time, only one magnetic field pulse per pulse period is used and not the MQE pulse amplitude. The conductors are tested and the results compared under similar critical conditions with the aim to generate relevant high electric fields in the sample. The test conditions are chosen such to have the same T_{cs} for the three conductors, see Table

6.5. The transport current is used as free parameter to set the same T_{cs} for the three different designs.

Table 6.5 – Conductor test conditions and T_{cs}.

	Cable 1	***Cable 2***	***Cable 3***
B_{dc} *[T]*	9.7	9.7	9.7
t_{pulse} *[s]*		0.128 – 1 – 5	
I_{op} *[kA]*	40	39	42.5
T_{cs} *[K]*	8.7	8.7	8.7

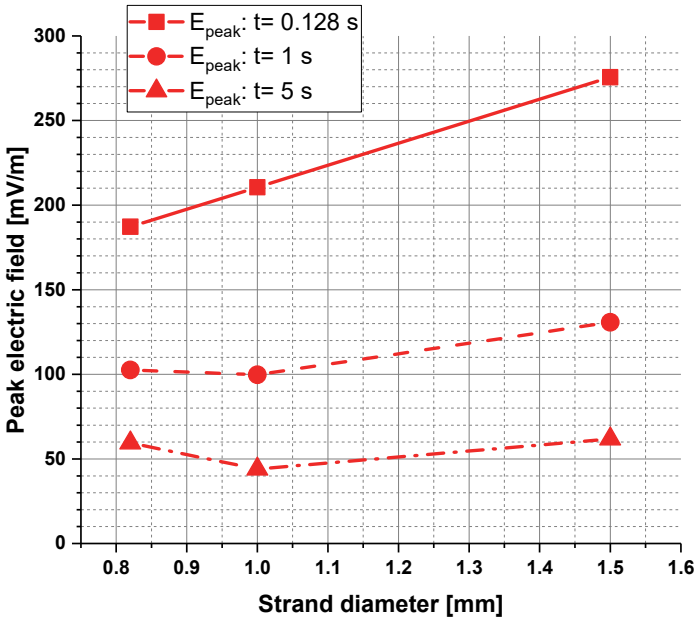

Figure 6.27 – Peak electric field as function of strand diameter for three different sinewave magnetic pulses of 0.128, 1 and 5 second.

The same single magnetic field sine wave pulse is applied to the three cables and the peak electric field for each one is calculated. Also the same pulse periods are used as previously in order to analyze the peak electric fields for different frequency regimes. In Figure 6.27, the calculated peak electric fields are shown as a function of the strand diameter. Cable 3 has the highest electric field. The peak electric field difference between the cables decreases with the increase of the pulse period. Cable 2 has a faster drop of peak electric field compared to the other two samples.

This phenomenon is probably related to the cable pattern as already observed in the coupling loss analysis.

The analysis of the peak electric field suggests that it can be preferable to have a higher number of strands with smaller diameter in order to improve the conductor's stability during fast transients, but it becomes less relevant with longer magnetic field pulse. A higher number of strands corresponds to less current per strand, easier redistribution and recovery during the magnetic field pulse. From the thermal point of view, considering cables with the same cross-sectional area, more strands also means larger strand wetted perimeter in contact with the coolant, which increases the heat removal capacity from the strand. It is necessary to underline that the peak electric field necessary to quench the strands can vary depending on the strand diameter and the strand internal design, implying that it is necessary to evaluate carefully the strand performance in order to choose the best conductor design.

6.5. Conclusion

The two experimental DEMO CIC Conductors called WP1 and WP2 are modeled using JackPot AC/DC for evaluation of coupling and hysteresis loss and pulsed field stability.

The coupling loss results show that the rectangular geometry causes a different coupling loss depending on the magnetic field orientation and conductor aspect ratio. This behavior is reflected in the stability performance of the conductors as well. The magnetic field perturbations in the perpendicular direction can generate high electric field leading to a quench, while in the parallel direction, with the same pulse peak value, the conductor is able to recover. In order to use a rectangular geometry, it is necessary to carefully evaluate the possible magnetic field fluctuations and their directions in order to avoid stability issues under normal operating conditions.

The absence of petal wraps allows a better current redistribution and more homogeneous compaction for rectangular conductors. However, in combination with a smaller void fraction, rectangular conductors are more prone to instability, in particular when subjected to magnetic field perturbations oriented perpendicular to the wide side.

The anisotropy of the rectangular WP2 ITER like conductor is less than of the rectangular WP1 Rutherford type conductor. The JackPot generated geometry has some minor differences in the strands distribution compared to the real cable cross section, but the model is well able to reproduce the Twente Press coupling loss measurement results. The model can also find a match to the EDIPO measurement results, but the assumed inter-strand contact resistivity necessary to achieve the fit, is two orders of magnitude lower than measured in the Twente Press. The issue with the EDIPO measurements is not yet explained and the test have to be repeated in order to make a better assessment.

The results of the stability analysis reflect the conductor's anisotropy. The difference in the peak electric field depending on the magnetic field pulse direction is obviously less for the WP2 than for the WP1 conductor.

The strand diameter and the number of strands in the conductor also play a role in the stability although the effect is rather limited. For comparable transport properties, a smaller strand diameter and thus a larger number of strands, leads to lower peak electric field and consequently to a better stability performance.

7. CONCLUSION

The electromagnetic and thermal critical stability behavior of Cable-in-Conduit Conductors for fusion is investigated by defining an electric field threshold for quench initiation and analyzing the conductor performance during plasma operating conditions.

The conductor tests conditions performed so far on short conductor samples cannot reproduce the real operating plasma scenario conditions. Therefore, the present experiments in the available test facility are not sufficient for validating in full the operation capacity of the superconducting CIC-Conductors for ITER-like fusion magnets. At present, only simulation models can be used to approximate the true operational condition and to predict the behavior of CICCs under plasma operating conditions. JackPot AC/DC and MPAS simulation models are used to study the coupling and eddy current losses generated in NbTi and Nb_3Sn based CIC-Conductors. Subsequently, they were combined with the THEA model to study the thermal behavior of the cables under quench and plasma operating conditions as well.

The MPAS analytical model can reproduce accurately the experimental coupling loss of NbTi and Nb_3Sn based CIC-Conductors. The combination THEA and MPAS is able to predict the SULTAN stability test results of the ITER PFEU2 NbTi sample within 10%. The heat deposition profile, i.e. the energy generated by the magnetic field pulse applied to the conductor under test, plays a key role in the quench initiation. It is shown that the minimum quench energy depends directly on the heat deposition profile. Therefore, the operating scenario in terms of magnetic field variations in time or more in general, any variation in the magnetic field perturbation applied to the conductor have to be considered with caution regarding conductor stability.

The MPAS model is calibrated using a relevant coupling loss measurement of a representative conductor. During the quench stability measurements of Nb_3Sn CIC-Conductors the test conditions are largely different from the AC loss test conditions. The main difference is in temperature, magnetic field pulse period and magnetic field peak value applied to the conductor. Obviously, the accuracy of MPAS declines when the test conditions become substantially different from the calibrating conditions. Therefore, the model loses its validity when simulating the stability test of the Nb_3Sn CIC-Conductors, where the applied magnetic field pulses deviate strongly from the calibration conditions.

JackPot AC/DC is a numerical conductor simulations model that is able to calculate accurately the trajectories of all strands in a full-size CICC and simulates the transport, coupling and eddy currents and its losses by solving the equivalent electric circuit. The only free parameters in the model are the inter-strand resistivity and the axial strain present in the strands. The inter-strand resistivity can be defined directly using the contact resistance measurement method performed at the University of Twente, or indirectly, by fitting the coupling and eddy current losses measured at the SULTAN facility.

The effective axial strain is determined from the current sharing temperature measurements performed at the SULTAN facility. Once calibrated, JackPot can simulate the energy deposited inside a cable for any, time dependent, applied magnetic field, current and temperature. The model is capable of reproducing the SULTAN short sample tests for both the NbTi and Nb_3Sn CIC-Conductors investigated. Differently from MPAS, JackPot can reproduce correctly the stability test performed on Nb_3Sn CIC-Conductors at the SULTAN facility. It can also estimate the current sharing temperature. However, it is not suitable to simulate the normal zone propagation after quench. Therefore, JackPot is not able to define the minimum quench energy of Nb_3Sn CIC-Conductors, because they can reach temperatures above the current sharing temperature before quench occurs. When combining THEA with JackPot, it is possible to model the electromagnetic and thermal behavior of CIC-Conductors in the relevant range of operating parameters. The combination JackPot-THEA reproduces the SULTAN MQE experiment for the ITER CSJA8 sample within 10%.

After validating JackPot-THEA with SULTAN quench measurements, the stability study is extended to magnetic field perturbations with lower ramp rates and higher peak values, more relevant for fusion magnets and Central Solenoid conductors in particular. The results show a dependency of the Minimum Quench Energy on the sinusoidal-like magnetic field pulse period. Increasing the sinusoidal magnetic field pulse period, the magnetic field ramp rate decreases and as consequence the deposited heat is reduced. At the same time, the increased magnetic field period allows the coolant to extract more heat from the conductor. As a result, the Minimum Quench Energy increases with the increment of the sinusoidal pulse period. It is concluded that the conductor is less stable when it is subjected to faster heat deposition.

Based on the stability simulation results using different pulse periods and peak values, JackPot is able to calculate the critical electric field, which can then be used as a threshold for initiating a quench. The determined peak and average electric

field thresholds are significantly higher than the average quench electric field measured at SULTAN in stationary condition. However, it is found that the average electric field threshold asymptotically approaches the experimental steady-state critical electric field when increasing the magnetic field pulse period. This result shows the remarkable effectiveness of the JackPot-THEA combination.

The definition of an electric field threshold for the stability performance of the CIC Conductors supported by the validated electromagnetic and thermal combined JackPot-THEA model enables to compare quantitatively short sample stability tests results and expected conductor performance under actual ITER plasma operating conditions.

The so-called ITER 15 MA plasma scenario determining the most demanding excitation of the Central Solenoid is analyzed from both thermal and electromagnetic points of view using the JackPot-THEA model. The peak and average electric fields generated in the most inner and critical turn of the Central Solenoid coil after the Start of the Discharge are compared to the electric field thresholds found in the preceding analysis. The Central Solenoid conductor electric fields found for the most severe plasma operating conditions are one order of magnitude below the critical threshold. At the same time, the average electric field after the Start of the Discharge is below the critical electric field measured under stationary condition. Moreover, the JackPot-THEA simulation of one layer of the so-called quadra-pancake of the CSU2 module provides the temperature profile reached along the conductor. The peak temperature is located in the most inner turn of the pancake and it reached a maximum of 5.7 K. In addition, the simulation describes the flow of the heat slug through the 150 m conductor of the pancake layer. At the end of the plasma cycle, the conductor is cooled down to the initial helium inlet temperature. Therefore, considering the defined electric field criteria, the ITER Central Solenoid does not show stability issues. On the contrary, the model convincingly confirms the ability of the Central Solenoid conductor and thus the coil for continuous cycling of the 15 MA plasma scenario burn cycles.

When completed the analysis of the ITER conductors stability, the JackPot simulations were extended to new fusion conductor designs for future reactors like DEMO. Two R&D samples of demonstration CICC-Conductors, designed by the Swiss Plasma Center and ENEA, respectively, were analyzed. Differently from ITER conductors, the conductor cross sectional layout is rectangular. The new geometries were reproduced using JackPot and calibrated using coupling loss and contact resistance measurements performed at the University of Twente. The observed agreement between simulation and experiment illustrates the capability

of JackPot to calculate the correct coupling loss even with cable designs significantly different from the ITER-type CICCs.

The electric field stability threshold, determined and evaluated for the ITER Central Solenoid conductor, was used to analyze the stability of the proposed DEMO conductors. The effect of the anisotropy of the conductors' rectangular shape is evident in the coupling loss results and in the stability performance. Magnetic field perturbations in the perpendicular direction generate a higher loss than in the parallel direction. Therefore, the stability of the conductor is anisotropic and varies with the magnetic field orientation. The rectangular design, however, is beneficial regarding conductor stability for applied field in parallel direction, to the detriment of the other orientation. Therefore, the rectangular geometry can be effective in improving conductor and thus magnet stability, although the magnetic field direction needs to be considered for all positions in the coil cross section, also at the edges of the coils where the magnetic field direction deviates significantly.

The performance of a Cable in Conduit type of Conductor is influenced by many factors like cable patterns, local void fraction, presence of petal wraps, use of segregated copper and strand diameter. With the numerical model JackPot, it is now possible to isolate a single factor and to perform a parametric study of its influence on the conductor behavior. The ITER CS conductor and the DEMO TF prototypes studied here comprise three strands with different diameter. To isolate and study only the influence of the strand diameter, three dedicated cable designs were created. The cable geometry is chosen with the aim to make the coupling loss variation only dependent on the strand diameter, thereby minimizing the influence of other factors. The coupling loss and stability tests of the three CIC Conductors were simulated using JackPot. The model shows that a smaller strand diameter and a higher number of strands in a conductor, corresponds to a lower peak electric field during the pulsed field stability tests. Although the impact is marginal, a larger number of strands corresponds to a higher number of contacts among them, a more homogeneous distribution of electrical properties and consequently can increase the current redistribution capability, and thus improve conductor stability.

The work presented here illustrates the tools and the next steps in Stability Simulations of Cable in Conduit Conductors. The electromagnetic analysis at strand level, combined with the thermal behavior of the conductor, provides a new and very powerful method for designing conductors for next generation magnets for fusion.

Although the research for the truly first fusion power plant is still far to be completed, I hope this work provides an effective contribution to the final achievement.

7. Conclusion

A. ENERGY CALCULATION OF SULTAN STABILITY TESTS

A.1. Introduction

The stability tests are performed to find the Minimum Quench Energy (MQE) of the conductor. The tests are carried out in the presence of transport current and background magnetic field. The energy to induce a quench is injected by a fast magnetic field pulse of the AC coil. Different from the AC loss measurements, the energy is deposited using a single sinusoidal magnetic field wave.

To realize a singular sinusoidal wave, a capacitor bank with 10 capacitors of 4 mF each, is connected to the AC coils in order to build an RLC circuit with 7.8 Hz resonating frequency (128 ms of time period) [58]. The capacitor discharge generates a sinusoidal magnetic field that can be cut either after one or half period. To reach the MQE, the amplitude of the pulse is stepwise increased until the quench occurs.

The calculation of the deposited energy is based on [80]. It is determined considering the helium temperature difference, measured between upstream and downstream sensors and by using the mass-flow rate and the helium specific heat, see eq. (3.1).

For NbTi conductors, the energy calculated using the methodology described in [68] was in good agreement with the results obtained using eq. (3.1), whereas in this case the temperatures, measured during the tests of the CSJA8 sample, show a large fluctuation. Therefore, the method described in [68] cannot be used and it is necessary to modify the analysis strategy in order to accurately calculate the deposited energy.

A.2. Minimization of the temperature fluctuation

During the stability tests of the sample CSJA8, the temperature readings show large fluctuations, as shown in Figure A.1, where the measured temperatures of test run #CSJA8Q011206 are shown. The test conditions are B_{DC} = 9 T, I_{op} = 40 kA, T_{in} = 8.1 K and the battery voltage is 340 V, which is equivalent to an applied magnetic field pulse B_a of 0.43 T.

As explained in section 2.2.1, the sample temperature sensors are located upstream and downstream the High Field Zone (HFZ), see Figure 2.1. Four sensors are attached to the jacket at each location and the axial distance between the sensors is 0.8 m. The temperature sensors are commercial zirconium oxynitride films (Cernox) [114]. The manufacturer calibrateed all Cernox sensors with an accuracy of ±5 mK. An evaluation of the precision and reproducibility of the current sources as well as potential thermal voltages, led to the conclusion that the absolute error of the temperature readings is typically ±30 mK [115].

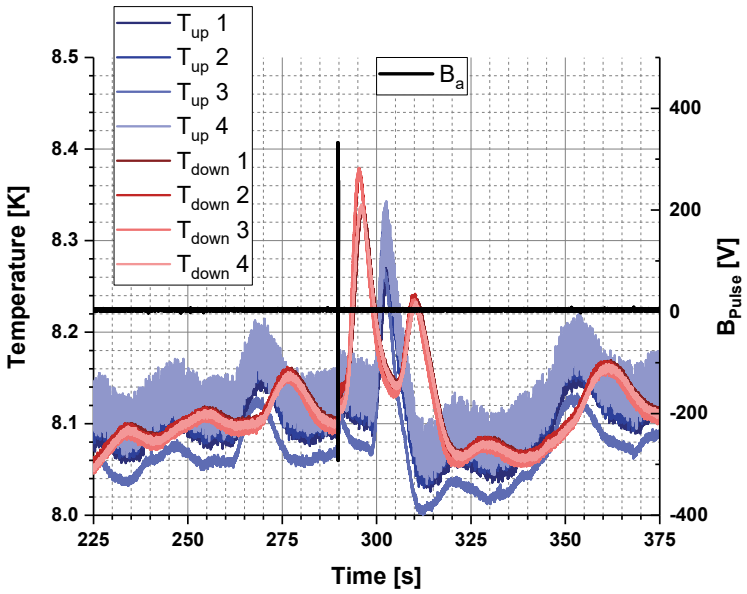

Figure A.1 – Temperature measured during test run #CSJA8Q011206 as function of time. In blue, the temperatures measured upstream the high field zone (T_{up}) while the temperatures measured downstream (T_{down}) are given in red. The battery voltage used to generate the pulse magnetic field as function of time is in black.

Following [68], the upstream and downstream temperatures are averaged before calculating the conductor temperature variation generated by the applied magnetic field pulse. The average temperatures are shown in Figure A.2. When excluding the peaks generated by the magnetic field pulse, the temperature profiles are both subjected to a fluctuation of ±0.1 K. The average temperatures show a clear phase shift between upstream and downstream temperature fluctuations. Due to this shift, it does not make sense to calculate the conductor temperature variation

directly subtracting the two curves as shown in Figure A.3. The calculated ΔT still has a continuous fluctuation and the increase of temperature due to the applied field pulse is partially hidden in the fluctuation. Therefore in the presence of such temperature fluctuations, the assumptions of [68] are not valid anymore and some improvements are needed.

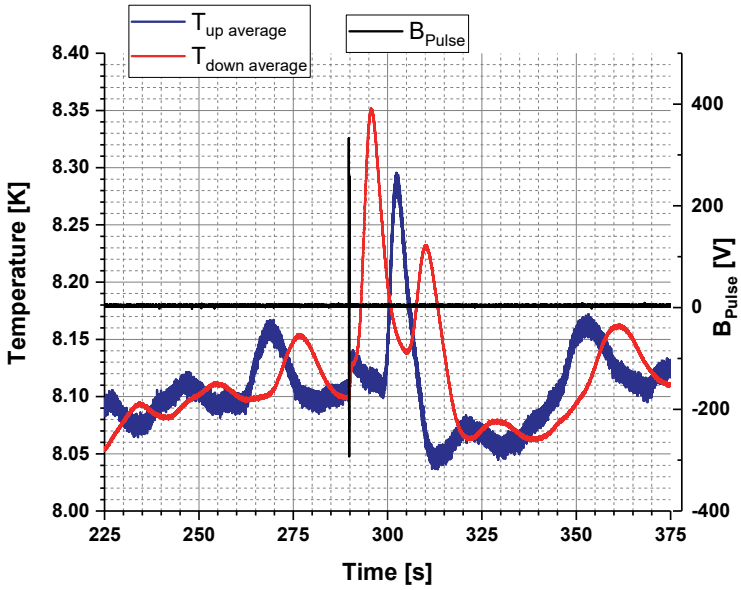

Figure A.2 – Temperature measured during test run #CSJA8Q011206 as function of time. In blue, the average upstream temperature (T_{up}) while the temperatures measured downstream the high field zone (T_{down}) is in red. The battery voltage used to generate the pulse magnetic field is in black.

As shown in Figure A.2, the helium temperature is subjected to local fluctuations, which seem to propagate through the conductor at a speed determined by the helium mass flow. Moreover, the temperature profile at T_{down} is basically similar to the one observed at T_{up}, which signifies that the temperature profile present at T_{up} propagates as a bias slug towards T_{down}.

In order to cancel out the effect of the strong helium temperature fluctuation, it is necessary to apply a time shift to the upstream temperature before subtracting the average temperatures. The time delay is t_{offset} = 7.5 ± 0.3 s and is determined empirically and defined as the time difference between the measured temperature peaks, see Figure A.4. The effective velocity of the helium in the bundle, calculated from t_{offset} is v_{eff} = 0.11 m/s.

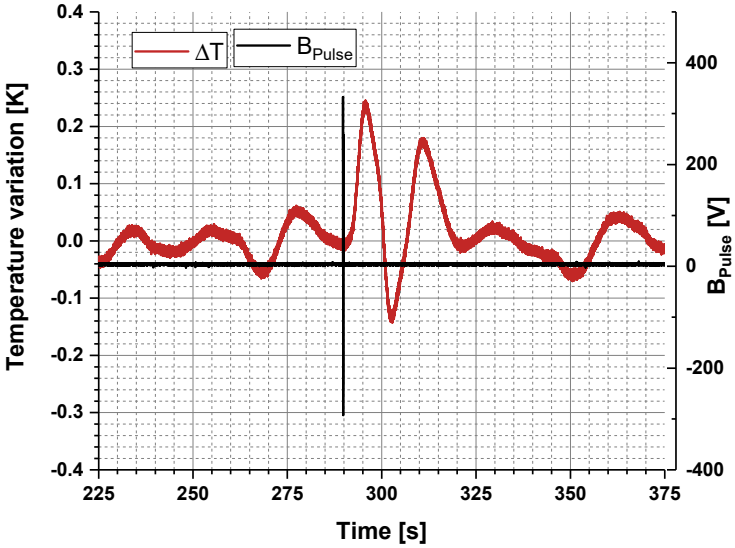

Figure A.3 – Temperature variation between upstream and downstream average temperatures measured during test run #CSJA8Q011206 as function of time. The battery voltage used to generate the pulse magnetic field is in black.

The time difference can also be determined by the helium flow rate as the time needed for the helium slug to travel from T_{up} to T_{down} locations. It is assumed that the helium is flowing in a channel of 0.8 m length with velocity:

$$v_{helium} = \frac{\dot{m}}{\rho_{he} A_{he}}. \quad \textbf{(A.1)}$$

Then the time needed for the coolant to transfer from upstream to downstream sensors is t_{helium} = 5.8 s, which is 20% less than the empirically obtained t_{offset}. This value is calculated using the hydraulic parameters listed in Table 4.5. The agreement of empirical and calculated propagation times is fair since the parameters listed in Table 4.5 might have error bars that cumulate into such difference. However, looking at [116] and [117], v_{eff} = 0.11 m/s is a realistic value compared with the velocities determined for different CICCs.

There are several elements, which support the hypothesis that the fluctuation is generated by the helium control system at inlet. First, the t_{offset} is different for every initial temperature as listed in Table A.1. This variation is compatible with the helium density variation, which depends on the temperature. Higher temperature corresponds to higher density and a slower heat slug transport considering the mass flow constant.

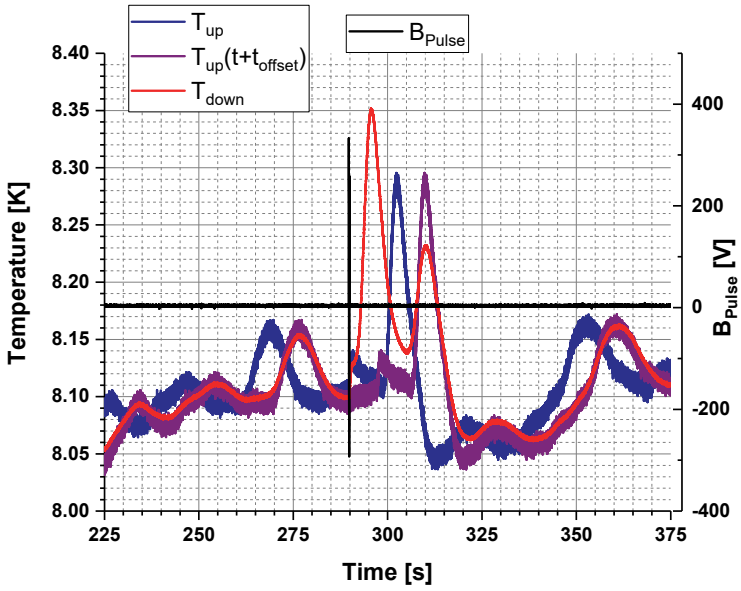

Figure A.4 – Temperature measured during test run #CSJA8Q011206 as function of time. In blue, the average upstream temperature (T_{up}), while the temperatures measured downstream the high field zone (T_{down}) is in red. The upstream temperature shifted by the time offset is in purple and covering the red curve during the bias oscillations. The battery voltage used to generate the pulse magnetic field is in black.

Second, the helium heat capacity per unit of volume is about two orders of magnitude larger than the heat capacity of the superconductor plus copper composite, $\sim 10^5$ and $\sim 10^3$ J/(m^{3}K), respectively. Therefore, considering coolant and composite at similar temperature, the helium slug is capable to cross the conductor length with negligible small variation of temperature. Since the heat slug is propagating in the conductor with small variation, it is possible to visualize how the fluctuation crosses the conductor. In Figure A.5, the average upstream and downstream temperatures are compared to the T_{inlet} and $T_{0\ left}$ sensors, placed at the helium inlet and at the beginning of the conductor respectively. There is a first temperature peak visible in T_{inlet}, probably generated at the temperature controller, trying to compensate the temperature and pressure changes initiated during the magnetic field pulse. This peak propagates in the conductor and is measured by all the sensors at different times, depending on the helium flow. The peak is also followed by minor adjustments of the temperature controller, which generates the fluctuations at 340-350 s and 360-370 s.

Table A.1 – Empirically calculated time delay between upstream and downstream temperature.

Temperature [K]	ρ_{he} *[kg/m³]*	t_{offset} *[s]*
7.75 ± 0.05	99 ± 1	8.3 ± 0.3
8.10 ± 0.05	91 ± 1	7.5 ± 0.3
8.40 ± 0.05	85 ± 1	7.3 ± 0.3
8.59 ± 0.05	81 ± 1	6.9 ± 0.3

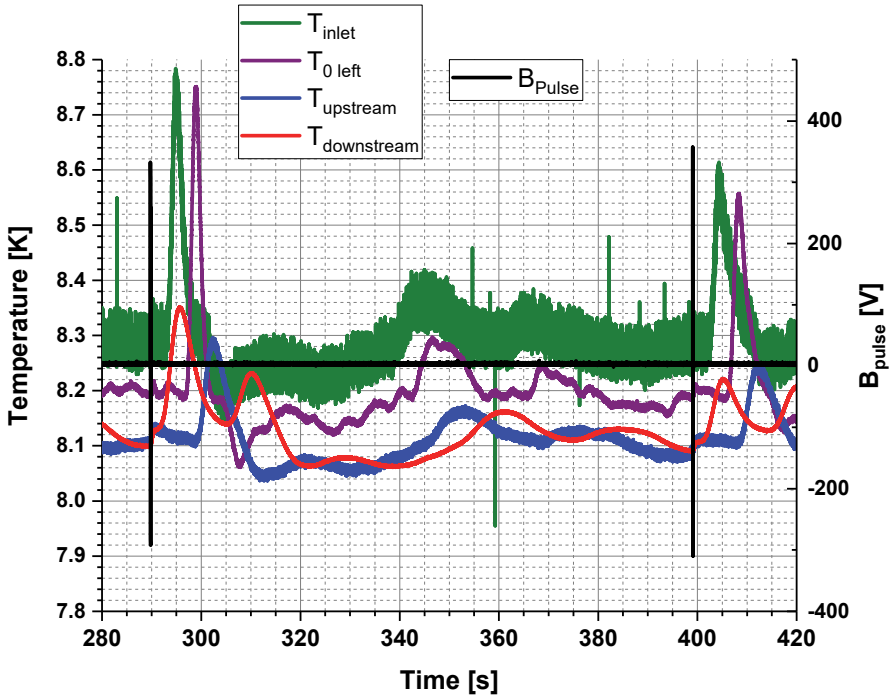

Figure A.5 – Temperature measured during test run #CSJA8Q011206 as function of time. $T_{upstream}$ and $T_{downstream}$ are average temperatures, while $T_{0\ left}$ and T_{inlet} are measured by single sensors.

Since, the temperature fluctuations decrease in time after the pulse, tending to the correct temperature, and the peak positions clearly correlate with the helium flow, the most probable origin for the fluctuation is the PID temperature controller. Altogether, subtracting the average temperatures after compensation for the helium flow time offset, allows to accurately calculating the temperature difference in time generated by the applied magnetic field pulse.

A.3. Energy Calculation

In Figure A.4, after shifting the upstream profile, as $T_{up}(t+t_{offset})$, a very good match between both bias profiles is found. The temperature difference between upstream and downstream average temperatures is then calculated and shown in Figure A.6. The large bias oscillations are annulled and the remaining temperature difference ΔT, versus time can be used to calculate the deposited energy using eq. (3.1).

The integral of the temperature as function of time is calculated between the instant at which the magnetic field pulse is applied and the time where the temperature has returned to the stationary condition.

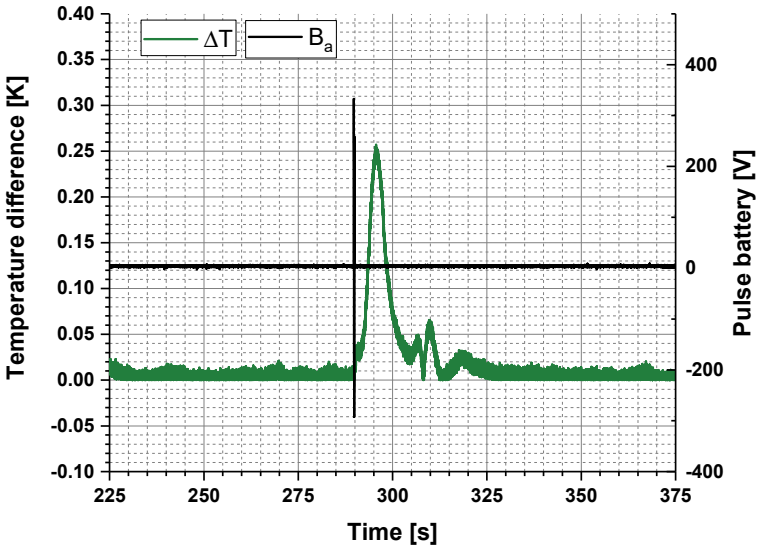

Figure A.6 – Temperature difference (ΔT) between upstream and downstream temperatures as function of time, represented by the green line. The battery voltage used to generate the pulse magnetic field is in black.

In the temperature difference profile, a second smaller fluctuation is observed while the curve is approaching zero, in this example between 305 and 315 s. The fluctuation is generated during the second temperature peak, visible in both T_{up} and T_{down}, see Figure A.4. The two peaks upstream and downstream are not equivalent; therefore the difference is not zero. This fluctuation is likely caused by the temperature controller and is observed in all the temperature measurements of the MQE tests performed on CSJA8 and it is considered as relevant in the

integration of the energy in order to avoid an underestimation of the deposited energy.

The temperature integral is then multiplied by the mass flow and specific heat of the helium. In this case the mass-flow is 3.3 g/s and the average specific heat at 8.1 K is 8325 $J/kg \cdot K$. The resulting energy is 432 mJ/cm^3.

Ignoring the minor peak and considering the system restored at about 310 s, the calculated energy is 353 mJ/cm^3. The difference between both calculated energies is about 15% strengthening the estimate that the error for the energy measured during the stability test might be better than 10%.

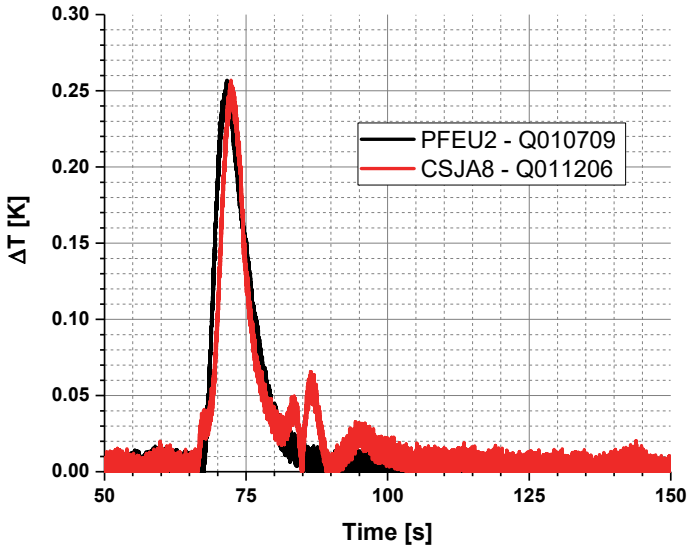

Figure A.7 – Temperature difference (ΔT) between upstream and downstream temperatures as function of time of sample CSJA8 and PFEU2. The PFEU2 temperature is scaled in order to compensate the different helium density and mass flow.

The second peak is not observed in the PF conductor tests, where the MQE was measured below 6 K. In order to analyze the trend of the temperature difference, the ΔT measured during the stability test of sample PFEU2 is compared to the peak in Figure A.6. The helium flow during the test of the PFEU2 at 5.7 K has lower mass flow, 2.5 g/s, and higher density. Therefore, the coolant spends about twice the time to travel along the same cable length. After applying a correction factor to the PFEU2 helium velocity, the temperature variations are compared in Figure A.7. This comparison strongly suggests that the small fluctuation at the end of the pulse, not

observed during the PFEU2 test, is an anomaly generated by the temperature controller.

In conclusion, the energy generated during the stability test of the CSJA8 sample can be calculated considering a correction for the coolant flow transfer in the conductor. The calculated energy is somewhat affected by the minor peak observed in the temperature difference at the end of the pulse allowing a maximum error of about 10%. For future analysis of stability measurements on Nb_3Sn conductors the proposed calculation methodology is recommended in order to allow an accurate energy calculation.

REFERENCES

[1] K.J. Shultis and R.E. Faw, *Fundamentals of Nuclear Science and Engineering*. Book, 2nd ed., CRC Press, Ed., Taylor & Francis, 2007.

[2] H.A. Bethe, "The Hydrogen Bomb", *Bullettin of the Atomic Scinetist*, vol. 6, no. 4, pp. 99-104, 1950.

[3] G.H. Miley, H. Towner and N. Ivich, "Fusion cross sections and reactivities", Illinois Univ., Urbana (USA), Technical report, 1974.

[4] P.H. Rebut, "The JET preliminary tritium experiment", *Plasma Physics and Controlled Fusion*, vol. 34, no. 13, p. 1749, 1992.

[5] N. Mitchell, "Design Description Document: 11 - Magnet, ITER_D_22HV5L v2.2", ITER-IO, Technical report, 2009.

[6] F. Romanelli, "A roadmap to the realization of fusion energy", in *European Energy Conference*, Hungary, 2013.

[7] Y. Xu, "A general comparison between tokamak and stellarator plasmas", *Matter and Radiation at Extremes*, vol. 1, no. 4, pp. 192-200, 2016.

[8] H.S. Bosch, "Wendelstein 7-X – a Technology Step towards Demo", *Plasma and Fusion Research*, vol. 5, p. S1002, 2011.

[9] V.D. Shafranov, B.D. Bondarenko, G.A. Goncharov, O.A. Lavrent'ev and A.D. Sakharov, "On the history of the research into controlled thermonuclear fusion", *Physics Uspekhi*, vol. 44, pp. 835-843, 2001.

[10] IAEA Agency, "Summary of the ITER final design system", Vienna, Technical report, EDA/DS/22, 2001.

[11] A. Devred, I. Backbier, D. Bessette, G. Bevillard, M. Gradner, C. Jong, F. Lillaz, N. Mitchell, G. Romano and A. Vostner, "Challenges and status of ITER conductor production", *Superconductor Science and Technology*, vol. 27, p. 044001, 2014.

[12] H.H.J. ten Kate, "The ATLAS superconducting magnet system at the Large Hadron Collider", *Physica C: Superconductivity*, vol. 468, no. 15-20, pp. 2137-42, 2008.

[13] N. Mitchell, A. Devred, P. Libeyre, B. Lim and F. Savary, "The ITER Magnets: Design and Construction Status", *IEEE Transaction on Applied Superconductivity*, vol. 22, no. 3, p. 4200809, 2012.

[14] W. Reiersen, "Toroidal Field Coil Conductor", ITER-US, Oak Ridge National Laboratory, Technical report, 2018.

[15] J. H. Schultz, T. Antaya, J. Feng, C. Gung, N. Martovetsky, J.V. Minervini, P. Michael, A. Radovinsky and P. Titus, "The ITER Central Solenoid", in *21st IEEE/NPS Symposium of Fusion Engineering*, Knoxville, TN, USA, 2005.

[16] B. Lim, F. Simon, Y. Ilyn, C.Y. Gung, J. Smith, Y. H. Hsu, C. Luongo, C. Jong and N. Mitchell, "Design of the ITER PF Coils", *IEEE Transaction on Applied Superconductivity*, vol. 21, no. 3, pp. 1918 - 1921, 2011.

[17] N. Mitchell, "Scenarios for coil, power supply and cryoplant analysis v1.10", ITER-IO, Technical report, 2FTVKY, 2009.

[18] K. Kim et al., "Conceptual design study of the K-DEMO magnet system", *Fusion Engineering and Design*, vol. 96-97, pp. 281-285, 2015.

[19] J. Zheng et al., "Concept design of CFETR superconducting magnet system based on different maintenance ports", *Fusion Engineering and Design*, vol. 88, no. 11, pp. 2960-66, 2013.

[20] L. Zani et al., "Overview of Progress on the EU DEMO Reactor Magnet System Design", *IEEE Transaction on Applied Superconductivity*, vol. 26, no. 4, p. 4204505, 2016.

[21] P. Bruzzone, K. Sedlak, B. Stepanov, L. Muzzi, S. Turtú, A. Anemona and J. Harman, "Design of Large Size, Force Flow Superconductors for DEMO TF Coils", *IEEE Transaction on Applied Superconductivity*, vol. 24, no. 3, p. 4201504, 2014.

[22] A. Torre, D. Ciazynski, P. Hertout and L. Zani, "Tools Used at CEA for Designing the DEMO Toroidal Field Coils Winding Pack", *IEEE Transaction on Applied Superconductivity*, vol. 26, no. 4, p. 4902005, 2016.

[23] Y. Krivchenkov, C. Sborchia, B. Stepanov and A. Panin, "Assessment of the radial plate design of the ITER TF coil winding pack", *IEEE Transactions on Applied Superconductivity*, vol. 10, no. 1, pp. 592-5, 2000.

[24] N. Mitchell, D. Bessette, N. Gallix, C. Jong, J. Knaster, P. Leyre, C. Sborchia and F. Simon, "The ITER Magnet System", *IEEE Transaction on Applied Superconductivity*, vol. 18, no. 2, pp. 435 - 40, 2008.

[25] National High Magnetic Field Laboratory - Applied Superconductivity Centre, Tallahasse, USA. (2018) Materials database available on website. https://nationalmaglab.org/magnet-development/applied-superconductivity-center/plots.html

[26] L. Bottura, "A Practical fit for the Critical Surface of NbTi", *IEEE Transaction on Applied Superconductivity*, vol. 10, no. 1, pp. 1054-1057, 2000.

[27] A. Godeke, B. ten Haken, H.H.J. ten Kate and D.C. Larbalestier, "A general scaling relation for the critical current density in Nb3Sn", *Superconductor Science and Technology*, vol. 19, no. 10, p. R100, 2006.

[28] L. Muzzi, G. De Marzi, C. Fiammozzi Zignani, U. Besi Vetrella, V. Corato, A. Rufoloni and A. della Corte, "Test Results of a NbTi Wire for the ITER Poloidal Field Magnets: A Validation of the 2-Pinning Components Model", *IEEE Transaction on Applied Superconductivity*, vol. 21, no. 3, pp. 3132-37, 2010.

[29] X.F. Lu, D.M.J. Taylor and D. Hampshire, "Critical current scaling laws for advanced Nb3Sn superconducting strands for fusion applications with six free parameters", *Superconductor Science and Technology*, vol. 21, no. 10, p. 105016, 2008.

[30] A. Nijhuis and et al., "The effect of axial and transverse loading on the transport properties of ITER Nb3Sn strands", *Superconductor Science and Technology*, vol. 26, no. 8, p. 084004, 2013.

[31] C.S. Myers, M.A. Susner, L. Motowildo, J. Distin, M.D. Sumption and E.W. Collings, "Specific Heats of Composite Bi2212, Nb3Sn and MgB2 Wire Conductors", *IEEE Transaction on Applied Superconductivity*, vol. 23, no. 3, p. 8800204, 2013.

[32] Y. Iwasa, *Case studies in superconducting magnets*. Book, 2nd ed. NewYork, Springer, 2009.

[33] M.N. Wilson, *Superconducting Magnets*. Book. Oxford, U.K., Oxford Science Publications, 1983.

[34] I. Pong, A. Vostner, B. Bordini, M. Jewell, F. Long, Y. Wu, L. Bottura, A. Devred, D. Bessette and N. Mitchell, "Current sharing temperature of NbTi SULTAN samples compared to prediction using a single pinning mechanism parametrization for NbTi strand", *Superconductor Science and Technology*, vol. 25, no. 5, p. 054011, 2012.

[35] E. Seiler, D. Richter, B. Bordini, L. Bottura, D. Bessette, A. Vostner and A. Devred, "Hysteresis losses and effective Jc(B) scaling law for ITER Nb3Sn strands.", *IEEE Transaction on Applied Superconductivity*, vol. 26, no. 2, p. 8200307, 2016.

[36] N. Mitchell, "Dedisgn Description Document 11-7: Conductors 2NBKXY v1.2", ITER-IO, Technical report, 2009.

[37] Y. Miyoshi, E.P.A. van Lanen, M.M.J. Dhallé and A. Nijhuis, "Microscopic Fractures and Transport Degradation in ITER Type Nb3Sn Strands", *IEEE Transaction on Applied Superconductivity*, vol. 20, no. 3, pp. 1404-7, 2010.

[38] National High Magnetic Field Laboratory. (2008) CICC Montage showing the components of a Superconducting Cable-In-Conduit Conductor for ITER. https://nationalmaglab.org/magnet-development/applied-superconductivity-center/asc-image-gallery/nb3sn-image-gallery

[39] A. Devred, I. Backbier, D. Bessette, G. Bevillerd, M. Gardner, M. Jewell, N. Mitchell, I. Pong and A. Vostner, "Status of the ITER Conductor Development and Production", *IEEE Transaction on Applied Superconductivity*, vol. 22, no. 3, p. 4804909, 2012.

[40] G. Ries, "AC-losses in multifilamentary superconductors at technical frequencies", *IEEE Transactions on Magnetics*, vol. 13, no. 1, pp. 524-6, 1977.

[41] A.M. Campbell, "A general treatment of losses in multifilamentary superconductors", *Cryogenics*, vol. 22, no. 1, pp. 3-16, 1982.

[42] A. Nijhuis, Y. Ilyin, W. Abbas, B. ten Haken and H. ten Kate, "Change of interstrand contact resistance and coupling loss in various prototype ITER NbTi conductors with transverse loading in the Twente Cryogenic Cable Press up to 40,000 cycles", *Cryogenics*, vol. 44, no. 5, pp. 319-339, 2004.

[43] A. Nijhuis, H.H.J. ten Kate, J.L. Duchateau and P. Bruzzone, "Coupling Loss Time Constants in Full-Size Nb3Sn CIC Model Conductors for Fusion Magnets", in *Advances in Cryogenic Engineering Materials*. Boston, MA: Springer, vol. 42, pp. 1281-8, 1996.

[44] C. Zhou, D. Bink, B. Liu, Y. Miyoshi, W. A. Wessel, H. J. G. Krooshoop and A. Nijhuis, "Magnetization measurements on ITER Nb3Sn CICC and strands subjected to irreversible strain degradation", *Superconductor Science and Technology*, vol. 25, no. 7, p. 075004, 2012.

[45] L.N. Cooper, "Bound Electron Pairs in a Degenerate Fermi Gas", *Physical Review*, vol. 104, no. 4, pp. 1189-90, 1956.

[46] W.J. Carr Jr., "Ac loss in a twisted filamentary superconducting wire. I", *Journal of Applied Physics*, vol. 45, pp. 929-34, 1974.

[47] W.J. Carr Jr., "Ac loss in a twisted filamentary superconducting wire. II", *Journal of Applied Physics*, vol. 45, pp. 935-40, 1974.

[48] A. Nijhuis and H.H.J. ten Kate, "Surface Oxidation and Interstrand Contact Resistance of Cr-Coated Nb3Sn and Bare NbTi Strands in CCIC's", in *Advances in Cryogenic Engineering Materials*.: Springer, vol. 46, pp. 1083-90, 2000.

[49] E.P.A. van Lanen, J. van Nugteren and A. Nijhuis, "Validation of a strand level CICC-joint coupling loss model", *Superconductor Science and Technology*, vol. 25, no. 2, p. 025013, 2012.

[50] E.P.A. van Lanen, J. van Nugteren and A. Nijhuis, "Full-scale calculation of the coupling losses in ITER size cable-in-conduit conductors", *Superconductor Science and Technology*, vol. 25, no. 2, p. 025012, 2012.

[51] E.P.A. van Lanen and A. Nijhuis, "JackPot: A novel model to study the influence of current non-uniformity and cabling patterns in cable-in-conduit conductor", *Cryogenics*, vol. 50, no. 3, pp. 139-148, 2010.

[52] E.P.A. van Lanen and A. Nijhuis, "Simulation of interstrand coupling loss in cable-in-conduit conductors with JackPot-AC", *IEEE Transaction on Applied Superconductivity*, vol. 21, no. 3, pp. 1926-1929, 2011.

[53] G. Rolando, E.P.A. van Lanen and A. Nijhuis, "Minimum quench power dissipation and current non-uniformity in international thermonuclear experimental reactor type NbTi cable-in-conduit conductor samples under direct current conditions", *Applied Physics*, vol. 111, p. 093904, 2012.

[54] G. Rolando, A. Devred and A. Nijhuis, "Minimizing coupling loss by selection of twist pitchlengths in multi-stage cable-in-conduit conductors", *Superconductor Science and Technology*, vol. 27, no. 1, p. 015006, 2014.

[55] L. Bottura, "Cable Stability", in *Proceedings of CERN Accelerator School*, 2013.

[56] P. Bruzzone, B. Stepanov, R. Wesche, Y. Ilyn, R. Herzog, M. Calvi, M. Bagnasco and F. Cau, "Methods, Accuracy and Reliability of ITER Conductor Tests in SULTAN", *IEEE Transaction on Applied Superconductivity*, vol. 19, no. 3, pp. 1508-11, 2009.

[57] Horizon Technologies. (2013) CryoSoft Suite. http://www.htess.com/cryosoft.htm

[58] P. Bruzzone, A. Anchel, A. Fuchs, G. Pasztor, B. Stepanov, M. Vogel and G. Vecsey, "Upgrade of Operating Range for SULTAN Test Facility", *IEEE Transaction on Applied Superconductivity*, vol. 12, no. 1, pp. 520-3, 2002.

[59] T. Kato, "First test results for the ITER central solenoid model coil", *Fusion Engineering and Design*, vol. 56-57, pp. 59-70, 2001.

[60] L. Reccia et al., "Preparation of PF1/6 and PF2 Conductor Performance Qualification Sample", *IEEE Transaction on Applied Superconductivity*, vol. 21, no. 3, pp. 1930 - 1933, 2010.

[61] B. Stepanov, P. Bruzzone, R. Wesche, N. Martovetsky, D. Hatfield, A. Vostner and A. Devred, "Impact of Sample Preparation Procedure on the Test Results of Four US ITER TF Conductors", *IEEE Transaction on Applied Superconductivity*, vol. 20, no. 3, pp. 508 - 511, 2010.

[62] M. Breschi et al., "Results of the TF conductor performance qualification samples for the ITER project", *Superconductor Science and Technology*, vol. 25, no. 9, p. 095004, 2012.

[63] P. Bruzzone, A. Fuchs, B. Stepanov and G. Vecsey, "Performance evolution of Nb3Sn cable-in-conduit conductors under cyclic load [for Tokamaks]", *IEEE Transaction on Applied Superconductivity*, vol. 12, no. 1, pp. 516-9, 2002.

[64] P. Bruzzone, "Segregated Copper Ratio Experiment On Transient Stability (SeCRETS)", Swiss Plasma Center, Lausanne (Switzerland), Technical report, 2001.

[65] R.J. Thome and A.M. Dawson, "Pool-Cooled Superconducting Coils: Past, Present and Future", in *Advances in Cryogenic Engineering, Volume 31*. New York: Springer US, 1986.

[66] M Breschi, D. Carati, D. Bessette, A. Devred, G. Romano, A. Vostner and C. Zhou, "Performance analysis of the Nb-Ti conductor qualification samples for the ITER project", *Superconductor Science and Technology*, vol. 28, no. 11, p. 115001, 2015.

[67] P. Readman, "PFEU2 SULTAN sample test report", Fusion For Energy, Technical report, F4E_D_22TW6E, 2014.

[68] D. Bessette, "Assessment of the performance of the CSJA8 sample", ITER-IO, Internal report, 2016.

[69] T. Bagni, M. Breschi, J.L. Duchateau, A. Devred and A. Nijhuis, "Analysis of ITER Nb-Ti and Nb3Sn CICCs experimental Minimum Quench Energy with JackPot, MCM and THEA models", *Superconductor Science and Technology*, vol. 30, no. 9, p. 095003, 2017.

[70] A. Nijhuis, Y. Ilyn, W. Abbas, H.H.J. ten Kate, M.V. Ricci and A. della Corte, "Impact of Void Fraction on Mechanical Properties and Evolution of Coupling Loss in ITER Nb3Sn Conductors Under Cyclic Loading", *IEEE Transaction on Applied Superconductivity*, vol. 15, no. 2, pp. 1633-6, 2005.

[71] Y.A. Ilyin, A. Nijhuis, W. Abbas, P. Bruzzone, B. Stepanov, L. Muzzi, P. Gislon and L. Zani, "Effect of Cycling Loading and Conductor Layout on Contact

Resistance of Full-Size ITER PFCI Conductors", *IEEE Transaction on Applied Superconductivity*, vol. 15, no. 2, pp. 1359 - 62, 2005.

[72] F.W. Grover, *Inductance calculation*. Book. New York, U.S.A., Dover Publications, 2004.

[73] J.L. Duchateau, B. Turck, B. Lacroix, M. Schwarz, A. Torre and L. Zani, "Stability of a Cable in Conduit Conductor Under Fast Magnetic Field Variations", *IEEE Transaction on Applied Superconductivity*, vol. 22, no. 3, p. 4803205, 2012.

[74] A. Nijhuis, H.H.J. ten Kate, JL Duchateau and P. Bruzzone, "Coupling Loss Time Constants in Full-Size Nb3Sn CIC Model Conductors for Fusion Magnets", *Advances in Cryogenic Engineering Materials*, vol. 42, pp. 1281-8, 1997.

[75] J.L. Duchateau, B. Turck and D. Ciazynski, "Coupling current losses in composites and cables: analytical calculations", in *Handbook of Applied Superconductivity*. Bristol: CRC Press, pp. 205, 1998.

[76] B. Turck and L. Zani, "A macroscopic model for coupling current losses in cables made of multistages of superconducting strands and its experimental validation", *Cryogenics*, vol. 50, no. 8, pp. 443-9, 2010.

[77] L. Bottura, C. Rosso and M. Breschi, "A General Model for Thermal, Hydraulic and Electric Analysis of Superconducting Cables", *Cryogenics*, vol. 40, no. 8-10, pp. 617-626, 2000.

[78] A. Devred, I. Backbier, D. Bessette, G. Bevillerd, M. Gardner, M. Jewell, N. Mitchell, I. Pong and A. Vostner, "Status of the ITER Conductor Development and Production", *IEEE Transaction on Applied Superconductivity*, vol. 22, no. 3, p. 4804909, 2012.

[79] J.L. Duchateau, "MCM characterization of the Sultan ITER PF1-6 sample (PFEU2)", ITER-IO, Internal report, 2015.

[80] P. Bruzzone, A. Fuchs, B. Stepanov and G. Vecsey, "Transient Stability Results for Nb3Sn Cable-in-Conduit Conductors", *IEEE Transaction on Applied Superconductivity*, vol. 12, no. 1, pp. 512-515, 2002.

[81] M. Bagnasco, "Calorimentric Method for current sharing temperature measurements in ITER conductor samples in SULTAN", *Fusion Engineering and Design*, vol. 84, no. 2-6, pp. 423-426, 2009.

[82] D.M.J. Taylor and D.P. Hampshire, "Relationship between the n-value and critical current in Nb3Sn superconducting wires exhibiting intrinsic and

extrinsic behaviour", *Superconductor Science and Technology*, vol. 18, pp. 297 - 302, 2005.

[83] A. Devred et al., "Status of Conductor Qualification for the ITER Central Solenoid", *IEEE Transaction on Applied Superconductivity*, vol. 23, no. 3, p. 6001208, 2013.

[84] E.P.A. van Lanen, J. van Nugteren and A. Nijhuis, "Validation of a strand-level CICC-joint coupling loss model", *Superconductor Science and Technology*, vol. 25, no. 2, p. 025013, 2012.

[85] ITER - Development of superconducting magnet, "Conductor parameters of the CSJA8 sample", ITER - Japan, Technical Report, 2016.

[86] L. Bottura and B. Bordini, "Jc(B,T) Parametrization for the ITER Nb3Sn Production", *IEEE Trans. Appl. Supercond.*, vol. 19, no. 3, pp. 1521-1524, 2009.

[87] S.P. Kwon, K. Sim, Y. J. Ma, S. Park, P. Park, I. Shin, H. Choi, Y. Seo, K. Jang and W. Park, "Prototype Nb3Sn Superconducting Strad for ITER CS Coil Conductor Produced in Korea Using the Internal-Tin Route", *IEEE Transactions on Applied Supercond.*, vol. 25, no. 3, p. 4201106, 2015.

[88] A. Nuijhuis, R. Lubkemann, H.J.G. Krooshoop, and W.A.J. Wessel, "Results of TARSIS and Pacman Ic(strain) testing on CSKO1 –D3 Nb3Sn strand", University of Twente, Technical Report , UT-IO-2014, 2014.

[89] J.L. Duchateau, "MCM for CSJA8 left leg", ITER-IO, Internal report, 2016.

[90] T. Bagni, J. L. Duchateau, A. Devred and A. Nijhuis, "Quench energy studies in ITER conductors for different magnetic field perturbations with Jackpot and THEA combined models", *Superconductor Science and Technology*, vol. 31, no. 9, p. 095001, 2018.

[91] M. Breschi, L. Trevisani, L. Bottura, A. Devred and F. Trillaud, "Comparing the Thermal stability of NbTi and Nb3Sn wires", *Superconductor Science and Technology*, vol. 22, no. 2, p. 025019, 2009.

[92] Horizon Technologies, "HePak Version 3.4", Cryodata Inc., 2013.

[93] D. Bessette, "Conductor Parameters for 2008-2009 analyses", ITER-IO, Internal report, 2009.

[94] D. Everitt and et al., "ITER Central Solenoid design", in *IEEE 25th Symposium on Fusion Engineering (SOFE)*, San Francisco, CA, 2013.

[95] P. Libeyre, N. Mitchell, D. Bessette, Y. Gribov, C. Jong and C. Lyraud, "Detailed design of the ITER central solenoid", *Fusion Engineering and Design*, vol. 84, no. 7-11, pp. 1188-91, 2009.

[96] G. Rolando, A. Devred and A. Nijuis, "Temperature and current margin of ITER central solenoid conductor designs during a 15MA plasma scenario", *Superconductor Science and Technology*, vol. 27, no. 2, p. 025010, 2014.

[97] A. Nijhuis, Y. Ilyin, W. Abbas, B. ten Haken and H.H.J. ten Kate, "Performance of an ITER CS1 Model Coil Conductor Under Transverse Cyclic Loading up to 40,000 Cycles", *IEEE Transaction on Applied Superconductivity*, vol. 14, no. 2, pp. 1489 - 94, 2004.

[98] N. Martovetsky et al., "ITER Central Solenoid Insert Test Results", *IEEE Transaction on Applied Superconductivity*, vol. 26, no. 4, p. 4200605, 2016.

[99] P. Bauer, H. Rajainmaki and E. Salpiero, "Material Data for Superconductor Simulation", EFDA CSU, Garching, Technical report, 2007.

[100] R. Zanino, P. Santagati, L. Savoldi, A. Martinez and S. Nicollet, "Friction Factor Correlation with Application to the Central Cooling Channel of Cable-in-Conduit Conductors for Fusion Magnets", *IEEE Transaction on Applied Superconductivity*, vol. 10, no. 1, pp. 1066 - 69, 2000.

[101] H. Hamada, T. Kato, K. Kawano, E. Hara, T. Ando, H. Tsuji, K. Okuno, R. Zanino and L. Savoldi, "Experimental Results of Pressure Drop Measurement in ITER CS Model Coil Test", in *Advances in Cryogenic Engineering: Proceedings of the Cryogenic Engineering Conference - CEC*, Madison, WI, 2002, pp. 407-414.

[102] A. della Corte et al., "Successful performances of the EU-AltTF sample, a large size Nb3Sn cable-in-conduit conductor with rectangular geometry", *Superconductor Science and Technology*, vol. 23, no. 4, p. 045028, 2010.

[103] P. Bruzzone, K. Sedlak, B. Stepanov, R. Wesche, L. Muzzi, M. Seri, L. Zani and M. Coleman, "Design, Manufacture and Test of a 82 kA React&Wind TF Conductor for DEMO", *IEEE Transaction on Applied Superconductivity*, vol. 26, no. 4, p. 4801805, 2016.

[104] K. Sedlak, "CRPP Design Specification for RW prototype LTS conductor", Swiss Plasma CEnter, Technical report, 2013.

[105] A. Nijhuis, H.J.G. Krooshoop and R. Lubkemann, "TF conductor strand sample thermo mechanical critical performance test", University of Twente, Enschede, Technical report, 2015.

[106] C. Reurslag, A. Nijhuis and M. Dhallé, "Influence of magnetic field, current injection joint length and strand diameter on the entrance effect of superconducting Nb3Sn strands", University of Twente, Enschede, NL, Master's thesis, 2017.

[107] L. Muzzi and et al., "Design, Manufacture, and Test of an 80 kA-Class Nb3Sn Cable-In-Conduit Conductor With Rectangular Geometry and Distributed Pressure Relief Channels", *IEEE Transaction on Applied Superconductivity*, vol. 27, no. 4, p. 4800206, 2017.

[108] A. Nijhuis and K. Yagotintsev, "TF CICC conductor sample cyclic mechanical critical performance test", University of Twente, Enschede, NL, Technical report, 2016.

[109] L. Muzzi, A. Di Zenobio and P. Bruzzone, "Fabrication of two short length TF conductor sections, RW1 and WR1", EURO-fusion, Technical report, 2015.

[110] P. Bruzzone, B. Stepanov, D. Uglietti, R. Wesche and K. Sedlak, "EDIPO: The Test Facility for High-Current High-Field HTS Superconductors", *IEEE Transaction on Applied Superconductivity*, vol. 26, no. 2, p. 9500106, 2016.

[111] P. Bruzzone, B. Stepanov, R. Wesche, K. Sedlak and D. Uglietti, "EDIPO Test Facility", Swiss Plasma Center, Villigen, Technical report, 2015.

[112] K. Yagotintsev and A Nijhuis, "AC loss measurement with transverse load cycles in Twente Press on CS Jastec 83JNM001-S4T1 sample", University of Twente, Enschede, NL, Technical report, 2014.

[113] V. B. Zenkevitch and A. S. Romanyuk, "The effect of magnetic properties of a composite superconductor on the losses in variable magnetic field: Part 1 Theory", *Cryogenics*, vol. 19, no. 12, pp. 725-730, 1979.

[114] B.L. Brandt, D.W. Liu and L.G. Rubin, "Low temperature thermometry in high magnetic fields. VII. Cernox™ sensors to 32 T", *Review of Scientific Instruments*, vol. 70, no. 1, p. 104, 1999.

[115] P. Bruzzone, B. Stepanov, R. Wesche, Y. Ilyin, R. Herzog, M. Calvi, M. Bagnasco and F. Cau, "Methods, Accuracy and Reliability of ITER Conductor Tests in SULTAN", *IEEE Transactions on Applied Superconductivity*, vol. 19, no. 3, pp. 1508-11, 2009.

[116] C. Marinucci, L. Bottura, P. Bruzzone and B. Stepanov, "Analysis of the transverse heat transfer coefficients in a dual channel ITER-type cable-in-conduit conductor", *Cryogenics*, vol. 47, pp. 563-76, 2007.

[117] R. Herzog, M. Lewandowska, M. Calvi and D. Bessette, "Helium flow and temperatures in a heated sample of a final ITER TF cable-in-conduit conductor", *Journal of Physics: Conference Series*, vol. 234, p. 032022, 2010.

ACKNOWLEDGEMENT

The research and particularly the PhD research is psychologically tough, there is a lot of competition coming from many clever people and, in addition, it leads to an unpredictable future. Sometimes it does not look worthy, but eventually I enjoyed it and I am proud to have pursued it.

This experience moved my horizon further away and it brought me to meet many interesting people from many different places. I would like to thank all the people who have walked with me along this journey, some were there from the beginning, others shared only few steps, but anyway I want to thank them all, I would not be here without you.

I cannot thank enough Arend Nijhuis, my day-by-day supervisor, for his constant support and patience. He has been my mentor, I asked him many questions and he always pointed me in the right direction as well as stimulating me to expand my knowledge on new areas. I would like to thank my promoters Herman Ten Kate and Jean-Marie Noterdaeme, which have helped me with their guidance, increasing the value of my work. I would also like to thank all the members of my graduation committee: Wolfgang Biel, Filip De Turck, Arnaud Devred, Jennifer Herek, Hans Hilgenkamp Anna Kario and Marcel ter Brake for their constructive criticisms.

My research work is the result of a collaboration between Ghent University, University of Twente and ITER-Organization. Therefore, I had the opportunity to spend a long period at ITER Head Quarter in France, where I met and worked with many capable people. I thank all of them for the time spent together and I am particular grateful to Jean-Luc Duchateau, Denis Bessette and Florent Gauthier, which participated to interesting discussions sharing their knowledge on many different subjects. A special thanks to Marco Breschi from University of Bologna for our discussions and skype calls on energy calculation.

A Joint Doctorate can be complicated also from the organization point of view. I would like to thank Eveline Indemans, Frank Janssens and Kathleen Van Oost from Ghent University and Ans Veenstra from University of Twente for organizing everything nicely and finding the answers to all my questions.

I spent most of my PhD at the EMS group of University of Twente. I would like to thank you all for the nice time spent together mostly during lunches and coffee breaks. From the many people that I met I would like to send a special greeting to

Marc, Srinivas, Nir, Anvar, Anne, Cris, Peng, Jianfeng, Chao, Sahil, Michiel, Sander, Ruben, Harry, Erik, Tim, Koen, Jeroen, Nando, Wilco, Jaap, Goncalo and Izak. A special thanks to Marcel Dijkstra, we worked side-by-side for more than one year to rewrite JackPot, without you this research would not have been possible.

I am grateful for the new and old friends who accompanied me during this adventure. Tiemo, the time spent together inside and outside the University was always pleasant, thank you for everything from the jokes to the very serious conversations. Marc Coatanea-Gouachet, the breaks at ITER were a continuous laugh thanks to you, thanks for the crazy talks. Helios, Leo, Enri, Paz and Tere our fixed appointment for RPGs allowed me not to feel the distance that separates us. Thanks for never making me feel out of the group and for the special spot on the hobs. Tam, Lea e Random our games were less frequent but equally useful for my mental health.

I was surprised to discover at University of Twente a large community of Italian people. I met many of them and with some, I have forged a bond, which has been extended far beyond the PhD period. Giorgio e Virgi, we shared a lot from climbing to numerous lunches together, I had a lot of fun with you. Caterina, Fede and Ettorino, your warm hospitality always made me feel welcome. Alberto, Ludovica and Allegra, we come from the same city and we became friends in Enschede, I am really happy to have met you.

Loredana, I do not have words to describe the gratitude and the love I feel for you. You do everything to make me a better man, even if I oppose strenuous resistance to the change. Grazie.

Papà, mamma e Francesco, you have supported me since the beginning of this long journey and you have never made me feel far away even during difficult times. Grazie, for all the love and support you have always given me, without you I would not be here.